Distributed Control and State Estimation of DC Microgrids Based on Constrained Communication Networks

Seyed Amir Alavi

A thesis submitted in partial fulfilment of the requirements
for the degree of Doctor of Philosophy

School of Electronic Engineering and Computer Science
Queen Mary University of London
London, United Kingdom

September 2021

Statement of Originality

I, SEYED AMIR ALAVI, confirm that the research included within this thesis is my own work or that where it has been carried out in collaboration with, or supported by others, that this is duly acknowledged below and my contribution indicated. Previously published material is also acknowledged.

I attest that I have exercised reasonable care to ensure that the work is original, and does not to the best of my knowledge break any UK law, infringe any third party's copyright or other Intellectual Property Right, or contain any confidential material.

I accept that the College has the right to use plagiarism detection software to check the electronic version of the thesis.

I confirm that this thesis has not been previously submitted for the award of a degree by this or any other university.

Signature: SEYED AMIR ALAVI
Date: September 2021

Abstract

The intermittent nature of renewable energy sources (RES) such as wind turbines and photovoltaic panels, requires advanced control systems to provide the balance between energy supply and demand in any power system. For better management of power quality and security issues, energy storage systems (ESSs) are deployed to compensate for the temporary mismatch of supply and demand. Furthermore, in rural areas with no connection to the main grid, ESSs such as batteries are deployed in large quantities as a solution for temporary power stabilization during RES unavailability. However, the control complexity of the power system increases as more ESSs are getting installed due to the need for coordination of the power transfer among them.

This thesis undertakes a thorough analysis of distributed control and state estimation designs for direct current (DC) microgrids with ESSs based on constrained communication networks. The developed distributed control and estimation strategies are designed for operation over constrained communication networks. They don't require a central coordinator for synchronization of the control tasks between the ESSs. This forms a multi-agent environment where the controllers cooperatively achieve the DC microgrid objectives, i.e. voltage stabilization, proportional power-sharing, and balancing of ESSs' energy level. To overcome the communication network constraints, event-based controllers and estimators are designed, which effectively reduce the network traffic and as a result, provide higher throughput with reduced delays for the real-time control loops of the DC microgrids. The controllers are designed to be distributed, leading to use cases such as autonomous islanded microgrids, smart villages, and plug-and-play mobile microgrids. The feasibility and performance of the proposed control and estimation strategies are confirmed in several experimental test benches by showing the higher reliability and robustness in the delivered power quality. The results have shown considerable reduction in the network traffic, meanwhile the control system provided high performance in terms of stability, robustness, power quality and endurability.

Acknowledgements

I would like to express my deepest thanks and sincere gratitude to my primary supervisor, Dr Kamyar Mehran, for his patience, guidance, support, and encouragement, and for giving me the opportunity to carry out my PhD studies. His immense knowledge and profound vision truly enabled me to develop my research and critical thinking skills.

I would like to sincerely thank my second supervisor, Prof Yang Hao, for his persistent and enormously helpful technical support and guidance throughout this work. I feel very fortunate to have had the chance to work with him. Moreover, I would like to thank Prof Arumugam Nallanathan, for contributing to my supervisory panel, and for his insightful and constructive suggestions that greatly improved this work. My sincere appreciation goes to Dr Vahid Vahidinasab for his great cooperation and support.

A special thanks to my lovely wife, Mrs Mehrnaz Javadipour, and to my family for their continued support and motivation, and for helping me progress through all the stages of my PhD studies.

Many thanks go to Dr Ardavan Rahimian and Dr Najmeh Rezaei for sharing with me their valuable professional and academic experiences, and for enduring scientific and intellectual conversations.

Lastly, I would like to thank all my friends and colleagues for their kindness, enthusiasm, support, and friendship, and for making the research group a vibrant place to work.

Seyed Amir Alavi
London, UK
September 2021

Contents

List of Figures

List of Tables

List of abbreviations

2TSA	Two-time steps ahead
AC	Alternating current
AI	Artificial intelligence
ANFIS	Adaptive neuro fuzzy inference system
ANN	Artificial Neural Network
ARMA	Autoregressive moving average
ARIMA	Autoregressive integrated moving average
BP	Backward propagation
BJT	Bipolar junction transistor
CBOR	Concise binary object representation
CC	Constant current
CCM	Current control mode
CPL	Constant power load
DAC	Digital to analog converter
DAG	Directed acyclic graph
DC	Direct current
DER	Distributed energy resource
DEKF	Distributed extended Kalman filter
DG	Distributed generation
DSP	Digital signal processing
ELM	Extreme learning machine
EMS	Energy management system
ESS	Energy Storage System
EWMA	Exponentially weighted moving average
FPGAs	Field programmable gate arrays
GPS	Global positioning system
HIL	Hardware-in-the-loop
IEEE	Institute of Electrical and Electronics Engineers
IoT	Internet of things
JSON	Javascript object notation
KCF	Kalman consensus filter
KNN	k-nearest neighbors
LSTM	Long short-term memory

M2M	Machine to machine
MAC	Medium access control
MGCC	Micrgrid control center
MIMO	Multiple input multiple output
MLPNN	Multi-layer perceptron neural network
MPC	Model predictive control
MPPT	Maximum power point tracking
MQTT	Message queue telemetry transport
MSE	Mean squared error
NCS	Networked control system
P&P	Plug-and-play
P2P	Peer-to-peer
PCC	Point of common coopling
PI	Proportional-integral
POCS	Projection onto convex sets
PMU	Phasor measurement units
PWM	Pulse width modulation
PV	Photo-voltaic
RBF	Radial basis function
RBFNN	Radial basis function neural network
RCPS	Real-time Control and Power System
RES	Renewable Energy Sources
RNN	Recurrent neural network
RMS	Root mean square
SCADA	Supervisory control and data acquisition
SNR	Signal to noise ratio
SoD	Send on delta
SoC	State of charge
SRRL	Solar radiation research laboratory
WSN	Wireless sensor network
WT	Wind turbine
ZOH	Zero-order-hold

Chapter 1

Introduction

1.1 Background

Power systems are in a very fast transition to a new era of energy transfer paradigm in which the newly added elements, such as renewable energy sources (RES) and energy storage systems (ESSs), have increased the operational complexity of the power transfer. In contrast to the past that the power system designers were mainly focused on the energy transfer from power plants to the consumers over transmission and distribution lines, modern power system designers have faced major challenges due to the appearance of the new elements in the distribution layer of the power system, not to mention the proliferation of power electronic devices and changes in the consumption behaviour.

The intermittent nature of renewable energy sources, such as wind turbines (WT) and photovoltaic (PV) panels, requires advanced control systems to provide the balance between energy supply and demand in power systems. For better management of the power quality and security issues, ESSs are deployed to compensate for the temporary mismatch of supply and demand. Furthermore, in rural areas with no connection to the main grid, ESSs such as batteries are deployed in large quantities as a solution for temporary power stabilization during RES unavailability. The deployment of ESSs creates further control and operational complexities that need to be overcome, therefore, microgrids are proposed as subsystems of a modern grid to provide higher reliability and efficiency in the presence of these challenges.

Microgrids can be categorized into two main types: alternating current (AC) and direct current (DC). A third type can also be considered as a hybrid combination of the mentioned two types, but it can be broken down into AC and DC subsystems for easier analysis. In any AC system, the voltage and frequency pair is the most important controlled variables for any control strategy. The dynamics of this pair can be directly mapped to active and reactive power. However, in DC microgrids, the only controlled variable is the voltage, which decides the power transfer between any two buses (nodes) in the power system.

From the control system aspect, controlling only a single variable seems to be less complicated than controlling more variables and this is the main reason that in the last several years, there was a vast amount of interest in application of DC microgrids and its potential to replace AC systems. This interest is boosted by the advances in the power electronic technologies of DC-DC converters and the increased number of household appliances and renewable sources that operate with DC interface. Furthermore, the ESSs such as Li-ion and Lead–acid batteries have DC electrical behaviour, which can be directly connected to the power system with a highly optimised bidirectional DC-DC converter. ESSs can also act as energy buffers for the RES such as WTs, that don't have DC electrical dynamics, which further simplifies their integration into the power system with a unified interfacing power electronic structure.

1.2 Motivation

DC microgrids, due to the elimination of frequency-dependant dynamics, expose less number of controlled variables comparing to AC ones. As a consequence, the control structure might become simpler. However, the elimination of the frequency-dependant dynamics reduces the inertia of the power system in response to external disturbances, such as sudden load changes or unplanned generation outage. Furthermore, as there is no zero crossing in the voltage of DC systems, the transient time of switching events happens considerably faster than AC systems. This critical property of DC systems has been the most important barrier in front of their application in many domains so far.

To overcome this important weakness of DC microgrids, the different control loops are required to stabilize the system in a very short time, which means the real-time performance of the controllers becomes very important for achieving the reliable and continuous operation of the microgrid. The time constraint on the operation of the control loops is directly affected by the structure of the control system and the communication interface between the measurement units, and actuators. To be specific, the measurement units are usually voltage meters and the actuators are the DC-DC converters that connect the ESSs and the distributed generations (DGs) to the power grid. A simple structure commonly used for implementation of the control systems is the centralized structure. In this structure, there is a single control system that runs all of the control loops and the measurement and control signals are aggregated toward that central system. This method is only recommended for small microgrids because it is not scalable to bigger size microgrid with more than a dozen of busses.

A better scalable solution could be that the operation of the central control system can be decentralized and delegated to several controllers that are responsible for a section of the microgrid. This method is scalable but requires a considerable amount of planning in the design phase and increases the cost of maintenance and extensibility of the microgrid after implementation. It also complicates the support for plug-and-play (P&P) functionality for integration new energy sources.

Comparing to the decentralized control strategy, a fully distributed solution can be better suited for the implementation of the control loops in a DC microgrid due to the following main reasons:

- There won't be a single points of failure in the control system.
- It is easier to support P&P addition and removal of controllers as they are designed to operate distributively with cooperation with the neighbour nodes.
- It can remove the need for a central supervisory and monitoring system, which makes them ideal for ad-hoc or mobile microgrids.

In the distributed control system of the DC microgrid, the controllers' interactions form a multi-agent control system. Agents in the microgrid are the DG controllers or ESS controllers that communicate with each other using different consensus protocols in order to achieve a common goal. Due to the real-time requirements of the control tasks, the communication interface between the controllers becomes an important element that affects response time of the control loops to the mentioned disturbances. Therefore, it is required to consider the limitations of the communication network between the agents and design the controllers accordingly.

In summary, DC microgrids provide the following advantages that makes them a feasible option for small and medium size power systems:

- Less conversion in losses connecting DC sources and loads.
- No need for synchronization with the utility grid and reactive power management.
- When a blackout or voltage sag occurs in the utility AC grid, it does not affect the bus voltage of the DC microgrid directly due to the existing stored energy of the capacitors or ESSs and the fast voltage control of the DC-DC converters.

1.3 Aim

This thesis undertakes a thorough analysis of distributed control system and state estimator designs for DC microgrids based on constrained communication networks. The developed distributed control and estimation strategies are designed for operation over constrained communication networks that have low data transmission speed and don't require a central coordinator for synchronization of the control tasks. This forms a multi-agent environment in which the controller agents cooperatively achieve the DC microgrid control objectives, i.e. voltage stabilization, proportional power-sharing, and balancing of ESSs' energy level.

As DC microgrids are distributed systems in which the components are distributed in geographical area, multi-agent control systems are proven to be the best choice in order to achieve the control objectives [2, 3]. Communication links are required among different agents in the microgrid to optimally control different aspects of DC microgrids. There are several challenges in introducing network to this type of control system such as reliability issues, packet dropout, bandwidth limitation, shared medium access and delay in data transmission. This forms an optimization problem trading of between communication resources and control performance of the DC microgrid. Event-based control techniques have been recently proposed for multi-agent control systems in order to consider the communication constrains in the controller design. In this research, event-based controller design approach is taken to design and implement the proposed control strategy for DC microgrids. Furthermore, wireless sensor networks (WSNs) are proposed for monitoring and state estimation objectives.

To overcome the communication network constraints, event-based controllers and estimators are designed, which effectively reduce the network traffic and as a result, provide higher throughput with reduced delays for the real-time control loops in the primary and secondary control layer of DC microgrids. The developed controllers' operations are distributed to remove the single point of failure, which leads to use cases such as autonomous islanded microgrids, smart villages, and plug-and-play mobile microgrids. The feasibility of the control and estimation strategies is validated in several DC microgrid experimental setups in the Real-time Control and Power System (RCPS) laboratory in Queen Mary University of London (QMUL).

1.4 Thesis structure and research path

The path followed in this thesis is depicted in Figure 1.1. Initially the research started by designing a distributed event-based Kalman consensus filter.

However, due to Kalman filter expensive computation, the required average consensus protocol was designed without Kalman filter in the next step. Afterwards, the effect of time-delay was considered for state estimation problem using event-based samples. Plug & play operation of the control system was tackled next to enable practical implementation of the proposed methods. Afterwards, a predictive (dis)charging method was designed to optimize the utilization of energy storage systems and finally a transactional control model was designed to improve the security of the proposed control systems. The structure of this thesis is described as follows:

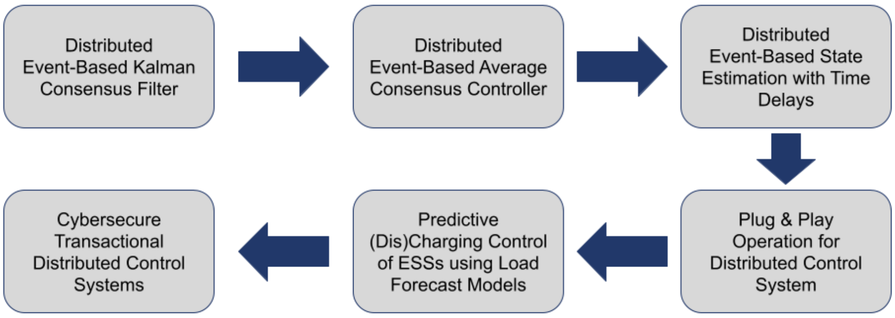

Figure 1.1: Research path followed in this thesis.

Chapter 2: This chapter covers the comprehensive background study and literature review on control and estimation of microgrids, in order to establish a solid framework for this work.

Chapter 3: This chapter presents the proposed distributed control system for DC microgrids based on event-triggered Kalman consensus filter and publish-subscribe communication pattern [4].

Chapter 4: This chapter analyzes the effect of time-delay on the distributed control system and presents the proposed event-based distributed control system with constant nonuniform time delays and communication graph topology change.

Chapter 5: This chapter presents the proposed distributed state estimation architecture for DC microgrids. The proposed architecture use send-on-delta sampling method and projection onto convex sets optimization method for signal reconstruction [5].

Chapter 6: This chapter presents the proposed forecast based consensus control for DC microgrids and it discusses how the endurability of the microgrid can be increased by prioritized (dis)charging of energy storage systems by energy consumption forecasts [6].

Chapter 7: This chapter summarizes the conducted work and primary contributions, and further addresses the concluding remarks.

Appendix A: This appendix discusses the cybersecurity aspects of the distributed control systems and presents a regulation scheme for secure operation of the distributed controllers proposed in this thesis.

1.5 Associated publications

Portions of the work detailed in this thesis have been presented in international conferences or peer-reviewed journals, as follows:

1. S. A. Alavi, K. Mehran, and J. P. S. Catalao, "A Novel Distributed Transactional Control System for Secure Operation of DC Microgrids", IEEE Transactions on Industrial Electronics, 2021 (in press).

2. Alavi, S.A., Rahimian, A., Mehran, K., Vahidinasab, V." Multilayer event-based distributed control system for DC microgrids with non-uniform delays and directional communication", IET Generation Transmission and Distribution, 00, 1– 15, 2021.

3. S. A. Alavi, K. Mehran, V. Vahidinasab and J. P. S. Catalão, "Forecast-Based Consensus Control for DC Microgrids Using Distributed Long Short-Term Memory Deep Learning Models," in IEEE Transactions on Smart Grid, vol. 12, no. 5, pp. 3718-3730, Sept. 2021,
doi: 10.1109/TSG.2021.3070959.

4. S. A. Alavi, X. Li, and K. Mehran. "Delay resilient networked control with application to microgrids.", Book: Control Strategy for Time-Delay Systems: Part II: Engineering Applications 2020, Publisher: Academic Press, ISBN: 032385804X, 9780323858045.

5. S. A. Alavi, K. Mehran and Y. Hao, "Optimal Observer Synthesis for Microgrids With Adaptive Send-on-Delta Sampling Over IoT Communication Networks," in IEEE Transactions on Industrial Electronics, vol. 68, no. 11, pp. 11318-11327, Nov. 2021, doi: 10.1109/TIE.2020.3034853.

6. S. A. Alavi, A. Rahimian, K. Mehran, "Statistical Estimation Framework for State Awareness in Microgrids Based on IoT Data Streams", The 10th International Conference on Power Electronics, Machines and Drives (PEMD 2020), 2021 p. 855 – 860, DOI: 10.1049/icp.2021.1090.

7. S. A. Alavi, K. Mehran, Y. Hao, A. Rahimian, H. Mirsaeedi and V. Vahidinasab, "A Distributed Event-Triggered Control Strategy for DC Microgrids Based on Publish-Subscribe Model Over Industrial Wireless Sensor Networks," in IEEE Transactions on Smart Grid, vol. 10, no. 4, pp. 4323-4337, July 2019, doi: 10.1109/TSG.2018.2856893.

8. S. A. Alavi, M. Javadipour and K. Mehran, "Microgrid Optimal State Estimation Over IoT Wireless Sensor Networks With Event-Based Measurements," IECON 2019 - 45th Annual Conference of the IEEE Industrial Electronics Society, 2019, pp. 4145-4150, doi: 10.1109/IECON.2019.8927727.

9. Z. Akhtar, S. A. Alavi and K. Mehran, "Voltage Control in LV Networks Using Electric Springs with Coordination," 2018 IEEE Canadian Conference on Electrical & Computer Engineering (CCECE), 2018, pp. 1-5, doi: 10.1109/CCECE.2018.8447586.

10. S. A. Alavi, A. Rahimian, K. Mehran and J. Mehr Ardestani, "An IoT-Based Data Collection Platform for Situational Awareness-Centric Microgrids," 2018 IEEE Canadian Conference on Electrical & Computer Engineering (CCECE), 2018, pp. 1-4, doi: 10.1109/CCECE.2018.8447718.

Chapter 2

Literature Review

Smart grid is a modern architecture for power systems that increases the reliability of power delivery and optimises the cost of power transmission from different types of power generation technologies to multiple consumers with different consumption behaviours. Increasing costs of fossil fuels and their consequent emission of greenhouse gases have moved the power industry to integration of renewable energy sources (RES) on a larger scale than today. Direct connection of RES to the grid such as photovoltaic (PV) panels or wind turbines (WTs) is not straightforward as the intermittent nature and ubiquity of RES in the grid demands for optimal aggregation of energy sources operating autonomously. To implement an optimal strategy, the entire power system needs to be divided into several subsystems called microgrids. In this new architecture, microgrids form a cyber-physical system in which they cooperate to achieve the smart grid's objectives.

Microgrids are often categorized into AC, DC, and hybrid types based on the specification of the operating voltage used inside them. AC microgrids have become dominant due to several important reasons such as easier voltage level transformation and the availability of components from the traditional power grids. However, the technology of electronic and power electronic devices have been improved considerably, which has led to numerous devices and equipment working with DC voltage specification.

Internal microgrid dynamics form a distributed system with the main controllable elements: distributed generations (DGs), local loads, energy storage systems (ESSs), and power electronic converters. Compared to conventional power systems with synchronous generators, microgrids with hybrid combination of DGs and RES have either small or no inertia, resulting in weak stability margin in the microgrid operation [7]. Increasing penetration level of the DGs and RES will increase the negative impact of low inertia on the microgrid dynamic performance and stability.

Due to the following advantages of DC microgrids to build the future smart grid, it is chosen for further analysis and design in this thesis:

1. Less conversion losses in connecting DC output sources and loads.
2. No need for synchronization with the utility grid and reactive power management.
3. When a blackout or voltage sag occurs in the utility grid, it does not affect the DC bus voltage of DC microgrid directly due to the existing stored energy of the DC capacitors and the voltage control of AC/DC converters [2, 3]. Therefore, DGs in DC systems are not easily tripped against these disturbances.

2.1 Microgrid structure and operating modes

The microgrids comprise dispersed energy resources, such as wind turbines, PV panels, fuel cells, and gas turbines, storage devices such as flywheels, supercapacitors, batteries, and controllable loads in order to offer considerable control capabilities to the local network operation. They can be connected to the main distribution network, but also be operated in islanded mode in case of faults in the main network.

In the connected mode, the microgrid system operator or the microgrid central controller (MGCC) must ensure the maximization of renewable energy generation and the optimization of the microgrid operation [8]. Controller functions have to be considered in order to achieve optimal operation of the microgrids in the connected mode. The microgrids system operator uses load forecasts (electric and possibly weather), production capacity forecasts (from local generators), the market prices of electricity, gas costs, local production capability, local load demands, grid security concerns, and distribution networks requests to determine the amount of power drawn from owned DGs and the amount of power to be exchanged with the grid [9]. In this framework, noncritical controllable loads can be cut off, when necessary. Furthermore, it is required to monitor the actual active and reactive power balancing. These techniques can be considered equivalent to the secondary control of the conventional power grid [10].

The structure of a microgrid is able to operate in both connected and islanded operation modes as shown in Figure 2.1. The grid-connected mode is a particular complex operating mode since local loads inside the microgrid need to be supplied alongside the power delivered to the main grid. MGCC manages the DG units in the grid-connected mode. The external loads can influence the distribution network as well as the microgrid power exchange by creating voltage drops or frequency fluctuations at the grid-connected bus.

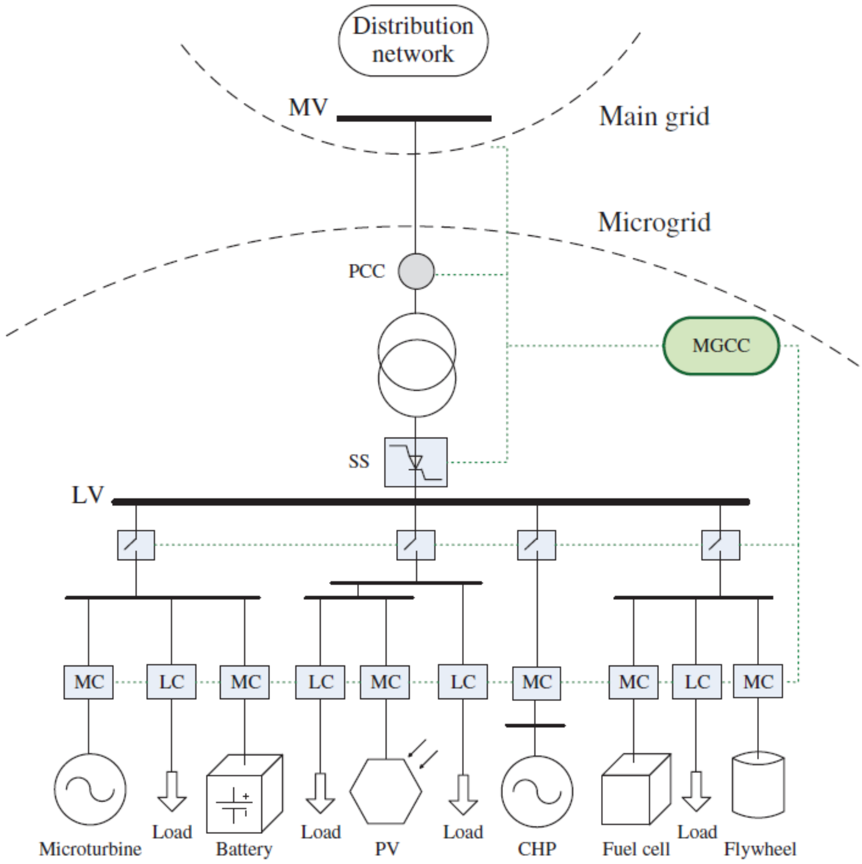

Figure 2.1: A typical microgrids structure.

This microgrid network is assumed to be radial with several feeders and a collection of loads (see Figure 2.1). Figure 2.2 shows how a interconnected network of microgrids are connected to the distribution network via point of common coupling (PCC).

2.2 DC microgrid and its applications

Due to the existing infrastructure of AC distribution, AC microgrids are the best candidate for grid-connected operating mode. DC microgrids are well suited for DC output type sources such as PVs, fuel cells, batteries, supercapacitor. Moreover, if loads in the system are supplied with DC power, the conversion losses from sources to loads are less, compared with AC microgrids. DC output type

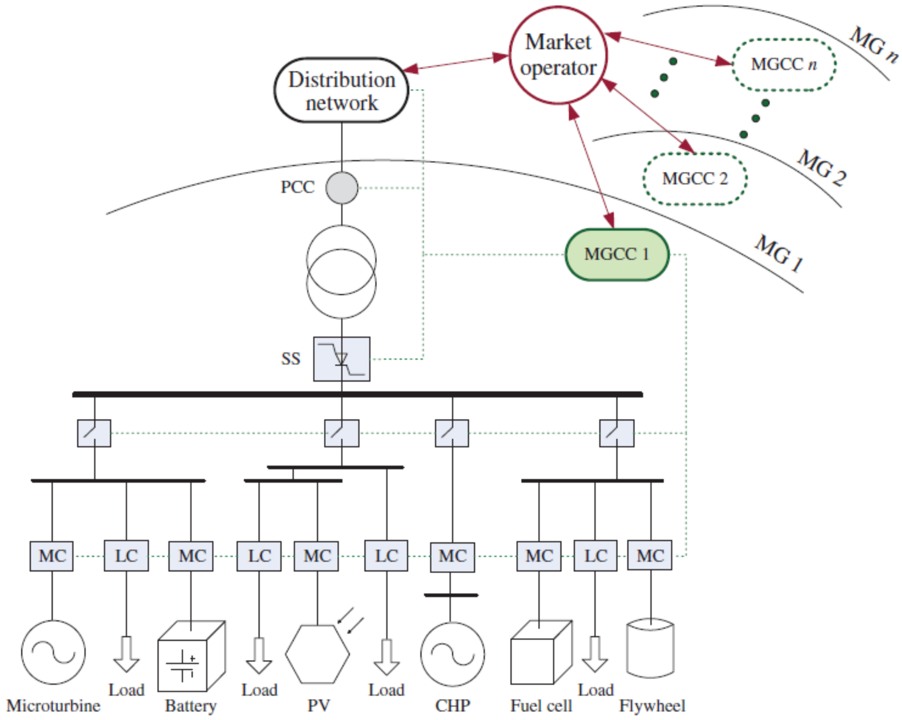

Figure 2.2: Parallel operation of MGs in smart grid.

sources, gas engine co-generations and WTs need inverters to convert DC to AC power and match the output voltages and the frequencies to those of the utility grids. Besides the loss reduction in AC/DC conversions, DC microgrids supply continuous high-quality power when voltage sags or blackouts occur in utility grids. For instance, DC power supplies are commonly used in telecommunication buildings and Internet data centres where high-quality power is required. In contrast to the advantages of DC microgrids, they have the following drawbacks:

1. Private DC distribution lines must be constructed for DC microgrids.

2. Protection is more challenging as there is no zero cross point of voltage in DC systems.

3. To provide high efficiency, the loads adapted for DC power supply are required.

Given the intermittent nature of electric loads, sources must be dynamically controlled to respond to the load demand at any moment, while maintaining the required voltage level at consumer supply. Sources may reflect a variety of rated powers. The total load demand among the sources must be in proportion to their rated power. This concept, widely known as proportional load sharing, prevents overstressing of sources and helps to span the lifetime of power generation entities in the microgrid. While the source voltages are the sole variables controlling power flow, they must be tightly managed to also ensure a desirable voltage regulation. The DC microgrids have found ever-increasing importance for the efficient realization of a number of crucial applications in the electric power industry, as they differentiate themselves from the AC counterparts in having the non-zero-crossing current and reactive power [3, 9, 11]. However, controlling of the DC microgrid subsystems poses a considerable challenge, e.g., grid voltage stabilization is still a major problem due to the limitations in the voltage compensation techniques, when compared to the conventional AC power system [7, 12, 13].

2.3 Hierarchical microgrid control

The hierarchical control and power management of microgrids has different operation layers which are responsible for:

- providing proper load sharing and DG coordination [13],
- voltage regulation in both operating modes [10],
- operating cost optimization [14],
- power flow control between the microgrid, neighbourhood microgrids, and the main grid [15].

In terms of control and communication topology, microgrids control strategies are categorized into **centralized, decentralized** and **distributed** approaches, which are applied in different layers of microgrids control structure [12]. See Figure 2.3.

Centralized Strategy: In this strategy, a main controller controls microgrid variables using the data collected from different sensors across the microgrid. This control strategy gives the main task to a central controller and as a result poses a single point of failure. Moreover, the plug and play capability in microgrids for dynamic penetration of RES and DGs dynamically may not be easily achieved. The considerable data collection also increases network bandwidth and availability requirement [16–18].

Decentralized Strategy: In this strategy, only local controllers make the decision without direct communication with each other. The only network requirement is for top level controllers, which may receive set points from a central controller. Although this strategy reduces the cost of network communication and eases the plug and play installation of new devices (e.g. droop control),

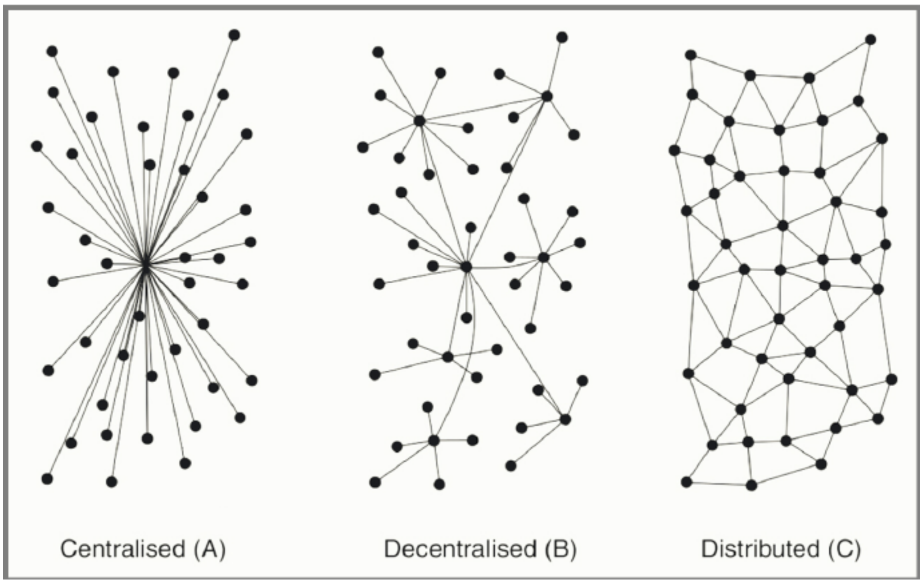

Figure 2.3: A) Centralized, B) decentralized and C) distributed control strategies.

consensus among the local controllers are required for the best performance. Additionally, certain control objectives can not be achieved without communication among the agents [7].

Distributed Strategy: To overcome the limitations of the former methods, this strategy proposes different controllers to cooperate and achieve global control objectives [19]. There is no single point of failure in this structure to increases the reliability of the system [20–22].

Microgrid control strategies will be efficient and effective when they are applied on different levels of operation with multiple objectives to provide reliable, secure, and economical operation either in grid-connected or islanded mode. The most salient challenges in the control of microgrids are:

- Microgrids have low inertia and therefore are less robust.
- Uncertainties in microgrids can easily drive the system to instability.
- Mathematical modelling and computational complexities of high order dynamics.
- Bidirectional power flow in the distribution lines.

On the other hand, DGs output voltage and current control, active/reactive power balancing and frequency/voltage regulation, demand-side management, economic dispatch, and transition between operation modes are mentioned as the most important control objectives of the microgrids control system. While in the grid-connected operation mode, concerns are on the interaction with the main grid, reliability and control issues are more significant in the islanded operation mode as in inertia of microgrids becomes very weak. In the islanded mode, the operation also is more challenging.

Generally the instabilities in microgrids can be listed as follows:

- *Small signal instability:* There are many recurring reasons for small signal instability including but not limited to dynamic impacts of feedback controllers, continuous load switching, oscillation modes, and DGs power limit.

- *Transient instability:* Unexpected islanding, DG outage, large and sudden load change, and cascaded faults are the most important reasons of the transient instabilities.

- *Voltage instability:* Reactive power limits, load dynamics, and tap changers create most of the voltage stability problems

- *Frequency instability (in AC or hybrid microgrids):* Load-generation imbalance, under frequency load shedding, and active power limits are considered as the main reasons for frequency instability.

In this thesis, mainly, small signal stability is the concern of the control system. A hierarchical control structure is able to provide efficient load sharing and DGs coordination, voltage/frequency regulation in both operating modes, microgrid resynchronization with the main grid, operating cost optimization, and power flow control between the microgrid, neighbourhood grids, and the main grid. As shown in Figure 2.4, hierarchical control has four levels, i.e. the local (primary), secondary, central/emergency, and the global control.

The local control that includes fundamental control hardware and DGs internal voltage/current control loops, stabilizes DGs by measuring and controlling the local signals.

The secondary control provides power sharing as a communication-based method for parallel configuration of DGs and compensates the voltage and frequency deviations caused by the load variation and local control operation.

The central/emergency control facilitates microgrids supervision activities. Its role is particularly important in the islanded operation mode. It operates as the microgrid energy management system (EMS) and monitors the microgrid's local and secondary controllers. It is also responsible for islanding detection and connection/disconnection to/from the main grid, as well as emergency control and overall protection schemes.

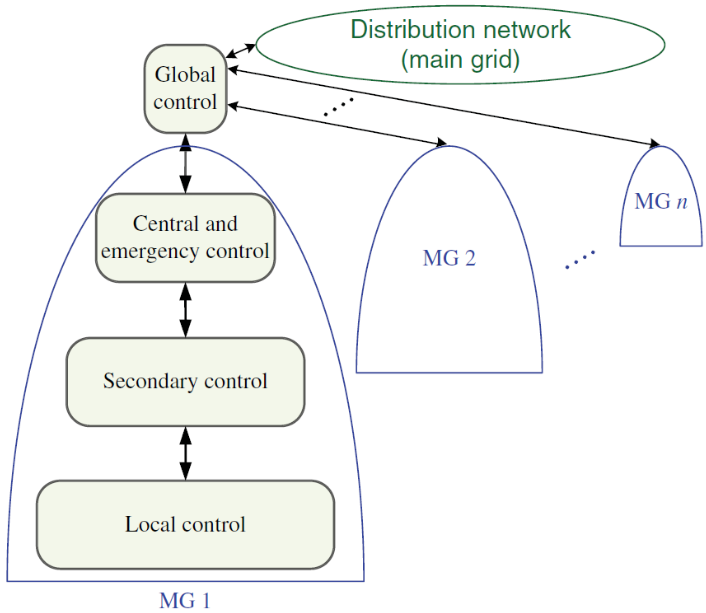

Figure 2.4: Microgrid control layers.

Finally, the global control manages the power flow between the given microgrid, other interconnected microgrids and the main grid. It provides an economically optimal operation.

Despite an extensive research, the following topics are still open problems in microgrids control:

- Improving robust performance and stability against the structured and unstructured uncertainties,
- Enhancing the transient response of the closed-loop systems,
- Accounting for imbalance and harmonics,
- Improving scalability of the control frameworks,
- Incorporating the DC-side dynamics in the control synthesis,
- Enhancing fault ride-through capabilities,
- Unified control schemes for both grid-connected and islanded operation modes,
- Providing a smooth transition from islanded to grid connected mode and vice versa.

The main advantages of a distributed control architecture include the seamless real-time operation, no single point of failure, reduction in the computational and communication complexities, and distribution of the tasks among the local controllers in the microgrid [23, 24]. The quality of power primarily relies on the fast real-time communication between the distributed controllers. Different approaches are proposed in order to effectively minimize the communication time and complexity. In [23], it is suggested that only one controller can communicate with its neighbor controllers rather than all the controllers. However, to satisfy the overall control objectives, the limitations of the main protocol candidates for the network should be appropriately considered, hence, the separation of concerns would not be held anymore [8].

2.4 Control systems over communication networks

Networked control systems (NCSs) are proved to be an essential framework for the implementation of the distributed control architectures in a number of applications, such as the power systems [25], industrial process control [26], power substation automation [27], aircraft control [28], and autonomous vehicles [29]. In an NCS, controllers are programmed on digital embedded platforms, and are connected to sensor/actuator nodes via a shared communication link. This offers a flexible structure where remote devices can be added, removed, and located with a minimum wiring and maintenance cost. With the advent of the Internet of things (IoT), the NCSs are moving towards wireless operation, where a channel may be shared among thousands of sensing nodes in the microgrid. Therefore, considering the fact that the channel bandwidth is limited, the NCS objectives should include reduction of the network traffic, as well as increasing the battery life of the sensors, while guaranteeing the overall performance.

The astonishing growth of communication technologies over the past decades reflected by available protocols, coding, and modulation algorithms and the switching/routing technologies for packet-based networks rapidly attracted the interest of the control community. The use of a multi-purpose shared network to connect decentralized control elements promised improvements in terms of more flexible architectures, reduced installation and maintenance costs, and higher reliability than traditional bus-based communication technologies. In this part, distinguishing characteristics of the NCSs are reported.

Typically, a control system is composed of the following elements: system or plant to be controlled; sensors measuring plant outputs, and transmitting them; automatic controllers receiving plant outputs and making decisions on the control signals to be applied to the plant; and actuators receiving the inputs sent by the controller and applying these inputs to the plant. Point-to-point communication links between the different devices make it possible to implicitly consider the perfect communication channel approach: absence of transmission delays, information integrity and unlimited bandwidth (Figure 2.5).

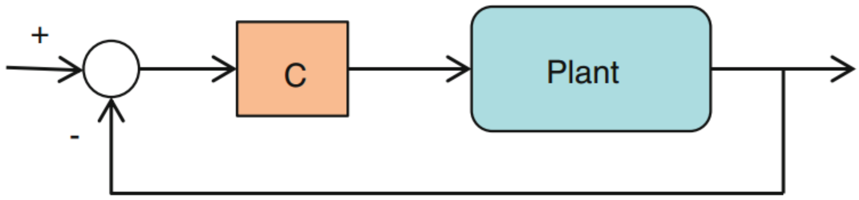

Figure 2.5: Classic control scheme with the assumption of perfect communication channel

Needless to mention, the feature that distinguishes an NCS from a classical control system is the presence of a communication network (Figure 2.6). The perfect communication channel assumption does not hold when a network mediates the connection among the different elements. Even when dedicated, standard communication networks are usually designed to preserve data integrity and do not suit the stringent real-time requirements of closed-loop control. These problems become particularly apparent when wireless or non-dedicated networks are used. A large number of systems may be using the communication channel concurrently sharing the available bandwidth.

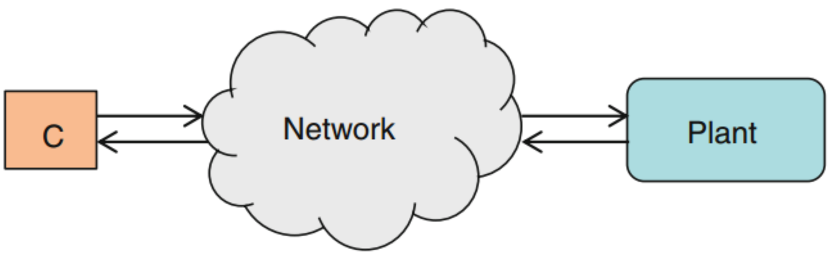

Figure 2.6: Networked control scheme

Hence, the following questions arise: Why is it better to use this type of technology for control purposes? In which situations are these solutions more suitable?

On the one hand, there are a number of generic advantages when using digital communication networks. Namely,

- **Low cost:** Using a point-to-point communication in large-scale systems or geographically distributed plants is generally a costly and impractical solution. Wireless or even wired networks, however, reduce the connections and the wire length. Concomitantly, the deployment and maintenance costs are shortened.

- **Reliability:** In addition to the acknowledgement retransmission mechanism of conventional communication protocols, a meshed network topology intrinsically improves reliability as dynamic routing allows to find alternative routes in the case that broken links are present. Also, fault detection algorithms can be easily implemented.

- **Maintenance:** The reduction of wiring complexity facilitates the diagnosis and maintenance of the system.

- **Flexibility:** Network structured systems offer flexible architectures, making easier the reconfiguration of the system parts and allowing a simpler addition of new devices.

- **Accessibility:** Traditional centralized point-to point control systems are no longer suitable to meet new requirements, such as modularity, control decentralization, or integrated diagnostics.

On the other hand, in a large number of practical situations, engineers use communication networks for control purposes:

- **Space and weight limitation:** Stringent limitations of this type need to be accomplished, for instance, in avionics (commercial aircrafts, unmanned aerial vehicles) or embedded systems in the automotive industry.

- **Coverage of considerable distances:** chemical plants, large-scale factories, and microgrids.

- **Control applications where wiring is not possible:** fleet of autonomous vehicles, safe driving control systems involving inter-vehicle communications, teleoperated systems, etc.

2.4.1 Impact of communication network constraints in general

There are general constraints on communication networks that can affect a control system. Communication through a shared network is imperfect and may be affected by some of the following problems (see Figure 2.7) in general:

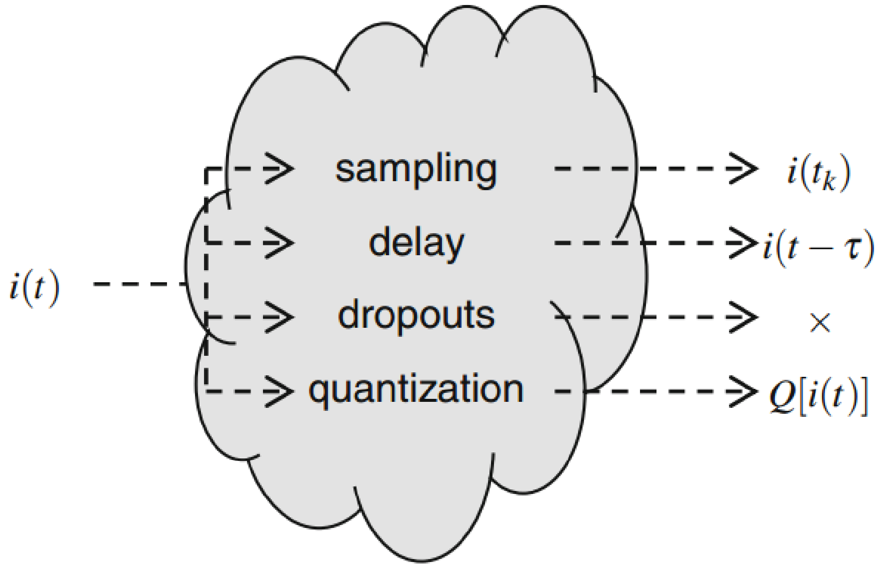

Figure 2.7: Networked control drawbacks.

- **Sampling:** In most digital networks, data are transmitted in atomic units called packets. These packets are sent at a finite rate, therefore continuous models must be discretized with an adequate sampling time. Since the available bandwidth is limited, sampling appears as a problem of the channel. In some network protocols, such as WiFi or Ethernet, this sampling time is not constant, as it strongly depends on the network traffic and congestion. A correct choice of the sampling periods will help to maximize the available bandwidth in those cases

- **Delay:** The overall delay between sampling and decoding at the receiver can be highly variable because both the network access delays (i.e. the time it takes for a shared network to accept data) and the transmission delays (i.e. the time during which data are in transit inside the network) depend on highly variable network conditions such as congestion and channel quality. Consequently, packets travelling through a network are received belatedly. For example, it is certainly common to receive one packet before another released earlier. Some protocols, such as TCP/IP, implement mechanisms to consider delay, however at the cost of increasing it. Even so, the reordering might be useless in control applications

- **Packet dropouts:** Some packets may also be lost, mainly because of the capacity of the reception buffer. If an element is receiving packets at a higher rate than it can process them, the buffer could overflow at any instant. Even, errors in physical links may cause the loss of information, as the packet must be discarded. Though some protocols guarantee data integrity through retransmission mechanisms, this is often useless in real-time control as old data packets cannot be used for control purposes. Indeed, many networked control algorithm discard and treat as losses those packets received with excessive delays.

- **Quantization:** A quantizer is a function that maps a real-valued function into a piecewise constant function taking on a finite set of values. This mapping typically introduce inaccuracies inversely proportional to the cardinality of the representation alphabet. One of the basic choices in quantization is the number of discrete quantization levels to use. The fundamental trade-off in this choice is the resulting signal quality versus the amount of data needed to represent each sample.

In this thesis, only the effect of communication delay and sampling are considered as these two are the major issues in a communication network.

2.5 Distributed event-based control approaches

By convention, the information between the sensors, actuators, and controllers is exchanged at constant rates of packet transfers in digital systems. The sampling frequency has to guarantee the stability of the system under all possible scenarios, and this can sometimes yield a conservative choice of the sampling period. Moreover, all tasks are executed periodically and independently of the state of the system.

In recent years, the idea of taking into account the system state to decide when to execute the control and sampling tasks has received interest to tackle the drawbacks of NCSs. In general, in this non-conventional sampling paradigm, information is exchanged in the control loop when a certain condition depending on the state is violated. Hence, there is an adaptation to the needs of the process at any time.

However, there is no uniform terminology when referring to this concept. One can find in the literature the terms event-based control, event triggered control, send-on-delta control, level-crossing control, self-triggered control, minimum attention control, any time attention control, and many more. All of them have basically the same idea, but vary in implementation. We will refer to *event-based control* or *asynchronous sampling* to cover all these approaches.

Despite its recent popularization, event-based control is not actually a new concept, and its origins date back to the late 1950s when it was argued that the most appropriate sampling method is to transmit data when there is a significant change in the signal. Later, in the 1960s and 1970s, a heuristic method called adaptive sampling [30] was popularized. The objective was to reduce the number of samplings without degrading the system performance, evaluating in each interval the sampling period.

More recently, an event-based PID controller was implemented in [30] showing that the number of control updates was reduced without degrading the performance of the system. In [31], level-crossing control was applied to control the angular position of a motor with a low-resolution sensor.

The first analytical results were for first-order linear stochastic systems in [31], showing that under certain conditions the event-based control outperforms the periodic control. But a real impulse to the asynchronous control came out a few years later when many researchers realized the benefits of applying this theory to networked control systems. Next section will present a literature review of event-based approaches applied to NCSs as well as the main concepts used in this formalism.

In most implementations, an event is triggered when some error function exceeds a tolerable bound. How this error function and this bound are defined distinguishes the different approaches in the literature that are discussed next.

2.5.1 Deadband Control

If the error is defined as the difference between the state of the last event occurrence and the current state, and the bound is defined as a constant, an event is triggered whenever

$$||\varepsilon|| = ||x(t) - x(t_k)|| \leq \delta \tag{2.1}$$

becomes positive, where t_k refers to the instant of the last event and t is the current instant of time. The value of δ determines, on one hand, the performance of the system and the ultimate set in which the state of the plant is confined around the equilibrium, and on the other hand, the average frequency of communication. Figure 2.8a, b depict two examples of deadband control for a first order and a second-order system, respectively.

2.5.2 Lyapunov Approaches to Asynchronous Control

Deadband control does not generally yield asymptotic stability. And so, some researchers have investigated triggering rules to fulfil this. One example is presented in [32] where the error is bounded by the state at the current time

$$||\varepsilon|| = ||x(t) - x(t_k)|| \leq \sigma||x(t)|| \tag{2.2}$$

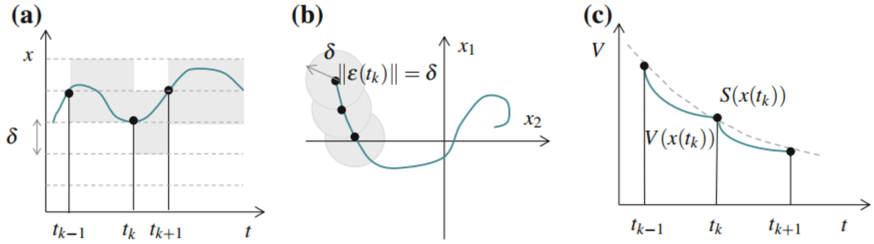

Figure 2.8: Examples of event triggering rules

The approach yields the asymptotic stability of the system but the inter-event times become shorter when the system reaches equilibrium. In [32] it is shown that a minimal inter-event time is guaranteed to exist only under suitable assumptions.

Other authors have exploited the idea of using Lyapunov methods to define the triggering rule [33]. An event is triggered when the value of the Lyapunov function of the closed-loop system for the last broadcast state reaches a certain threshold of performance $S(x, t)$ (see Figure 2.8c):

$$V(x, t) \leq S(x, t) \tag{2.3}$$

This condition also guarantees that equilibrium is reached asymptotically.

2.5.3 Time-Dependent Event-Triggering

Recently, time-dependent triggering rules have been proposed to reach the equilibrium point asymptotically. In [34, 35], the trigger functions for linear interconnected systems and multi-agent systems, respectively, bound the error as

$$||\varepsilon|| \leq \delta e^{-\beta t}, \delta, \beta \geq 0, \tag{2.4}$$

which has the aforementioned property, guaranteeing a lower bound for the inter-execution times. Note that this bound approaches to zero when $t \to \infty$, the Zeno behaviour is however avoided even in non-ideal network conditions.

2.5.4 Self-Triggered Control

Sensor networks are a special case of networked control systems in which the energy consumption plays a crucial role. Thus, event-triggering approaches are convenient in sensor networks since the number of transmissions can be decreased. However, it has been discussed [36, 37] that most of the energy consumed in a sensor node comes from the task of monitoring the measured variable(s) rather than the transmission. The asynchronous control strategies discussed above require the continuous monitoring of the state. For this reason, a new approach known as self-triggered control has emerged in the recent years.

Self-triggering policies determine the next execution time t_{k+1} by a function of the last measurement of the state x_k. The sensor nodes do not monitor the process until they are triggered at time t_{k+1}, they then take the measurement and transmit it, and the next execution time is computed again [38].

2.5.5 Periodic Event-Triggered Control

Periodic event-triggered control strikes a balance between periodic control and event-based control. As self-triggered control, it avoids continuous monitoring of the system outputs while preserving the reduction in resource utilization. So, instead of checking the trigger condition continuously, this is only evaluated at instances of time defined by a period T_s.

The design methods that have been proposed mainly use Lyapunov-based trigger functions and provide the tools to check stability and performance for a given control gain and a sampling period. One additional advantage is that it guarantees a minimum inter-event time of (at least) the sampling interval of the event-triggering condition.

2.5.6 Event-Based Control and Output Measurement

The triggering rules presented previously are all based on full state measurement, although in practice the full state is not often available. If the same setups are tried to be used for output feedback controllers, the Zeno behaviour might occur.

To solve this problem, the existing approaches to output-based asynchronous controllers can be categorized as observer-based or not. To the first category belong [35]. The measured state is replaced in the trigger function by the estimated state provided by the observer [35] or the filter [39]. The second direction is to use a different structure in the controller. A dynamical output-based controller is proposed in [25]. Using mixed event-triggering mechanisms, the ultimate boundedness can be guaranteed while excluding the Zeno behaviour. A level crossing sampling solution with quantization in the control signal is presented in [28], where an LTI continuous-time controller is emulated.

2.6 Communication patterns for distributed control systems

There are several communication models that can be integrated into a control system. Each model has both advantages and disadvantages, and the system designer has to effectively decide which model to employ for the implementation of the control system. In this work, several communication models are studied in detail and are compared with each other. In the following, a comparative analysis has been given for a number of the intended communication models, for the purpose of the appropriate employment in the DC microgrids.

1. **Request/Response:** This communication model is one of the most commonly known models. It consists of a client that requests a service from a server, as shown in Figure 2.9 (a). It is a useful model for the client-server or master-slave architectures [40]. However, the drawback of this model is the inequality of participants as apparent in the network topology. This makes it difficult for the bidirectional communication scenario, in which both the parties request information from each other, especially if firewalls are present. Consequently, either events, event-subscriptions, or security is difficult to manage, and require additional services and substantial resources if firewalls are used in the network.

2. **Event-Subscription:** This communication model allows a client to subscribe to events of a given type from a server. The server then informs the client each time the event is triggered, without having to constantly poll the server, as in Figure 2.9 (b). Advanced event-subscription mechanisms can include client-specific requirements of when events are desired and under what conditions. The benefits of using this communication model are that half of the messages are not needed over time, and the latency of updates is kept to a minimum. The problem with this model is that it is not designed for the multiparty communication scenario.

3. **Multicasting:** The previous models are primarily considered for the communication purposes between two entities. However, a more efficient model is required in cases when the same information has to be sent to multiple entities at the same time. Here, a sender sends one message through an intermediary (i.e. a broker or a router) which then distributes it to multiple recipients that have all requested participation in the communication. This model saves the bandwidth because the sender does not have to send individual messages to all the parties by itself. Also, the sender does not even have to know who the recipients are.

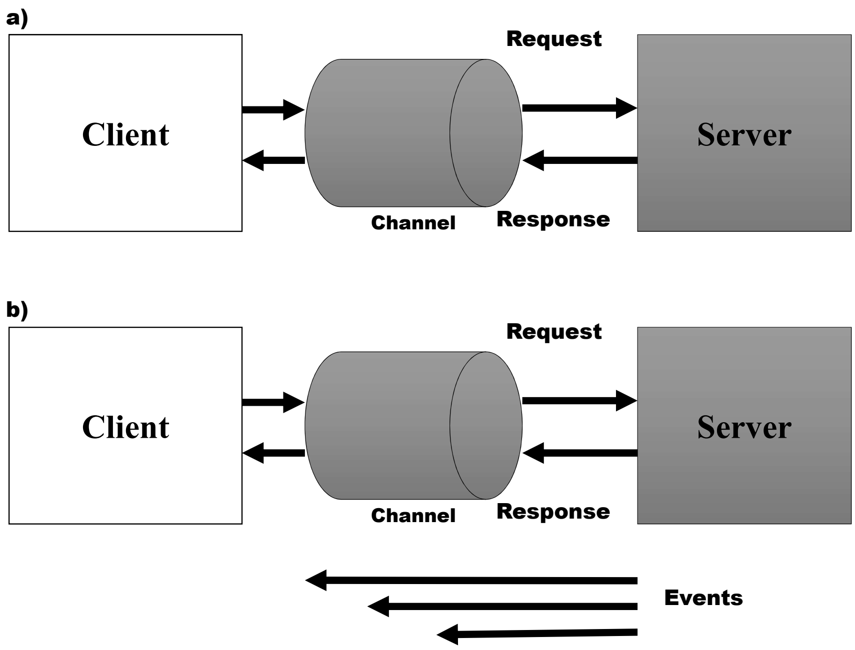

Figure 2.9: The communication models for the bidirectional communication scenario: (a) request/response model; (b) event-subscription model.

Although one can use this model in order to save the bandwidth, it is often used as a means of overcoming the restrictions in the chosen protocol, and its support of the event-subscription model, as well. In addition, multicasting is inherently difficult to secure, and it is more efficient in terms of the bandwidth only if the recipients actually use most of the transmitted values. In the case where frequent multicasting for decreasing the latency in the network is desired an implausible, the multicasting model might result in an increase rather than decrease in the required bandwidth [41].

4. **Queues:** The first-in, first-out queues, is a model that allows one or more entities to post the messages or tasks into a queue, and then lets one or more receivers receive the messages in an ordered fashion. The queues reside on an intermediary node or network to which all participants are connected. This model is an excellent tool for the load balancing purposes, where the collected tasks from multiple sources need to be distributed among the existing workers, perhaps having different performances. Queues can hardly be used for real-time communications in control systems, since the message should be saved at first, and then be processed at the controller via an intermediary node.

Publish/Subscribe: This communication model is an extension of the multicasting model, with the difference that messages transmitted are stored in the intermediary node. The messages, or a reference to the messages, are distributed to the corresponding subscribers, depending on the protocol. Also, only the latest message is stored, a given number of messages are stored, or all messages are stored in the intermediary, depending on the chosen protocol, as well as the settings of the intermediary [42]. The difference between distributing the entire message and distributing only a reference to the message is important and affects the performance of the solution in terms of the consumed bandwidth. If the subscribers consume most of the messages, forwarding the messages themselves is more efficient, as in the case of multicasting. If, however, consumption occurs only on demand, then sending shorter references is more efficient because these messages are smaller and subscribers would use only a minority of them to fetch an actual message. In order to fetch a message in the latter case, a separate request/response action needs to be performed [43].

The behaviour of each model has been analyzed from the control point of view. In this treatise, the publish-subscribe communication model is used for the practical implementation of the distributed event-based control strategy. In the publish-subscribe model, a node can act as a publisher, subscriber, or both simultaneously. The network roles can be dynamically changed to ensure a flexibility to reconfigure the directions of the data exchange. The main advantage of this model is that the data can be exchanged intelligently between the devices (i.e. the publishers send the data to the specific subscribers without having a subscription knowledge of each node). This keeps the setup process easier for the overall maintenance of the network, and enables the self-configuration of the devices, as one of the primary characteristics of the industrial ad-hoc networks. The process of selecting messages for the reception and processing is called filtering. The topic-based and content-based filtering are the two common forms of filtering used in new communication protocols introduced in the context of IoT. In the publish-subscribe network setup, a server manages the topics and contents, which is called a broker. The broker-free setup can be achieved with the distributed topics/contents suitable for the proposed distributed control structure [44]. The topic-based publish-subscribe communication model also enables the selective message distribution among a number of sources and sinks [45]. Messages are associated with the topics and are selectively routed to destinations with matching topic interests. Subscribers show their interest in receiving data with a given topic and data sources publish messages on the topics.

The main advantages of the publish/subscribe communication model compared with the aforementioned models can be summarized as:

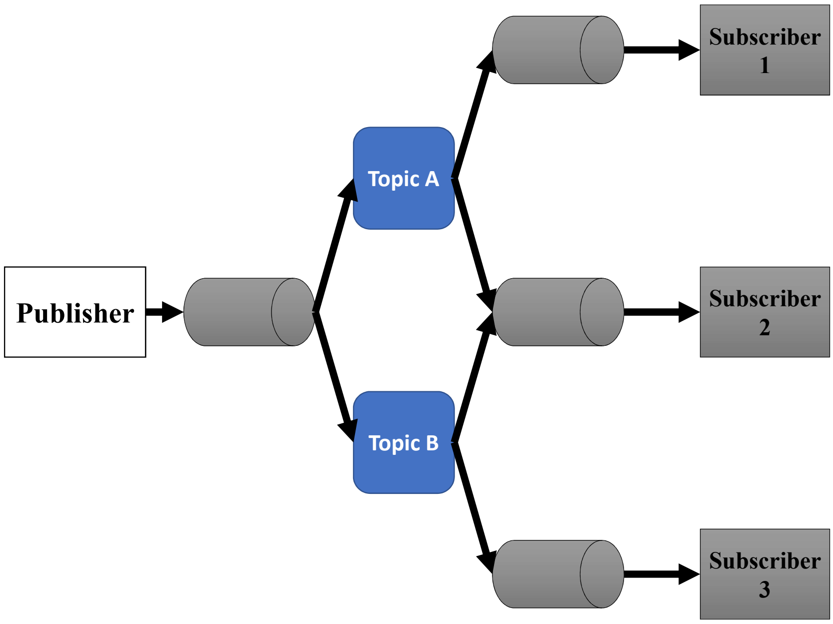

Figure 2.10: Block diagram of the topic-based publish-subscribe model for the industrial distributed communication scenario.

- Adaptive role change in a dynamic environment from the publisher to the subscriber and vice versa.
- Intelligent data exchange among the nodes without having a subscription knowledge of each node.
- Automatic self-configuration of the nodes in the ad-hoc network without a central configurator which enables the plug and play operation of the microgrid.
- Intrinsic discrete event transmission support which suits it as an ideal choice for the event-triggered control.

Figure 2.10 also presents the concept of the topic-based publish-subscribe communication protocol model. Multiple subscribers can listen for a predetermined topic, and also multiple publishers can publish new data to certain topics. The only drawback with this model is that when subscribers initially subscribe to a certain topic or content, their initial value remains undefined until the next publishing cycle. A number of communication protocols are proposed to tackle this issue, such as the message queue telemetry transport (MQTT) protocol, which uses the retained value in the broker-based structures. Consequently, when a subscriber connects to the broker, it will release the retained value of

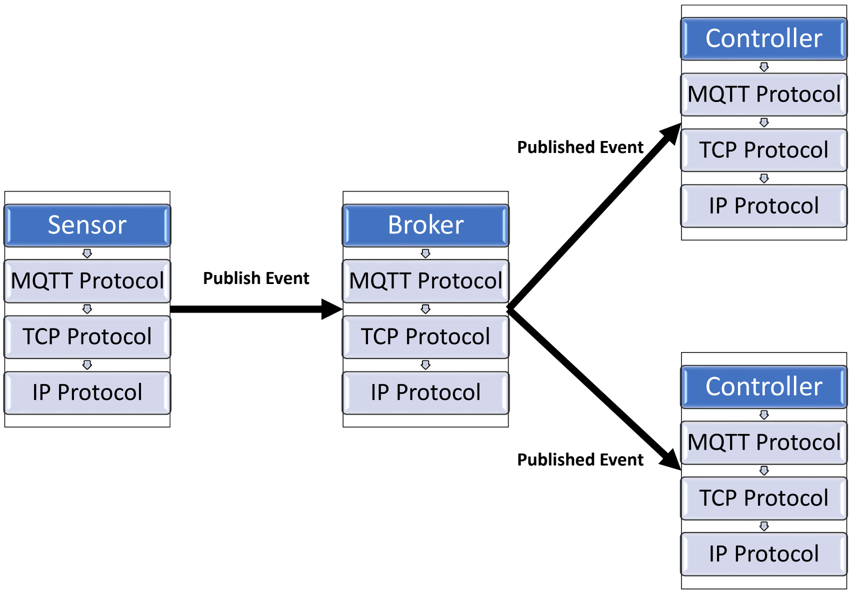

Figure 2.11: The MQTT protocol stack for the event-based implementation.

the most updated published event to the subscriber [46,47]. The protocol stack of MQTT is depicted in Figure 2.11.

A distributed microgrid control system requires well-defined communication patterns to support scalable operation for a high number of controllers and dynamic configuration of the control system. Publish-subscribe and request-response are the most suitable data sharing patterns for microgrid controllers [46,48]. In the request-response communication pattern, there are several master controllers that poll the desired variables from slave devices. Despite its simplicity, this pattern doesn't support the even-based operation as the master must always poll for new changes and the direct communication links are required for real-time operation. In contrast, the publish-subscribe pattern supports dynamic role change of the controllers to publish changes or subscribe to variable changes in a distributed event-based model. The summary of the patterns comparison is provided in Table 2.1.

2.7 Transactional microgrids

The reliance of the distributed control system on the communication network requires network security consideration. The traditional approach for security of networked control systems is to isolate the control tasks from the rest of the network either virtually or physically [49]. This approach works well if the network

Table 2.1: Comparison between the different communication models for the distributed event-triggered control of DC microgrids.

Communication Model	Support for Dynamic Environment	Smart Message Delivery	Plug & Play	Event-Based
Request/Response	Weak	Weak	No support	No support
Event-Subscription	Weak	Medium	No support	Strong
Multicasting	Strong	Medium	Medium	Medium
Queues	Medium	Medium	No support	Medium
Publish/Subscribe	**Strong**	**Strong**	**Strong**	**Strong**

is not public and has a limited number of access points with sufficient supervision. However, microgrids are distributed by nature and therefore, networking technologies such as the internet of things (IoT) can be used to implement the networked control system. In these types of public networks, the security of the distributed controllers is a major issue, especially with the advent of quantum processors that are able to decipher many types of encryption methods. A proactive approach is therefore needed to provide inherent security in the control tasks themselves, able to provide higher degrees of attack detection and mitigation.

Recently, the concept of the transactional microgrid is introduced by the pioneering works of [49–51]. The core concept in transactional microgrids is that energy transfer between the consumers, producers, prosumers (i.e. both consumes and produces energy) are modelled in transactions of an open market [52]. This idea promotes the application of cryptocurrencies in energy markets, which are managed by a distributed ledger with full transparency and security [53, 54]. A ledger is simply defined as a log of an ordered list of transactions, e.g financial and energy transactions [50]. A distributed ledger is basically a set of information protocols for accessing, validating, updating, and storing records in a transparent and secure manner across a decentralized peer-to-peer (P2P) network of servers, spread over multiple locations. It further enables dynamic energy pricing and accurate billing applications. So far, a number transactional microgrids models are proposed such as the works in [53] and [55], however, their applications were limited mainly to the trades in energy markets [56], and the security preserving advantages for the real-time control systems are not studied. The details of transactional microgrids are not furthermore discussed in this thesis, except a short analysis in the appendix describing the concept of distributed transactional control systems to support cyber secure implementation of the proposed controllers in this thesis.

2.8 Effect of load forecasting on the optimal operation of control system

The existing control systems are mainly concerned with the real-time operation of the microgrid to compensate for the disturbances. Based on this approach, the unit commitment and energy management tasks are processed centrally in the tertiary control layer of the microgrid, which relies on a separate communication network. The separation between the real-time control layer and the energy management layer limits the resolution of the optimization problems that could be solved should the layers be integrated. As an example, a single day-ahead energy forecast requires the collection of data from smart meters for the previous days and running the computationally intensive algorithms centrally to predict the load. Considering the growing number of smart meters and the amount of data required, this leads to major scalability problems in the tertiary layer management, not to mention the privacy and communication issues.

Distribution of the forecasting tasks to the local controllers has been recently proposed owing to the advances in the area of edge computing and distributed control systems, which has led to new approaches to solving the energy management problems in microgrids [5, 57].

In the microgrids, distributed control and estimation are mainly implemented in the secondary layer, due to the distributed nature of the RES, and the limitations of the communication network. Optimal neighbor data sharing and multi-agent consensus protocols are the problems of interest in the proposed distributed strategies [24, 58]. Among the available consensus protocols in the multi-agent systems, distributed average consensus (DAC) is the commonly used one, in which the agents agree on the average value of their shared variables from an initial condition [4].

There are a number of important applications for the distributed control systems, such as in power systems [25], industrial automation [26], situational awareness [46], drones control [28], and in self-driving vehicles [29]. Decentralized control approaches are also reported in several works such as [59–62]. They are mainly categorized into two types, virtual resistance control [59] and impedance control [62]. Virtual resistance droop control can only be implemented in homogeneous ESSs, without the capability to allocate different frequency components of loads. For example in [59], a decentralized output constrained control algorithm is proposed for single-bus DC microgrids. In [61], the authors have proposed a decentralized controller which has removed the need for an accurate model of the DC microgrid. However, virtual impedance control is able to assign different frequency components of the loads to specific ESSs [60, 62]. The majority of the virtual impedance control methods are based on filters such as works in [63]. Although decentralized methods can solve the real-time control problems in a microgrid, they can not be used in energy forecasting applications, which require a reliable communication network.

As each ESS can act as both a source or a load in its charging and discharging modes, it needs to be integrated as part of the microgrid unit commitment solution. Energy management of the ESSs during the microgrid operation is mainly concerned with the stabilization of the state of charge (SoC) levels at different times of the day. In a microgrid with RES, the load and generation profiles are the main players affecting the SoC of ESSs during the microgrid operation, therefore, load forecasting is an essential step throughout the design of the microgrid control strategy and its energy management plan.

The main approach for ESS management is based on keeping the ESSs fully charged to respond to supply failure, disregarding the load behaviour and generation forecast [64]. For centralized small size microgrids, this approach works well, as the ESSs are managed centrally [64]. However, for distributed microgrids with low inertia of the operating point and the intermittent behaviour of RES, ESSs are used to establish voltage stability and accurate SoC balancing [65,66]. This needs a multi-objective control system to provide the operating point stability, and optimal reserve endurability when the distributed generations (DGs) are not available. The multi-objective control problem must be resolved in real-time, considering the scalability of the distributed system. Additionally, since many RES such as PV panels and fuel cells (FC) naturally generate DC, they can easily get interfaced to a DC system [67]. DC microgrids, comparing to the AC ones, require fewer interfacing circuits and also eliminates reactive power and frequency constraints [2, 10]. These fewer constraints lead to a simpler control system with reduction in energy losses [68].

Recently, deep neural network models have become a feasible solution for energy forecasting. Deep learning mainly refers to multiple layers of neural networks being stacked, as opposed to shallow learning, relying on stochastic optimization algorithms for training. Several layers provide different abstraction levels that can improve learning performance. In the proposed models, the long short-term memory (LSTM) recurrent neural network (RNN) has unique capabilities for time series sequence [69], as introduced by Hochreiter and Schmidhuber [70]. This has led to innovations in many areas such as speech recognition, image captioning, and dynamic system modeling [71]. Long-term load forecasting is used in power system infrastructure planning, while short-term load forecasting is mainly used for online real-time control of the microgrid operations [72].

There is a considerable amount of research in the short-term load and generation forecasting. In [73], the autoregressive integrated moving average (ARIMA) model is proposed for intraday load forecasting. In [73], radial basis function (RBF) neural network is used for the short-term load forecasting. Authors in [74] combined the RBF neural network with the adaptive neural fuzzy inference system (ANFIS) to adjust the prediction by using the real-time electricity price. In [75], the short-term day-ahead forecasting problem is addressed based on a grid method combined with back-propagation (BP) training of RBF neural networks. Authors in [76] also proposed a neural network-based predictor for very short-term load forecasting. The approach considers the load values of the current and previous time steps as the input to predict the load value at the coming time step. In [77], an ensemble of extreme learning machines (ELMs) is used to learn and forecast the total load of the Australian national energy market. The proposed methodology not only made use of the supreme ELM learning efficiency for self-adaptive learning but also used the ensemble structure to mitigate the instability of the forecasts. The k-nearest neighbor (KNN) algorithm is also reported to be successful for load forecasting in [75]. KNN is a widely used approach due to its computational simplicity, however, training requires considerable feature extraction work. Authors in [78] proposed a dedicated input selection scheme to work with the hybrid forecasting framework using wavelet transformation and Bayesian neural network. In the pioneering work of [72], the LSTM model is proposed for short term residential load forecasting, however, the microgrid stabilization using energy forecast.

2.9 Summary

In this chapter, a complete review on the state-of-the-art control systems for DC microgrids and their related concepts are given. The challenges were discussed and several possible solutions were studied. Throughout the next chapters of this thesis, several distributed controllers and state estimators are designed that can be used for different microgrid requirements. In each design, several constrains such as network bandwidth, communication pattern, and energy forecasts are considered to fully stabilize the case studies.

Chapter 3

Distributed Event-Triggered Control Based on Publish-Subscribe Communication Pattern

This chapter introduces the complete design, analysis, and performance evaluation of the proposed distributed event-triggered control and estimation strategy for DC microgrids. The primary objective of this work is to efficiently stabilize the microgrid grid voltage and to further balance the energy level of the energy storage systems (ESSs). The locally installed distributed controllers are utilised to reduce the number of transmitted packets and battery usage of the installed measurement units, based on the proposed event-triggered communication scheme. Also, to reduce the network traffic, an optimal observer is employed, which utilizes a modified Kalman consensus filter (KCF) to estimate the state of the DC microgrid via the distributed measurement units. Furthermore, in order to effectively provide an intelligent data exchange mechanism for the proposed event-triggered controller, the publish-subscribe communication model is employed to set up a distributed control infrastructure over industrial wireless sensor networks (WSNs). The performance of the proposed control and estimation strategy is validated via the simulations of a DC microgrid composed of renewable energy sources (RESs). The results confirm the suitability of the proposed strategy for the optimal utilization of the communication infrastructure in DC microgrids. The results of this chapter formed the basis for publishing [4].

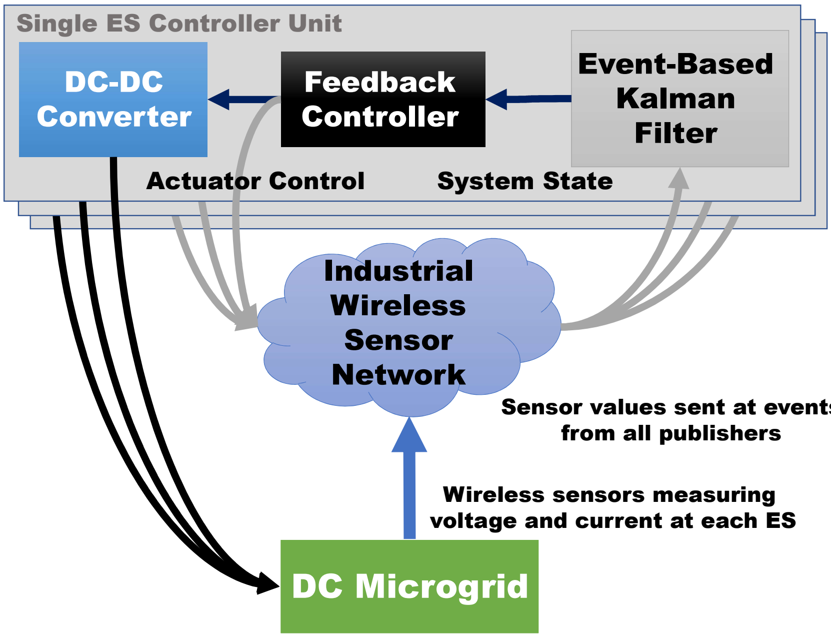

Figure 3.1: Block diagram of the proposed distributed event-triggered control and estimation strategy for the DC microgrids.

Figure 3.1 presents the structure of the distributed controller node. A state estimator is proposed to reduce the number of data transmissions with a relatively small degradation in the estimation performance. The send on delta (SoD) event-generation condition (i.e. δ) is used in which the data from measurement units is transmitted only if its values changes beyond δ. A case study of a 10-bus microgrid is used to validate the proposed scheme, where the control objectives are chosen as the voltage stability and power-sharing among the ESSs. Furthermore, multiple distributed ESSs replace the need for a central energy storage system, which increases the reliability, power quality, and reduces the power transmission losses.

The contributions of the work in this chapter can be summarized as:

1. Regulating the voltage of the DC microgrid using a novel distributed control strategy, in order to effectively control the output voltages of the DC-DC converters connected to the ESSs. Also, the controller is fulfilling two objectives, i.e. balancing the energy level of the ESSs together with the voltage regulation.

2. Proposing an SoD-based Kalman filter, as a state estimator, for feedback control of the DC-DC converter to balance the energy level by the distributed controllers, along with the voltage regulation in the microgrid.

The developed filter receives the real-time sensors' data from the WSN, where the event-triggering function is based on the SoD sampling. The energy cost at each sensor node is also analyzed and compared to the traditional digital control system with the time-triggered sampling functionality. It is shown the network traffic is significantly reduced, due to the deployed procedure.

3. Utilizing the publish-subscribe model for the implementation of the event-triggered control strategy. It is shown that the model is seamlessly suitable for the event-based coordination of the distributed controllers.

The rest of this chapter is organized as follows. Section 3.1 describes the components of the DC microgrid, in which a microgrid model is developed based on the proposed distributed control and estimation strategy. In Section 3.2, the proposed distributed controller design is discussed, and the structure of the Kalman filter as a state estimator is described, where a modification is suggested for the filter in order to adapt to the SoD event-based sampling. The stability and steady-state analysis are provided in Section 3.5. In Section 3.6, a case study is given to validate the performance of the controller using the simulations of a 10-bus DC microgrid. The chapter is concluded in Section 3.7.

3.1 Modelling of DC microgrid dynamics

A DC microgrid essentially consists of four main components, including the DGs, ESSs, power converters (DC-DC or DC-AC), and loads. Figure 3.2 indicates the common configuration of a DC microgrid, along with its constituent components.

The main objective of the ESSs is to compensate for the fast voltage dynamics caused by the load fluctuations in the DC microgrid. They are utilized to stabilize the voltage and to increase the power quality. The widely used ESSs are electrochemical batteries, super capacitors, and flywheels which are easily deployable in a microgrid due to their natural DC output. A DC microgrid has two main operating modes: islanded mode and connected mode. The distributed secondary controller proposed in this work can operate in both modes. A maximum power point tracking (MPPT) scheme is used to ensure that maximum power is absorbed from the intermittent distributed energy sources (DERs) such as photovoltaics. Here, the DGs and DC-DC converters in the main grid are modeled as the current sources, in which the variable injected current is related to their output power. In this way, the DC microgrid only gets connected to the main grid if enough power is not available from the installed DGs for load balance.

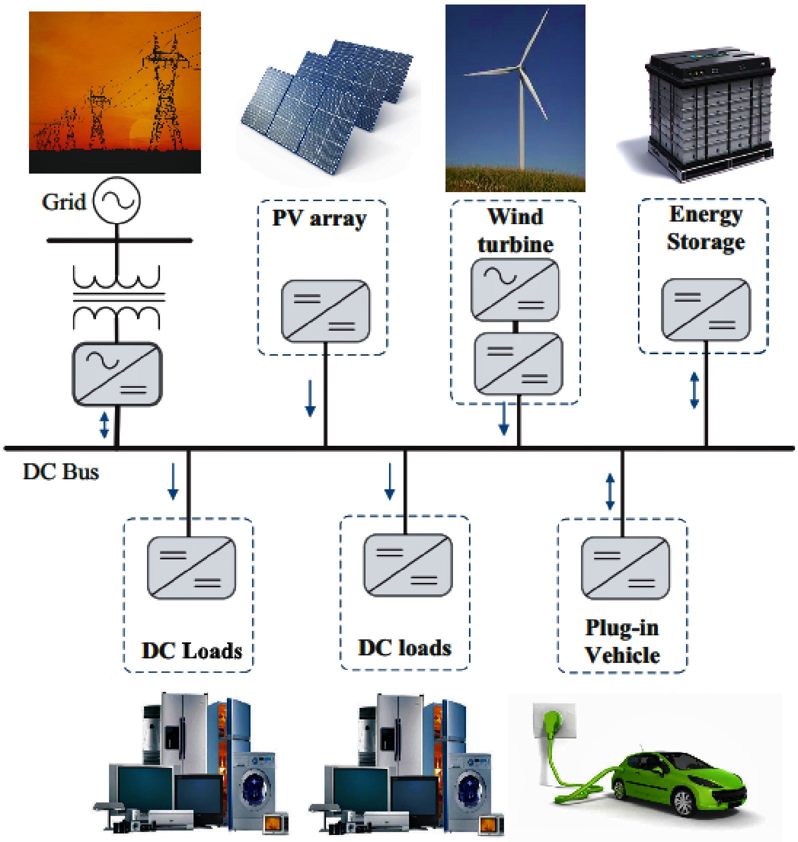

Figure 3.2: Schematic of a DC microgrid with the main constituent components.

3.2 Control system modelling based on publish-subscribe pattern

A bidirectional DC-DC boost converter provides an interface between the ESS and the DC microgrid. The boost converter also acts as a bidirectional charger. A voltage-current (V-I) droop controller regulates the DC-DC converter output voltage with the reference voltage of v_i^*, which is calculated based on the microgrid voltage reference v^{mg} and the locally measured output current i_i. In the proposed strategy, the droop control is improved by considering two extra control signals $u_i^{\overline{v}}$, u_i^e in the current reference signal v^*:

$$v_i^* = v^{mg} - F_i r_i (i_i - u_i^{\overline{v}} - u_i^e) \tag{3.1}$$

where the voltage stabilization control signal $u_i^{\overline{v}}$ is defined to regulate the average microgrid bus voltage, and the power-sharing control signal u_i^e is proposed to balance the energy level between the ESSs and to maintain it through the load sharing. In a decentralized V-I droop control, the load is normally shared between the ESSs in inverse proportion to their virtual resistances r_i. The virtual resistance (i.e. r_i) is merely used for the voltage regulation at the converters of the ESSs, therefore it is lossless.

The DC microgrid is subject to high-frequency harmonics due to the pulse width modulation (PWM) switching control scheme used for the converters. A low-pass filter with the cut-off frequency of ω_i^c should be used to reduce the harmonics, and to prevent the resulting instabilities in the grid.

$$F_i = \frac{\omega_i^c}{s+\omega_i^c} \tag{3.2}$$

where ω_i^c is a constant parameter considering the switching control of the DC-DC converters. However, with an appropriate selection of an upper-bound value, it can be approximated to a time-invariant parameter.

The current regulation can be achieved in two stages [79]. At the first stage, a proportional-integral (PI) voltage controller G_i^v is defined in (3.3) to set the converter current reference to regulate the output voltage of the ESSs:

$$i_i^* = G_i^v\left(v_i^* - v_i\right), \;\; G_i^v = p_i^{vp} + \frac{p_i^{vi}}{s} \tag{3.3}$$

At the second stage, the current controller sets the duty cycle of the PWM switching to control the bipolar junction transistors (BJTs) of the converter and to regulate the output current.

In order to balance the energy level, a PI controller G_i^e is defined in (3.4) to set the energy level e_i to the local estimate of the average energy level of the ESSs. Due to different capacities for the ESSs, per-unit energy level is used for the power balancing signal.

$$u_i^e = G_i^e\left(e_i - \bar{e}_i\right), \;\; G_i^e = p_i^{ep} + \frac{p_i^{ei}}{s} \tag{3.4}$$

Another PI controller $G_i^{\overline{v}}$ is used for the voltage regulation of the microgrid, where the local estimate of the average bus voltage is regulated to the voltage reference of the microgrid:

$$u_i^{\overline{v}} = G_i^{\overline{v}}\left(v^{mg} - \overline{v}_i\right), \;\; G_i^{\overline{v}} = p_i^{\overline{v}p} + \frac{p_i^{\overline{v}i}}{s} + \frac{p_i^{\overline{v}ii}}{s^2} \tag{3.5}$$

In (3.5), the double-integral is used to maintain the overall stability, and to eliminate the steady-state error. An average state estimator is designed for each ESSs, using the local measurements and information from the neighbouring ESSs. The estimator updates the local estimates of the average energy level and bus voltage of the ESSs, then the controller tries to regulate the average estimates to the nominal values of the microgrid.

3.3 Average consensus protocol for distributed controllers

Each ESS has an average state estimator that uses the local measurements and information from the neighboring ESSs to update the local estimates of the average ESS per-unit energy level $\overline{e}_i$, average microgrid bus voltage $\overline{v}_i$, and average ESS output current. The average state estimator implements a distributed average consensus protocol for tracking the dynamic signals from [80].

The ESS are connected by a sparse communication graph $\mathcal{G}(\mathcal{V}, \mathcal{E})$ with the nodes $\mathcal{V} = (1, ..., \mathcal{N})$ and edges $\mathcal{E}$. Each graph node represents an ESS, and the graph edges represent communication links between them. $(i, j) \in \mathcal{E}$ if there is a link allowing information flow from node i to node j. The neighbors of i node are given by $\mathcal{N}_i$, where $j \in \mathcal{N}_i$ if $(j, i) \in \mathcal{E}$. The graph adjacency matrix is given by $A = [a_{ij}] \in R^{N\times N}$, where $a_{ij} > 0$ if $(j, i) \in \mathcal{E}$ and $a_{ij} = 0$ otherwise.

For the ith ESS, let x_i be a local state variable, and let $\overline{x}_i$ be a local estimate of the average value of that state for the ESSs. The ith ESS receives the average state estimates from its neighbours $j \in \mathcal{N}_i$, and its average state estimator implements the following distributed average consensus protocol ($\overline{x}$ is the average value of vector elements):

$$\overline{x}_i = x_i + \int \sum_{j\in\mathcal{N}_i} a_{ij}(\overline{x}_j - \overline{x}_i)dt \tag{3.6}$$

Each node in the network has in-degree $d_i = \sum_{j=1}^{N} a_{ij}$ and out-degree $d_i^o = \sum_{j=1}^{N} a_{ji}$. Moreover, the graph is balanced if $d_i = d_i^o$ for all the nodes. The graph degree matrix is given by $\mathbf{D} = diag\{d_i\}$ and the graph Laplacian matrix is also given by $\mathbf{L} = \mathbf{D} - \mathbf{A}$. The global dynamics of the distributed average consensus protocol are given by:

$$\dot{\overline{\mathbf{x}}} = \dot{\mathbf{x}} - \mathbf{L}\overline{\mathbf{x}} \tag{3.7}$$

Applying the Laplace transform yields the following transfer function matrix for the average consensus protocol [80]:

$$G^{avg} = \frac{\overline{\mathbf{X}}}{\mathbf{X}} = s(sI_N + \mathbf{L})^{-1} \tag{3.8}$$

$\overline{\mathbf{X}}$ and $\mathbf{X}$ are the Laplace transforms of $\overline{x}$ and x, respectively.

For a balanced communication graph with a spanning tree, the steady-state gain of the average consensus protocol is given by the averaging matrix [81]:

$$\lim_{s \to 0} G^{avg} = Q, \text{where } [Q]_{ij} = \frac{1}{N} \tag{3.9}$$

The final value theorem shows that for a vector of step inputs, the elements of $\overline{\mathbf{x}}(t)$ converge to the global average of the steady-state values $\mathbf{x}^{ss}$:

$$\lim_{t \to \infty} \overline{\mathbf{x}}(t) = \lim_{s \to 0} G^{avg} \lim_{t \to \infty} s\mathbf{X} = Q\mathbf{x}^{ss} = \langle \mathbf{x}^{ss} \rangle \, \underline{1} \tag{3.10}$$

3.4 Design of event-based Kalman filter

Consider the following linear system which is the state space realization of distributed average consensus protocol transfer function in each controller:

$$\begin{aligned} \dot{x} &= Ax\left(t\right) + w\left(t\right) \\ y(t) &= Cx(t) + v(t) \end{aligned} \tag{3.11}$$

where $x \in \mathrm{R}^{\mathrm{n}}$ is the estimated state and $y \in \mathrm{R}^{\mathrm{p}}$ is the output measurement. The process noise $w\left(t\right)$ and measurement noise $v(t)$ are the uncorrelated, zero-mean white Gaussian random signals, fulfilling the following:

$$E\left\{w(t); w(s)'\right\} = Q; \delta(t-s) \tag{3.12}$$

$$E\left\{v(t); v(s)'\right\} = R; \delta(t-s) \tag{3.13}$$

$$\tag{3.14}$$

where w_i and v_j are the i-th and j-th elements of the w and v, respectively. Also, R is the measurement noise covariance, and Q is the process noise covariance. It is assumed that the i-th sensor only transmits the data when the difference between the current sensor value and the previously transmitted value is greater than δ_i.

The states are also estimated periodically with the period of T. For simplicity, it is assumed that there is no delay in the sensor data transmission. Using the SoD method, the estimator continuously with a period of T demands the data from the sensors no matter the data becomes available. For example, if the last received i-th sensor value is y_i at the time $t_{last,i}$, and there is no i-th sensor data received for $t > t_{last,i}$, then the estimator can estimate $y_i(t)$ as:

$$y_i\left(t_{last,i}\right) - \delta_i \leq \; y_i\left(t\right) \leq y_i\left(t_{last,i}\right) + \delta_i \tag{3.15}$$

The last received i-th sensor data is used to compute the output $y_{computed,i}$ even if there is no sensor data transmission:

$$y_{computed,i}\left(t\right) = y_i\left(t_{last,i}\right) = C_i x\left(t\right) + v_i\left(t\right) + \Delta_i\left(t, t_{last,i}\right) \tag{3.16}$$

where $\Delta_i\left(t, t_{last,i}\right) = y_i\left(t_{last,i}\right) - y_i\left(t\right)$ and:

$$\left|\Delta_i\left(t, t_{last,i}\right)\right| \leq \delta_i \tag{3.17}$$

In (3.16), the measurement noise increases from $v_i\left(t\right)$ to $v_i\left(t\right) + \Delta_i\left(t, t_{last,i}\right)$. If $\Delta_i\left(t, t_{last,i}\right)$ is assumed to have the uniform distribution with (3.17), then the variance of $\Delta_i\left(t, t_{last,i}\right)$ is $\frac{\delta_i^2}{3}$, which is added to the *measurement noise covariance* in standard Kalman filter $\mathrm{R}(i, i)$ when (3.16) applies.

Improved Kalman Measurement Update Algorithm: An algorithm is proposed here to appropriately improve the *measurement update* part of the standard Kalman filter algorithm, which is adapted to the SoD event-generation condition by increasing the measurement noise covariance $\overline{R}_k$:

1. Initialization set

$$\begin{aligned} &\hat{x}^-(0), P_0^- \\ y_{last} &= C\hat{x}^-\left(0\right) \end{aligned} \tag{3.18}$$

2. **Measurement update**

$$\overline{R}_k = R \tag{3.19}$$

if *i*-th measurement data are received

$$\hat{y}_{last,i} = y_i\left(kT\right) \tag{3.20}$$

else

$$\overline{R}_k\left(i, i\right) = \overline{R}_k\left(i, i\right) + \frac{\delta_i^2}{3} \tag{3.21}$$

end if

$$\begin{aligned} K_k &= P_k^- C'(CP_k^- C' + \overline{R}_k)^{-1} \\ \hat{x}\left(kT\right) &= \hat{x}^-\left(kT\right) + K_k(\hat{y}_{last} - C\hat{x}^-(kT)) \\ P_k &= (I - K_k C)P_k^- \end{aligned} \tag{3.22}$$

3. Project ahead

$$\hat{x}^{-}((k+1)T) = \exp(AT)\hat{x}(kT)$$
$$P_{k+1}^{-} = \exp(AT)P_k \exp(A'T) + Q_d \tag{3.23}$$

where Q_d is the process noise covariance for the discretized dynamic system; y_{last} is defined as (3.24):

$$y_{last} = [y_{last,1}, y_{last,2}, \ldots, y_{last,p}]' \tag{3.24}$$

The presented event-triggered Kalman filter has been developed to implement the distributed controller and estimator as an NCS. It should be noted that in the proposed event-triggered observer, convergence is obtained by using the Kalman optimal observer. However, choosing the lower values of δ_i would result in a considerable reduction in the convergence time [39]. The controllers only receive updates from their neighbour controllers which are reflected in the **L** matrix of the transfer function that has been realized. Distributed average consensus is then achieved for each controller based on the number of neighbour controllers. Also, the higher the number of adjacent controllers is, the faster the estimator would converge.

3.5 Global dynamics and stability analysis

Figure 3.3 presents the block diagram of the feedback loop for each of the distributed ESS controllers. The voltage regulation dynamics of the grid forms a multiple-input multiple-output (MIMO) linear system. If V^{mg} is the Laplace transform of the voltage reference of the grid, the distributed control dynamics can be expressed as (3.25):

$$V^* = V^{mg}\underline{1} - Fr\left(I - G^{\overline{v}}\left(V^{mg}\underline{1} - \overline{V}\right) - G^{e}\left(E - \overline{E}\right)\right), \tag{3.25}$$

where

$$F = diag\{F_i\} \tag{3.26}$$
$$r = diag\{r_i\} \tag{3.27}$$
$$G^{\overline{v}} = diag\left\{G_i^{\overline{v}}\right\} \tag{3.28}$$
$$G^{e} = diag\{G_i^{e}\} \tag{3.29}$$
$$\overline{V} = G^{avg}V \ and \ \overline{E} = G^{avg}E \tag{3.30}$$

The grid-connected rectifier, the constant power loads, as well as the generation sources (i.e. operate under the MPPT algorithm), can act as the positive or negative current sources, while the ESSs act as the bus voltage regulation units in the DC microgrid. To formulate the bus voltage regulation dynamics, power sources can be modelled by a parallel current source and resistance. Modern DC-DC converters operate at a high switching frequency with one switching period delay (i.e. T_s) in the current control mode. In order to model the DC-DC converter, a control structure as shown in Figure 3.4 is used, in which the bus voltage regulation dynamics is designed as an outer-loop between the output voltage of the ESS v_i^*, and the local bus voltage v_i [82]. Moreover, the transfer function for the internal loop is given by $H_i^{v_{ol}}$.

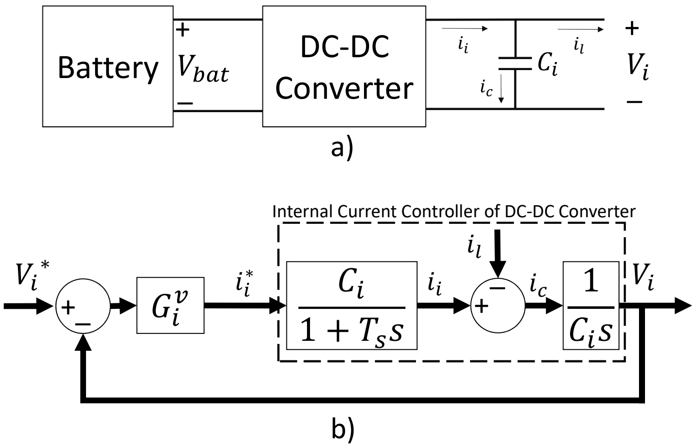

Figure 3.3: Internal model of the ESS: (a) DC-DC converter circuit; (b) block diagram of the local converter controller.

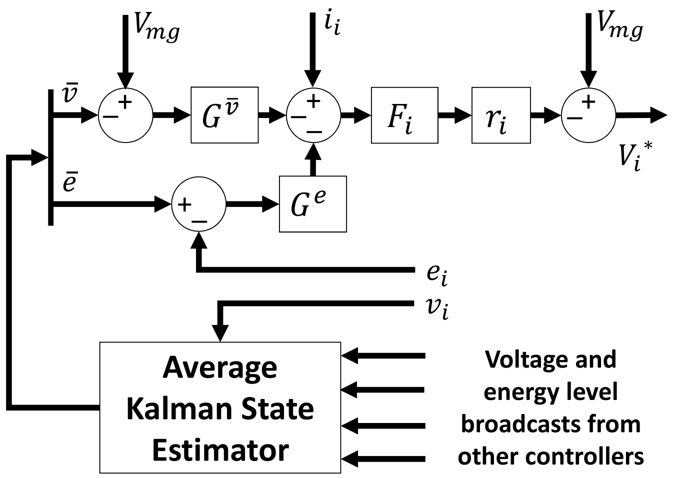

Figure 3.4: Block diagram of the proposed distributed feedback controller.

$$H_i^{v_{cl}} = \frac{H_i^{v_{ol}}}{1 + H_i^{v_{ol}}} \ , \ \ H_i^{v_{ol}} = \frac{G_i^v}{sC_i(T_s s + 1)} \tag{3.31}$$

Therefore, the local bus voltage closed-loop transfer function of the DC microgrid is given by:

$$V{=}H^{v_{cl}}V^*, \qquad H^{v_{cl}}{=}diag\{H_i^{v_{cl}}\} \tag{3.32}$$

The output currents of the ESS can be obtained from multiplying the bus voltages with the bus admittance matrix, constructed based on the line and load impedances:

$$I = YV \tag{3.33}$$

A first order model is used for the battery per-unit energy level charging and discharging:

$$\dot{e}_i = -\frac{v_i i_i}{e_i^{max}} \tag{3.34}$$

where e_i^{max} is the maximum energy capacity of the i-th ESS. The global energy level dynamics is modeled as (3.35):

$$E = MYV, \ \ M = diag\{-\frac{v^{mg}}{e_i^{max} s}\} \tag{3.35}$$

The global closed-loop voltage regulation dynamics can be described by the multiple output linear system as (3.36):

$$\begin{aligned} V = [(H^{v_{cl}})^{-1} + FrY + FrG^{\overline{v}}G^{avg} \\ -FrG^{e}\left(I_N - G^{avg}\right)MY]^{-1}V^{mg}\left(I_N + FrG^{\overline{v}}\right)\underline{1} \end{aligned} \tag{3.36}$$

In the above strategy, it is assumed the local distributed controllers can exchange data with the other controllers in a continuous mode. It should also be noted that this assumption is not feasible in the cases involving the NCSs. An event-based Kalman filter is proposed to overcome this problem. Using this filter, the distributed control system can be realized with the SoD event triggering condition.

3.5.1 Stability and steady-state analysis

Assuming v^{mg} be the control reference voltage. In this case, input to the global closed-loop voltage dynamics is given by:

$$V^{mg} = \frac{v^{mg}}{s} \tag{3.37}$$

The steady-state DC microgrid bus voltages are obtained by applying the final value theorem to (3.37):

$$\begin{aligned} v^{ss} &= \lim_{s\to 0} sV \\ &= \lim_{s\to 0}[s^2\left(H^{v_{cl}}\right)^{-1} + s^2 FrY + s^2 FrG^{\overline{v}}G^{avg} \\ &-s^2 FrG^e\left(I_N - G^{avg}\right)MY]^{-1} s^2 v^{mg}\left(I_N + FrG^{\overline{v}}\right)\underline{1} \end{aligned} \tag{3.38}$$

The steady-state bus voltages can be reached to based on the following limits:

$$\begin{aligned} \lim_{s\to 0} s^2 G^{\overline{v}} &= G^{\overline{v}ii}, \text{where } G^{\overline{v}ii} = \text{diag}\{k_i^{\overline{v}ii}\} \\ \lim_{s\to 0} sG^e &= G^{ei}, \text{where } G^{ei} = \text{diag}\{k_i^{ei}\} \\ \lim_{s\to 0} sM &= M_0, \text{where } M_0 = \text{diag}\{-\frac{v^{mg}}{e_i^{max}}\} \\ \lim_{s\to 0} G^{avg} &= Q, \lim_{s\to 0} Y = Y_0,\ \lim_{s\to 0} F = I_N, \\ &\text{and} \lim_{s\to 0}\left(H^{v_{cl}}\right)^{-1} = I_N \end{aligned} \tag{3.39}$$

therefore,

$$v^{ss} = \left[r\left(G^{\overline{v}ii}Q - G^{ei}(I_N - Q)M_0 Y_0\right)\right]^{-1} v^{mg}(rG^{\overline{v}ii})\underline{1} \tag{3.40}$$

which yields

$$\left[(G^{ei})^{-1}G^{\overline{v}ii}Q - (I_N - Q)M_0Y_0\right] v^{ss} = v^{mg}(G^{ei})^{-1}G^{\overline{v}ii})\underline{1} \tag{3.41}$$

Furthermore, as shown in (3.39), without the double-integral gain of the voltage controller, the steady-state response would be dominated by the energy balancing control signal; to verify that the average steady-state voltage is equal to the reference voltage of the microgrid, each side of (3.41) is multiplied by the averaging matrix Q. Since the column sums of $(I_N - Q)$ are equal to zero, $Q(I_N - Q) = 0_{N\times N}$. Following (3.10) yields:

$$\begin{aligned} Q\left((G^{ei})^{-1}G^{\overline{v}ii}Qv^{ss}\right) &= v^{mg}Q\left((G^{ei})^{-1}G^{\overline{v}ii}\underline{1}\right) \\ \langle v^{ss}\rangle \left\langle (G^{ei})^{-1}G^{\overline{v}ii}\underline{1}\right\rangle \underline{1} &= v^{mg}\left\langle (G^{ei})^{-1}G^{\overline{v}ii}\underline{1}\right\rangle \underline{1} \\ \langle v^{ss}\rangle &= v^{mg} \end{aligned} \tag{3.42}$$

3.6 Experimental results and discussion

The performance evaluation of the proposed controller is thoroughly presented in this section through a case study of a 10-bus microgrid. As also depicted in Figure 3.1, each distributed controller receives the events from neighbor ESS sensors. The deployed sensors measure the bus voltages and currents.

It has been discussed in detail that the network traffic, and the battery energy usage of sensor nodes in a WSN, would be reduced significantly if an event-triggered strategy is used. The event-triggered control stops the unnecessary data exchange in a shared medium. Once an event is generated, the data must be sent to the controller as fast as possible, in order to prevent the deviation of system behaviour from the stable margin.

In the proposed distributed control, there are two different variables that are evaluated in the event-generation condition. First is the bus voltage in which the distributed controller is installed, and second is the ESS per-unit energy level. The conditions of the SoD event-generation for these variables are independent, therefore two thresholds are evaluated in each controller. Each event is then matched with its corresponding topic in the publish-subscribe model; e.g., in the presented case study of the 10-bus system, each bus controller publishes data in two topics related to that bus. Since the network is assumed to be connected, each distributed controller subscribes to the topics of the other neighbours. This is shown in Table 3.1. The MATLAB & Simulink software is employed for the simulation of the DC microgrid and distributed control strategy. Also, the Simscape toolbox is used to simulate the electrical distribution system of the DC microgrid.

Table 3.1: Distributed Controllers and Their Corresponding Topics.

Bus Controller	Voltage SoD Event Topic	Energy SoD Event Topic
Bus 1	voltageBus1	energyBus1
Bus 2	voltageBus2	energyBus2
Bus 3	voltageBus3	energyBus3
Bus 4	voltageBus4	energyBus4
Bus 5	voltageBus5	energyBus5
Bus 6	voltageBus6	energyBus6
Bus 7	voltageBus7	energyBus7
Bus 8	voltageBus8	energyBus8
Bus 9	voltageBus9	energyBus9
Bus 10	voltageBus10	energyBus10

3.6.1 DC Microgrid Configuration

The microgrid used for the case studies is shown in Figure 3.5. The presented DC microgrid incorporates a 10-bus distribution system with the PV generation and 10 battery ESSs.

At bus 1, a 150 kW rated rectifier provides the main connection of the microgrid. Bus 1 also includes 500 m^2 PV generation operated with the MPPT algorithm, rated for 80 kW. Based on the analysis of conventional wiring configurations of the DC microgrids shown in [83] for data centres, $50m \times 24mm$ cables are selected to connect the load buses to bus 1. The buses 1 to 7 have 25 kWh lithium-ion batteries, while the buses 8 to 10 ESSs have 12.5 kWh lithium-ion batteries. The battery ESSs are connected by a sparse communication network to support the proposed distributed event-triggered control. The communication links between the ESSs are bidirectional, meeting the requirements of the distributed control strategy for a balanced communication network. Based on the ETSI EN 300 132-3-1 telecommunications DC distribution standard for data centres, the voltage limits are defined as 380 V$\pm$5% [68].

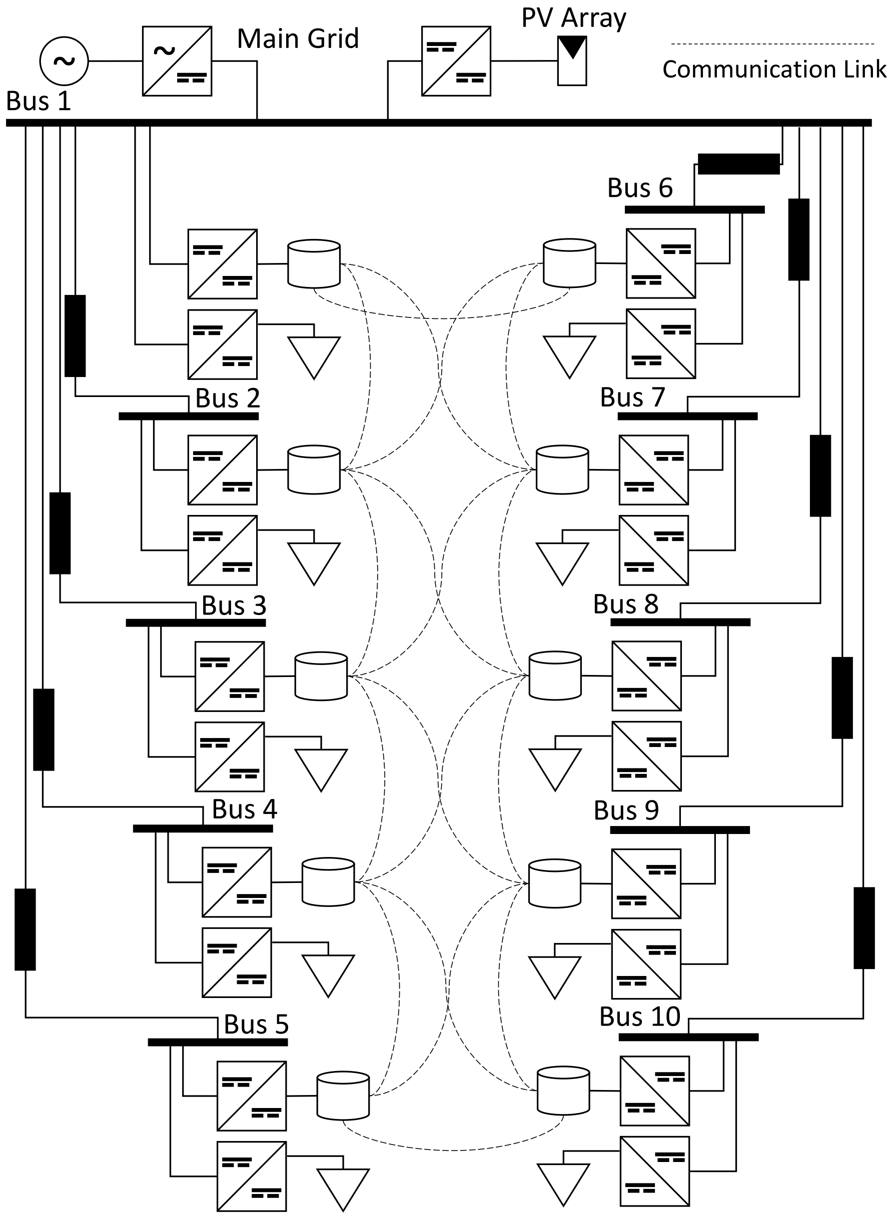

Figure 3.5: Proposed case study of the 10-bus DC microgrid with the ESSs.

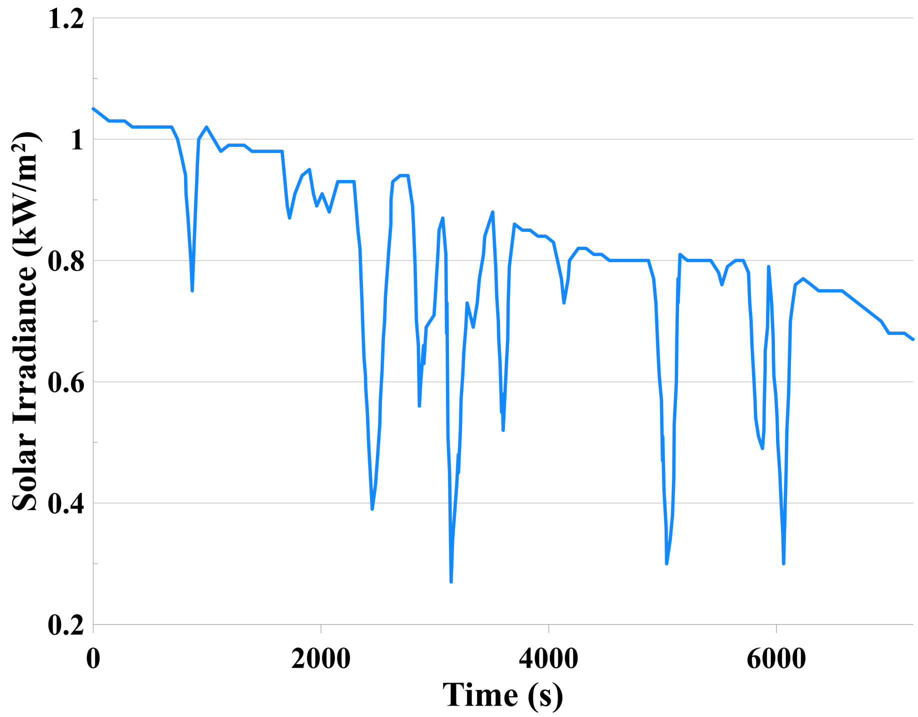

Figure 3.6: Data of the PV solar irradiance used in this case study.

For the case study, 15 kW constant power loads are installed at buses 1 to 5, and 5 kW constant power loads are installed at buses 6 to 10, hence the total load of the microgrid would be 100 kW. The battery ESSs begin with values around half of their energy levels and the initial energy levels are chosen randomly. The bus 1 PV generation with MPPT was simulated based on the modelling approach from [84], using the 1 min resolution irradiance and temperature data for 2 p.m. to 4 p.m. on June 1, 2014, from the NREL Solar Radiation Research Laboratory (SRRL): Baseline Measurement System (BMS), in Colorado. Moreover, the used irradiance data is shown in Figure 3.6. The simulation parameters are also provided in Table 3.3. The graph adjacency matrix A elements a_{ij} are chosen as "1" if there is a connection and "0" if there is no communication link between the buses. The DC load and battery parameters for each bus are given in Table 3.2. The parameters of the proposed event-based Kalman filter are also provided in Table 3.4 for the proposed control strategy. The values for parameters Q and R are experimentally calculated by using try and error as mathematical models for process noise and measurement noise are very complicated.

Table 3.2: Size of the loads and capacity of the batteries installed on each bus in kW and kWh.

Bus	Load Power	Battery Capacity (380 V)
Bus 1	15 kW	25 kWh
Bus 2	15 kW	25 kWh
Bus 3	15 kW	25 kWh
Bus 4	15 kW	25 kWh
Bus 5	15 kW	25 kWh
Bus 6	5 kW	25 kWh
Bus 7	5 kW	25 kWh
Bus 8	5 kW	12.5 kWh
Bus 9	5 kW	12.5 kWh
Bus 10	5 kW	12.5 kWh

3.6.2 Simulation scenario

The simulation scenario is divided into four sections to represent the different modes of operation of the proposed control strategy. The scenario is simulated for both with and without the proposed event-triggered estimation, in order to compare the results of both implementations. Moreover, in another simulation, the performance of the proposed estimator is tested by adding a 100 ms delay in the event transmission. The simulation time is set at 120 minutes (i.e. 7,200 seconds).

Islanded operation with load switching, 0 to 10 min

The DC microgrid begins in the islanded mode. The start load is 60% at all the employed buses. After 5 minutes, the loads are switched at all buses to their 100% nominal values. As shown in Figure 3.9, the energy level of the ESSs at the buses are increased, as the total power from the PV exceeds the total load of the microgrid. After the load switching, ESSs starting to discharge the energy, and the voltage is stabilized around 380 V with zero error, as shown in Figure 3.7 (C).

Grid connected operation with rectifier providing load balancing, 10 to 40 min

At min 10, a grid connection is made with the rectifier in the load balancing mode. Moreover, the ESSs use their 30 kW power capacity to reach a balanced per-unit energy level, as shown in Figure 3.9. A per-unit energy level of 0.45 is reached by the ESSs; 11.25 kWh for the 25 kWh ESSs at buses 1 to 7, and 5.62 kWh for the 12.5 kWh ESSs at buses 8 to 10. The voltage controllers limit the bus voltages of the DC microgrid between 377.3 and 381.6 V (i.e. 1% error), and ensure the average bus voltage remains at the voltage reference of the microgrid, as shown in Figure 3.9 (B). As desired, the average ESS per-unit energy level remains constant around the operating point.

Grid connected operation with main grid providing ESS charging, 40 to 80 min

At min 40, the rectifier operating mode is changed from the load balancing to the ESS charging mode and the injected power increases. The rectifier uses its maximum power capacity of 150 kW to raise the average ESS per-unit energy level to the value of 0.62, as shown in Figure 3.9 (B). The per-unit energy balancing is maintained between the ESSs. The 25 kWh ESSs are charged at a common rate and the 12.5 kWh ESSs are charged at half of this rate. As the ESSs are charged, they adjust their output powers to balance the variable PV generation, and to further regulate the average DC microgrid voltage within 0.05 V of the reference of 380 V, as shown in Figure 3.7 (B).

Islanded operation with sudden main grid disconnection, 80 to 120 min

At min 80, the grid-connected rectifier is suddenly disconnected, initiating the islanded operation. The sudden power imbalance causes the bus voltages of the DC microgrid to fall, with a minimum level of 377.4 V reached. The ESSs react to the fall in the voltage by increasing the corresponding output powers, restoring the microgrid load balance and returning the average bus voltage to the reference with less than 1% (i.e. 2 V) steady-state deviation.

Table 3.3: Parameters of the case study and controller.

R_{dc}	36 mΩ	Voltage	380 V	$p_i^{\bar{v}p}$	500
L_{dc}	7 μH	p_i^{vi}	10	$p_i^{\bar{v}i}$	10
r	0.2533	w_i^c	100 rad/s	$p_i^{\bar{v}ii}$	0.1
p_i^{vp}	10	p_i^{ep}	5000	p_i^{ei}	50

Table 3.4: Parameters of the event-triggered Kalman filter.

$\delta_i(Voltage)$	0.1 V
$\delta_i(Energy)$	0.01 p.u.
Q	0
R	1
T	1 Second

Furthermore, by manually adding the delay of 100 ms in the event transmission via the communication network, it can be seen in Figure 3.8 that the stability throughout the simulation is maintained. It should be noted that the event-triggered control is more prone to instability, due to the delay in the event transmission. This is the reason the voltage profile is higher compared with the ideal scenario. This fact is reflected in the error graph of Figure 3.8 (C).

In the simulation without applying the event-based Kalman filter, each sensor is driven by a synchronous clock, as in a traditional digital control system. For instance, with a sampling period of 1 ms, there should be 40,000 events in the time frame of 40 s. For this specific case study, in 7,200 seconds there should be $7,200 \times 1000 = 72 \times 10^5$ number of generated messages at each bus, but this is much lower with the event-triggered control strategy proposed in this work. The number of generated events at each distributed controller unit of each bus is given in Table 3.5. This also shows that the acceptable performance of the microgrid is kept with a minimum number of transactions among the neighbouring controllers. The total energy loss in the communication is compared in Table 3.6, where the average power consumption of each transceiver is assumed to be 50 mA in the duration of 10 ms at the voltage of 3.3 V (i.e. $e = v \times i \times t$), and the sampling interval is 100 ms for the time-triggered control. When comparing the values of the consumed energy in the nodes in the traditional sample-based control, as well as the proposed event-based one, the effectiveness of the event-based control strategy in terms of the utilization of the resources is evident, as the energy lost in the communication is reduced nearly by 40%. Additionally,

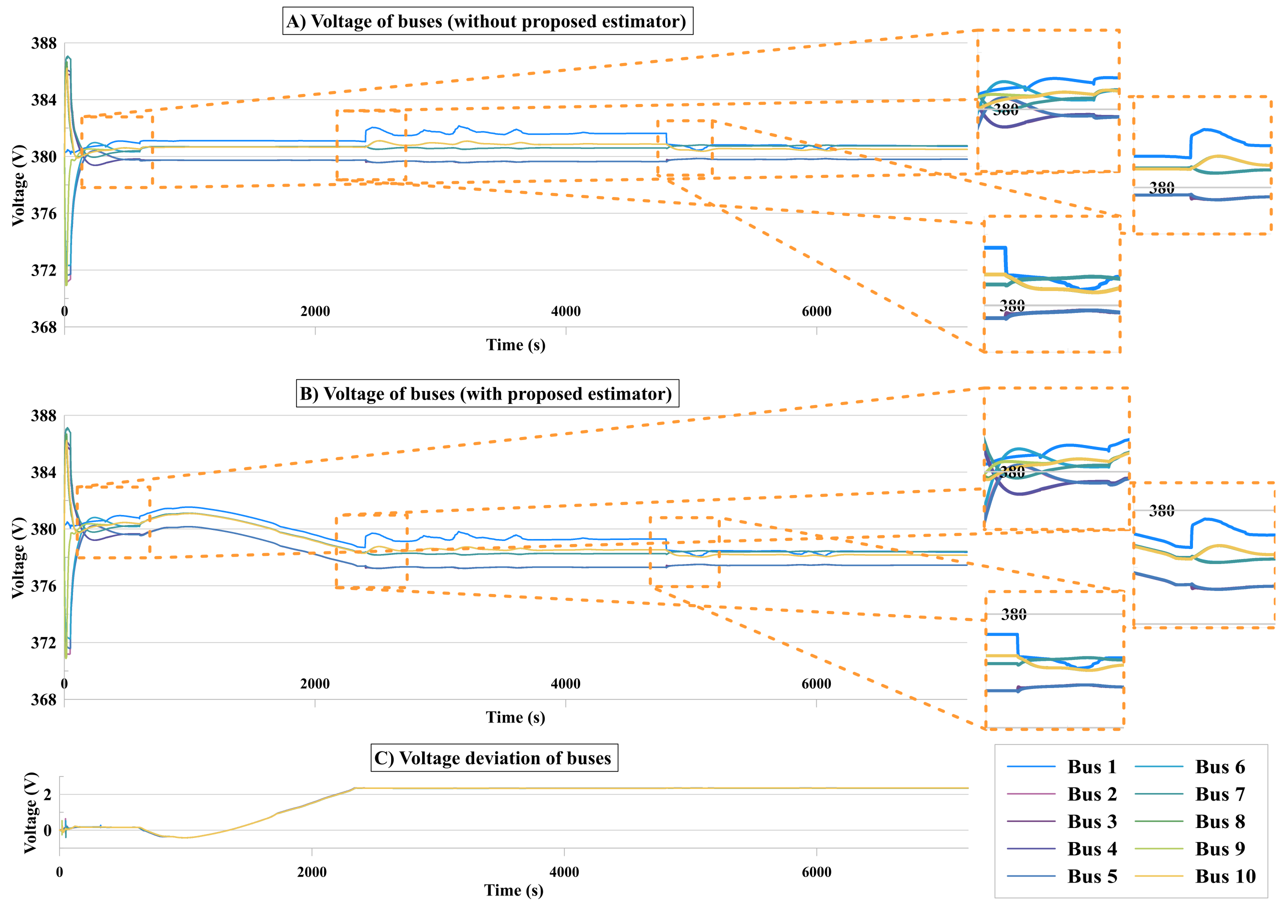

Figure 3.7: Simulation results of the bus voltages for the case study of the 10-bus DC microgrid: A) without the proposed estimator; B) with the proposed estimator; C) error between the two approaches.

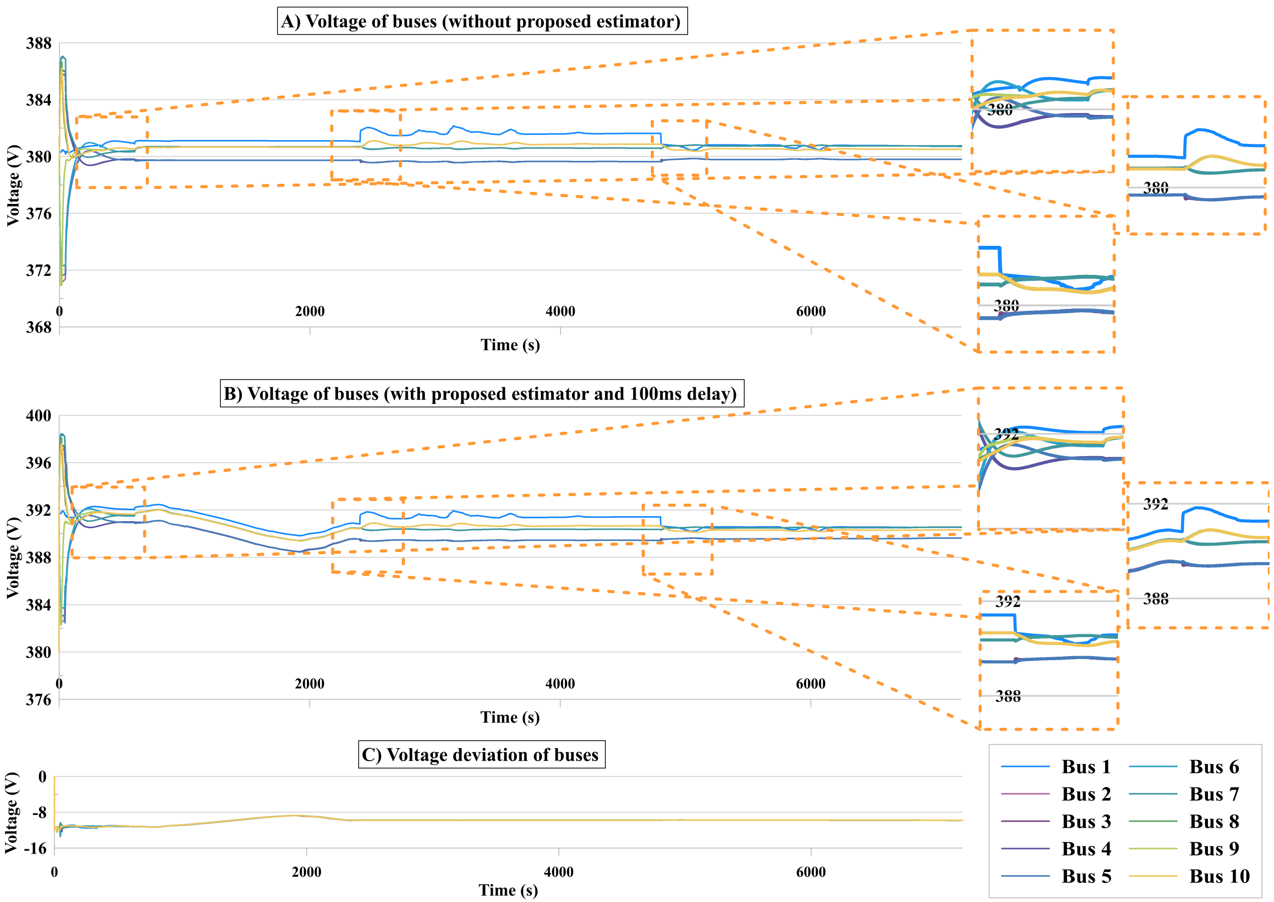

Figure 3.8: Simulation results of the bus voltages for the case study of the 10-bus DC microgrid: A) without the proposed estimator; B) with the proposed estimator (100 ms delay); C) error between the two approaches.

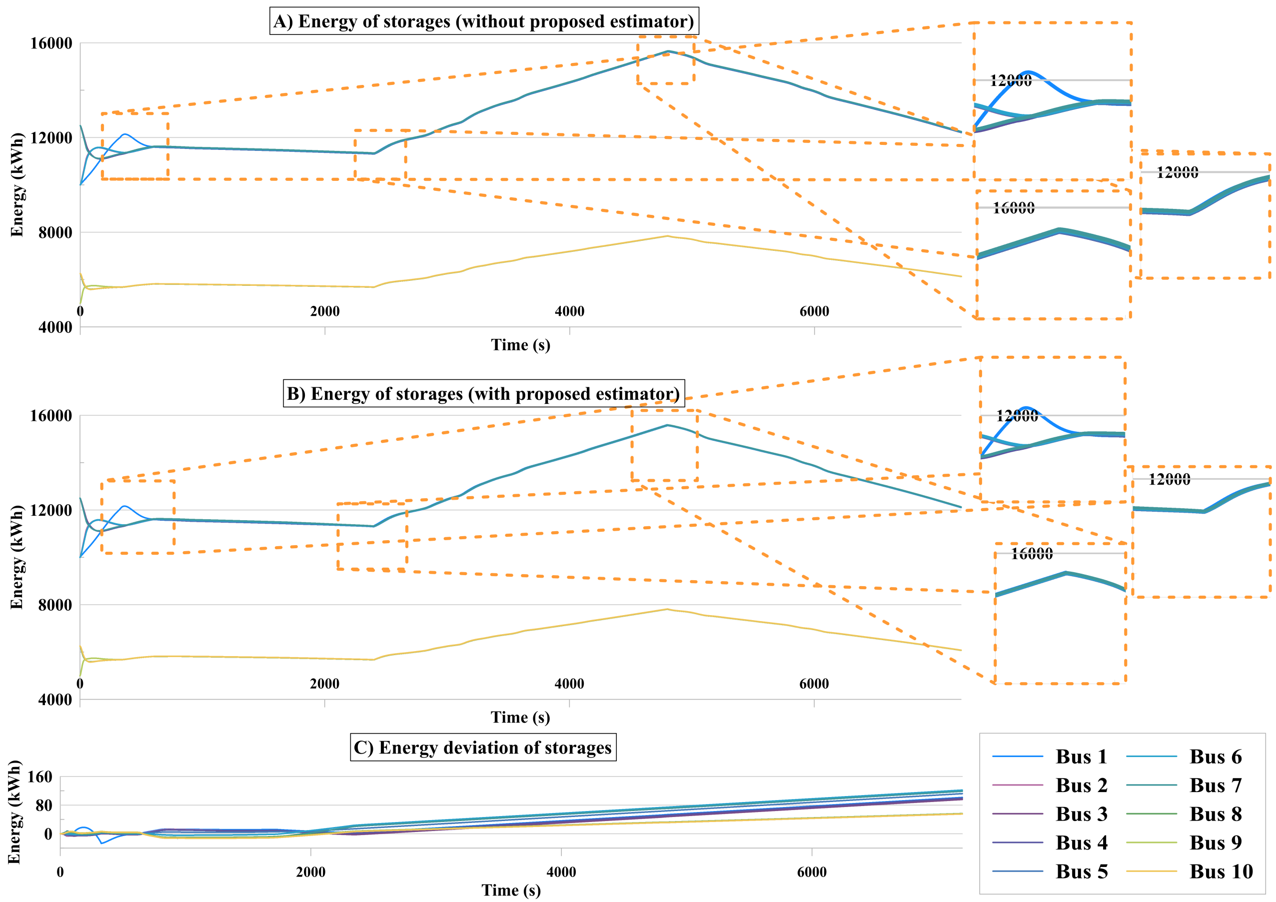

Figure 3.9: Simulation results of the energy level of the ESSs for the case study of the 10-bus DC microgrid: A) without the proposed estimator; B) with the proposed estimator; C) error between the two approaches.

the network traffic is considerably reduced comparing the number of packets generated at each bus with the proposed control strategy to the traditional sample-based control scheme.

Table 3.5: Generated events from each bus controller.

Bus	Number of Published Messages
Bus 1	44,064
Bus 2	44,159
Bus 3	43,920
Bus 4	43,942
Bus 5	44,198
Bus 6	44,180
Bus 7	44,060
Bus 8	44,184
Bus 9	44,693
Bus 10	43,945

Table 3.6: Comparison of the energy cost between the time-triggered and event-based control implementations.

Traditional Digital Control	720,000 messages total	0.34 Wh
Event-Based Control	441,345 messages total	0.2084 Wh

3.7 Summary

This chapter has thoroughly presented the design and performance evaluation of a novel distributed event-triggered control and estimation strategy for DC microgrids. The objective of this controller is to effectively stabilize the voltage of a DC microgrid only by controlling the output voltages of the DC-DC converters connected to the ESSs. The control strategy is able to balance the energy level of the ESSs and regulate the output voltage of the microgrid. An event-based Kalman filter has been designed for the state feedback controller of the DC-DC converters. The Kalman measurement update algorithm has also been modified for the distributed controllers to exchange the data over industrial WSNs. The publish-subscribe model has been proposed for the optimal implementation of the distributed controller, in which the publishers send the data to the specific subscribers without having a subscription knowledge of each node. This has consequently resulted in the smart data exchange, as well as the self-configuration of the devices. The simulated results confirm a significant reduction in the network traffic, while maintaining the performance threshold comparing to the digital control schemes. The total energy cost at each sensor node is considerably reduced compared to the traditional time-triggered sampling control systems.

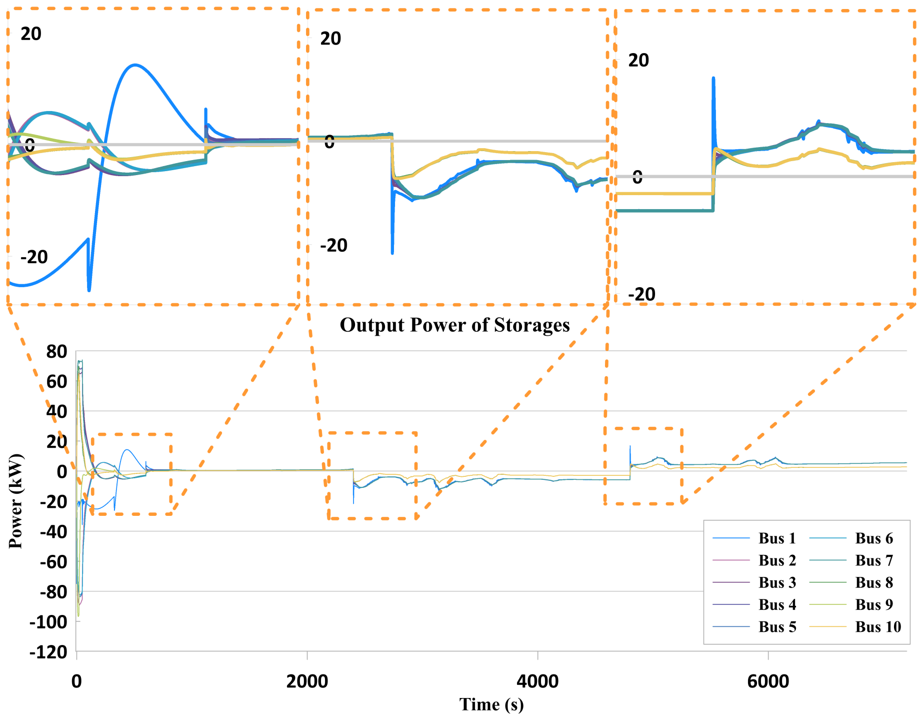

Figure 3.10: Simulation results of the output power of ESSs using the proposed distributed event-triggered estimator.

Chapter 4

Control System Design with Communication Delays and Variable Topologies

The secondary control layer of microgrids is often modelled as a multi-agent distributed system, coordinated based on consensus protocols. Convergence time of consensus algorithm significantly affects transient stability of microgrids, due to changes in communication topology, switching of distributed generations (DGs), and uncertainty of intermittent energy sources. To minimise convergence time in the consensus protocol, this chapter introduces a multilayer event-based consensus control framework, which is resilient to communication delays and supports plug-and-play (P&P) addition or removal of DGs in DC microgrids. A bi-level optimisation algorithm minimises convergence time by selecting an optimal communication topology graph and then adjusts controllers' parameters. Average consensus is achieved among distributed controllers using an event-based consensus protocol, considering non-uniform delays between agents. A realisation method has also been introduced using the directional beamforming technique for topology assignment algorithm based on modern telecommunication technologies. Provided feasibility case study has been implemented on a real-time hardware-in-the-loop (HIL) experimental testbed, to validate the performance of the proposed framework for key purposes of voltage stabilisation and balanced power-sharing in DC microgrids. Exchanging information among components is only executed when an event is generated, which efficiently reduces the number of packets generated in sensor-controller-actuator loops. The results of this chapter formed the basis for publishing [85].

Different datasets can be used for event detection; e.g., output signals [34,86] or state-feedback signals [36]. Output-based event generation approach has been deployed in this chapter, as voltages and currents are only available measurements in DC microgrids. More importantly, communication delays among agents are considered to be non-uniform, which is realistic in a distributed communication scenario. Thus, the main contributions of this chapter can be summarised as follows:

- A novel bi-level optimisation algorithm to minimise the convergence time of distributed controllers based on event-based average consensus.
- A secondary layer controller for DC microgrids, resilient to non-uniform network delays. The proposed control architecture results in fast-voltage recovery by only regulating the output voltage of converters installed on EESs. It is co-designed to tackle the problem of voltage stabilisation and power-sharing together.

The remainder of this chapter is structured as follows. Section 4.1 introduces the proposed multilayer control framework. Distributed event-triggered consensus protocol is described in Section 4.2. In Section 4.3, the proposed topology assignment algorithm for minimum time convergence is discussed and analysed. Then in Section 4.4, secondary control layer system for DC microgrids is designed. The provided case study has been implemented on a real-time HIL experimental testbed, to effectively validate the performance of the proposed architecture for voltage stabilisation and balanced power-sharing in the DC microgrids. Experimental results and analysis are discussed in Section 4.5, and the chapter is concluded in Section 4.6.

4.1 Framework Overview

In the proposed framework for DC microgrids, when a new DG is getting online, i.e. connecting to the network, secondary control systems of DG have to be initialised. Therefore, controllers first seek neighbouring DGs with the required link speed and shortest route. A synchronisation unit in the DG controller is responsible for this task. Then, the unit transmits information of available links to the tertiary layer control system, where a specific bi-level optimisation algorithm defines the communication graph for all DGs in the microgrid.

In this chapter, it is assumed that each bus has an ESS installed on it and ESS is connected to a microgrid via a bi-directional DC-DC converter. ESS acts as an energy buffer for the corresponding DG installed on the bus, and thus, DG will not get connected to the microgrid directly. This forms the concept of virtual or abstracted DG as ESS on each bus hides (abstracts) dynamics of installed DG. It further simplifies distributed control system design as the dynamic interface of RES will be similar for all buses.

The main optimisation factor is a delay in the communication graph, which directly affects the convergence of consensus protocols. This topology change is critical for maintaining microgrid stability since microgrid power continuity and resiliency must be achieved by minimising communication delays.

After the new communication topology is determined, this information will be sent back to DG's synchronisation unit. For security reasons, the whole communication graph is not shared with DGs, and DG controllers gain information for neighbouring connections only. Secondary control systems operate based on event-triggered average consensus protocol with the following two objectives: 1) voltage stabilisation, and 2) state of charge (SoC) balancing of ESSs in the microgrid. The proposed protocol is resilient to communication delays, and further uses communication networks in an event-based manner to reduce overall network traffic.

The structure of the tertiary layer topology assignment unit is shown in Figure 4.1. The process consists of two steps: 1) optimisation of graph topology algorithm based on communication link delays, and 2) computation of tuned parameters for DG controllers. In the next section, the proposed event-triggered consensus protocol is introduced, which forms the basis of the secondary control layer system. Then, the tertiary layer graph optimisation method is discussed, followed by the droop control strategy for mentioned control objectives of the DC microgrid.

4.2 Event-Triggered Average Consensus With Communication Delays

Controller agents are connected via a directed graph $\mathcal{G}(\mathcal{V}, \mathcal{E})$ with nodes $\mathcal{V} = (1, ..., \mathcal{N})$, and edges $\mathcal{E} \subset \mathcal{V} \times \mathcal{V}$. $(i, j) \in \mathcal{E}$ holds if there is a connection from node i to node j. $A = [a_{ij}] \in R^{N\times N}$ is the graph adjacency matrix, where $a_{ij} > 0$ if $(i, j) \in \mathcal{E}$, and $a_{ij} = 0$ otherwise. $d_i = \sum_{j=1}^{N} a_{ij}$ represents the weighted degree of controller v_i. $\mathbf{D} = diag\{d_i\}$ is the degree matrix graph, and $\mathbf{L} = \mathbf{D} - \mathbf{A}$ is the Laplacian matrix graph. A directed graph is connected if there is an undirected path between any pair of vertices.

In this section, after presenting an overview of the proposed framework, some preliminaries on graph theory are given, followed by the proposed event-based consensus protocol for multi-agent systems. It is then shown that the system is input-to-state stable (ISS), by finding the maximum allowed delay.

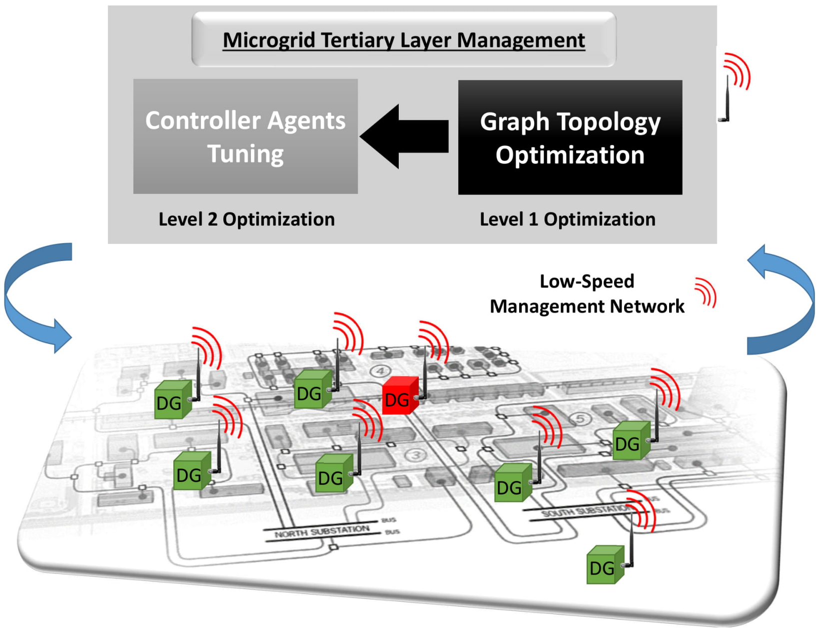

Figure 4.1: The proposed communication network-centric tertiary layer optimiser for distributed controllers in microgrids. The optimization methodology works in the standard configuration of DC microgrid control hierarchy.

4.2.1 Average Consensus Protocol

Considering a continuous-time system of N single integrator agents, classical distributed average consensus protocol in secondary control layer of microgrid architecture is given by:

$$\dot{x}_i = u_i(t) = -\sum_{j=1}^{N} L_{ij} x_j(t) \tag{4.1}$$

where x is value of interest to be shared among agents, and L_{ij} is communication topology Laplacian matrix.

Due to constraints of communication link to transmit continuous-time data streams, we hereby propose the following event-triggered consensus protocol, in which each controller shares its state information at specific event instances:

$$\dot{x}_i = u_i(t) = -\sum_{j=1}^{N} L_{ij} \hat{x}_j(t - \tau_{ij}) \tag{4.2}$$

where $\tau_{ij} > 0$ is communication delay from agent j to agent i, $\hat{x}_j(t - \tau_{ij}) =$

$x_j(t_l^j)$, $t-\tau_{ij} \in [t_l^j - t_{l+1}^j)$. We assume delay only affects communication between two different agents, therefore, $\tau_{ii} = 0$, $\hat{x}_i(t) = x_i(t_l^i)$, and $t \in [t_l^i - t_{l+1}^i)$. Note that delays between agents are not uniform and can have different values.

Increasing sequence $\{t_l^i\}_{l=1}^{\infty}$ and $\{t_{l+1}^i - t_l^i\}_{l=1}^{\infty}$, are event-triggering times and event interval of controller i, respectively. For notation simplicity, let $x(t) = [x_1(t), \ldots, x_n(t)]^T$, $\hat{x}(t) = [\hat{x}_1(t), \ldots, \hat{x}_n(t)]^T$, and $e(t) = [e_1(t), \ldots, e_n(t)]^T = \hat{x}(t) - x(t)$.

The objective here is to find correct event generation conditions to guarantee the stability of the proposed protocol with time delay. To prove Theorem 1, first, it is shown that L has its second smallest eigenvalue at λ_2, using Lemma 1:

Lemma 1. *[87] The Laplacian matrix L of a connected graph $\mathbb{G}$ is positive semi-definite, i.e. $z^T L z \geq 0, \forall z \in \mathbb{R}^n$. Moreover, $z^T L z = 0$ if and only if $z = a\boldsymbol{1}_n, a \in \mathbb{R}$, and $0 \leq \lambda_2(L) K_n \leq L$, where λ_2 is the second smallest eigenvalue of L and $K_n = I_n - \frac{1}{n} 1_n 1_n^T$.*

Now in the proposed Theorem below, we show that DAC protocol is converged to the average of agents' variables under non-uniform communication delays.

Theorem 1. *Assume a strongly connected directional graph with N agents and consensus protocol defined in (4.2). Let $0 < \sigma_i < 1$ be a constant design parameter. Given first event generation time at $t_1^i = 0$, nodes converge to consensus of the average of initial state values under the following event-triggering condition:*

$$e_i^2(t) - \frac{\sigma_i}{4L_{ii}} \sum_{j=1}^{N} L_{ij} (\hat{x}_j(t) - \hat{x}_i(t))^2 \leq 0 \tag{4.3}$$

with convergence rate upper bounded by:

$$\exp\left(-\frac{(1-\sigma_{max}) min_i\{L_{ii}\} \lambda_2(L) t}{2 min_i\{L_{ii}\} + ||L|| \sigma_{max}}\right) \tag{4.4}$$

Proof. First $\delta(t)$ is defined as agents disagreement vector using the following substitution ([5]):

$$x(t) = a\mathbf{1} + \delta(t) \tag{4.5}$$

a is the initial state average, $a = \frac{1}{N} \sum x_i(t)$. Input values to agents are then derived, using (4.5):

$$\begin{aligned}\dot{\delta}(t) = -\sum_{i=1}^{N} L_{ij}(a + \hat{\delta}_j(t)) = -a\sum_{i=1}^{N} L_{ij} - \sum_{i=1}^{N} L_{ij}\hat{\delta}_j(t)) \\ = -\sum_{i=1}^{N} L_{ij}\hat{\delta}_j(t))\end{aligned} \tag{4.6}$$

To prove the stability of the proposed event-triggered DAC protocol in (4.2), the following Lyapunov energy function is employed:

$$V(\delta(t)) = \frac{1}{2}\sum_{i=1}^{N} \delta_i^2 \geq 0 \tag{4.7}$$

with its derivative along the dynamic trajectory (4.2) as:

$$\begin{aligned}\dot{V}(\delta(t)) &= \sum_{i=1}^{N} \delta_i \dot{\delta}_i = \sum_{i=1}^{N} \delta_i \sum_{j=1}^{N} -L_{ij}\hat{\delta}_j(t - \tau_{ij}) \\ &= \sum_{i=1}^{N} (\hat{\delta}_i - e_i(t)) \sum_{i=1}^{N} -L_{ij}\hat{\delta}_j(t - \tau_{ij}) \\ &= \frac{1}{2}\sum_{i=1}^{N}\sum_{j=1}^{N} L_{ij}(\hat{\delta}_j(t - \tau_{ij}) - \hat{\delta}_i(t))^2 \\ &\quad - \sum_{i=1}^{N}\sum_{j=1}^{N} e_i(t) L_{ij}\hat{\delta}_j(t - \tau_{ij}) \\ &= \frac{1}{2}\sum_{i=1}^{N}\sum_{i=1}^{N} L_{ij}(\hat{\delta}_j(t - \tau_{ij}) - \hat{\delta}_i(t))^2 \\ &\quad - \sum_{i=1}^{N}\sum_{j=1, j\neq i}^{N} e_i(t) L_{ij}(\hat{\delta}_j(t - \tau_{ij}) - \hat{\delta}_i(t))\end{aligned} \tag{4.8}$$

To simplify equation (4.8), let:

$$\hat{f}_i = -\sum_{i=1}^{N} L_{ij}(\hat{\delta}_j(t - \tau_{ij}) - \hat{\delta}_i(t))^2 \tag{4.9}$$

Therefore, equation (4.8) becomes:

$$\dot{V}(\delta(t)) = \frac{1}{2}\sum_{i=1}^{N} \hat{f}_i - \sum_{i=1}^{N}\sum_{j=1, j\neq i}^{N} e_i(t) L_{ij}\hat{\delta}_j(t - \tau_{ij}) \tag{4.10}$$

Since $ab < a^2 + \frac{1}{4}b^2, \forall a, b \in \mathbb{R}$, and

$$\sum_{i=1}^{N} \hat{f}_i = -\sum_{i=1}^{N}\sum_{j=1}^{N} L_{ij}(\hat{\delta}_j(t-\tau_{ij}) - \hat{\delta}_i(t))^2 = \hat{\delta}^T(t)L\hat{\delta}(t) \tag{4.11}$$

the following inequality holds:

$$\begin{aligned}\dot{V}(\delta(t)) \leq -\frac{1}{2}\sum_{i=1}^{N}\hat{f}_i - \sum_{i=1}^{N}\sum_{j=1,j\neq i}^{N} L_{ij}e_i^2(t) \\ -\sum_{i=1}^{N}\sum_{j=1,j\neq i}^{N} L_{ij}\frac{1}{4}(\hat{\delta}_j(t-\tau_{ij}) - \hat{\delta}_i(t))^2 \\ = -\frac{1}{4}\sum_{i=1}^{N}\hat{f}_i + \sum_{i=1}^{N} L_{ij}e_i^2(t)\end{aligned}$$

From (4.3) and (4.12), we have:

$$\dot{V}(\delta(t)) \leq -\frac{1}{4}\sum_{i=1}^{N}\hat{f}_i + \sum_{i=1}^{N} L_{ij}e_i^2(t) \leq -\frac{1}{2}(1-\sigma_{max})\hat{\delta}^T(t)L\hat{\delta}(t) \tag{4.12}$$

where $\sigma_{max} = \max\{\sigma_1, \ldots, \sigma_n\}$. In addition, we have:

$$\begin{aligned}\delta^T(t)L\delta(t) &= (\hat{\delta}(t) + e(t))^T L(\hat{\delta}(t) + e(t)) \\ &\leq 2\hat{\delta}^T(t)L\hat{\delta} + 2e^T(t)Le(t) \qquad (4.13)\\ &\leq 2\hat{\delta}^T(t)L\hat{\delta} + \frac{||L||\sigma_{max}}{2\min_i\{L_{ii}\}}\sum_{i=1}^{N}\hat{f}_i \qquad (4.14)\\ &= \left(2 + \frac{||L||\sigma_{max}}{2\min_i\{L_{ii}\}}\right)\hat{\delta}^T(t)L\hat{\delta} \qquad (4.15)\end{aligned}$$

where (4.13) holds because L is a positive semi-definite matrix, $2a^TLb \leq a^TLa + b^TLb, \forall a, b \in \mathbb{R}^n$, and $a^TLa \leq ||L||\ ||a||^2, \forall a \in \mathbb{R}^n$. As a result we have:

$$\begin{aligned}\dot{V}(\delta(t)) &\leq -\frac{(1-\sigma_{max})\min_i\{L_{ii}\}}{4\min_i\{L_{ii}\} + 2||L||\sigma_{max}}\delta^T(t)L\delta(t) \\ &\leq -\frac{(1-\sigma_{max})\min_i\{L_{ii}\}\lambda_2(L)}{2\min_i\{L_{ii}\} + 1||L||\sigma_{max}}V(\delta(t)) \qquad (4.16)\end{aligned}$$

Considering Lemma 1, (4.16) holds, therefore:

$$\dot{V}(\delta(t)) \leq V(\delta(0)) \exp\left(-\frac{(1-\sigma_{max})\min_i\{L_{ii}\}\lambda_2(L)t}{2\min_i\{L_{ii}\}+||L||\sigma_{max}}\right) \tag{4.17}$$

This confirms system (4.2) with triggering condition (4.3) exponentially gets stabilised because $\mathcal{G}$ is connected, and τ_{ij} is finite. □

Remark: The proposed event-triggering function is entirely distributed as convergence law is only dependant on the information of the agent's neighbours. Thus, agents do not need any information for global parameters. However, under this condition, communication delay between the agent and its neighbours should be estimated in advance.

4.2.2 Communication Delay Effect on Average Consensus

In this section, analysis for the effect of communication delay is provided, where maximum allowable time delay for node-to-node communication will be derived. Effect of delay with continuous feedback is treated in literature; e.g., in [88, 89]. Here, it is shown the proposed event-based strategy stabilises the average consensus with respect to ISS, assuming the maximum allowed delay is $\Delta \geq 0$, and the control law will be $u(t) = -L\hat{x}(t-\Delta)$.

Following the change of variables in (4.5):

$$x(t) = a\mathbf{1} + \delta(t) \tag{4.18}$$

where a is the average of initial state values, $a = \frac{1}{N}\sum x_i(t)$. Then we obtain:

$$\dot{\delta}(t) = -L\delta(t-\Delta) - Le(t-\Delta) \tag{4.19}$$

From the extension of ISS for time-delay systems in [90], we use the following Lemma from [91] to find the attraction region under bounded delay:

Lemma 2. *[91] Time-delay consensus problem of (4.19) is ISS with regarding to $e(t-\Delta)$, then there exists functions $\beta \in \mathbb{K}_{\mathbb{L}}$ and $\gamma \in \mathbb{K}$ such that for all $t > 0$ and $0 \leq \Delta \leq \frac{\pi}{2\lambda_N(G)}$:*

$$||\delta(t)|| \leq \beta(||\delta(0)||, t) + \gamma\left(||e_{[-\Delta, t-\Delta[}||_\infty\right) \tag{4.20}$$

From Lemma 2, there exists $\beta \in \mathbb{K}_{\mathbb{L}}$ and $\gamma \in \mathbb{K}$ such that (4.20) holds. Since an upper bound is enforced for $||e||$ by event generation mechanism (4.3), $||\delta(t)||$ converges to a ball around origin as long as the maximum allowed delay is $0 \leq \Delta \leq \frac{\pi}{2\lambda_N(G)}$. It can be shown that size of the ball increases with bound on $||e(t)||$, defined by σ_i.

4.3 Minimum Time Average Consensus

4.3.1 Algebraic Connectivity Optimisation Principles

In the previous section, the necessary event-triggering condition for exponential stability of average consensus protocol has been thoroughly described. However, as mentioned, convergence time can significantly degrade the performance of the controller or destabilise the microgrid. In this section, convergence time is minimised using an optimisation problem for controller agents to achieve consensus in minimal finite time.

As stated in Lemma 1, λ_2 is the second smallest eigenvalue of L. Besides, Theorem 1 has shown in equation (4.17) that λ_2 directly affects the convergence rate of average consensus among agents. Hence, λ_2 is a very important parameter of the graph among all eigenvalues of the Laplacian matrix, which is also called *algebraic connectivity.*

In this work, the aim is to optimise the communication graph to decrease consensus convergence time. Based on equation (4.17), this occurs if the value of algebraic connectivity increases. The following two theorems state the effect of adding and removing a node on algebraic connectivity:

Theorem 2. *Let G be a graph with N vertices. Let $G + e$ be an augmented graph obtained by adding an edge e between two vertices in G. Then eigenvalues of G and $G + e$ are intertwined as follows [92]:*

$$\begin{aligned} 0 = \lambda_1(G) \leqslant \lambda_1(G+e) \leqslant \lambda_2(G) \leqslant \lambda_2(G+e) \leqslant \cdots \leqslant \\ \lambda_N(G) \leqslant \lambda_N(G+e) \end{aligned} \tag{4.21}$$

If $\lambda_2(G)$ is a multiple eigenvalue such that $\lambda_2(G) = \lambda_2(G + e)$, the result of adding an edge does not improve algebraic connectivity. Given that the trace $(L) = \sum_{i=1}^{N} \lambda_i(G) = 2|E|$, it follows that

$$\sum_{i=1}^{N} (\lambda_i(G+e) - \lambda_i(G)) = 2 \tag{4.22}$$

which implies that $0 \leqslant \lambda_2(G + e) - \lambda_2(G) \leqslant 2$. Additionally, we deduce that given a graph with N vertices, the magnitude of λ_i for $i \in N$ tends to increase as $|E|$ increases.

Theorem 3. *Let G be a graph with N vertices. Let $G-e$ be an augmented graph obtained by removing an edge e between two vertices in G such that removal of an edge does not disconnect the graph. Then eigenvalues of G and $G-e$ are intertwined as follows [93]:*

$$0 = \lambda_1(G-e) \leqslant \lambda_1(G) \leqslant \lambda_2(G-e) \leqslant \lambda_2(G) \leqslant \cdots \leqslant \\ \lambda_N(G-e) \leqslant \lambda_N(G) \tag{4.23}$$

We can also deduce that:

$$\sum_{i=1}^{N} (\lambda_i(G) - \lambda_i(G-e)) = 2 \tag{4.24}$$

This implies that $0 \leqslant \lambda_2(G) - \lambda_2(G-e) \leqslant 2$ and that given a graph with N vertices, the magnitude of λ_i for $i \in N$ tends to increase as $|E|$ increases.

According to (4.4), the Lyapunov function $V(x)$ reaches to origin in a finite time, less than the settling time of (exp $\left(-\frac{(1-\sigma_{max})\min_i\{L_{ii}\}\lambda_2(L)t}{2\min_i\{L_{ii}\}+||L||\sigma_{max}}\right)$):

$$\dot{V}(\delta(t)) \leq V(\delta(0)) \exp\left(-\frac{t}{T}\right) \tag{4.25}$$

In [94], the settling time is defined as *"the time required for the response curve to reach and stay within a range of certain percentage (usually 5% or 2%) of the final value"*. For exponentially stable systems, the settling time maps to $4T$ and $5T$, respectively [95], where T is:

$$T = \frac{2\min_i\{L_{ii}\} + ||L||\sigma_{max}}{(1-\sigma_{max})\min_i\{L_{ii}\}\lambda_2(L)} \tag{4.26}$$

Equation (4.26) shows elements of the communication graph that are affecting settling time convergence, i.e. 1) algebraic connectivity of the graph, and 2) event generator parameter σ_{max}. To minimise T, a bi-level optimisation approach is proposed via:

1. Online topology assignment algorithm, which decides optimal communication graph based on highest algebraic connectivity.
2. Distributed tuning of controlling agents by adjusting optimal value for σ_{max} in equation (4.26).

The proposed two-level optimisation approach results in a minimum time event-triggered consensus, which drastically improves the transient response of microgrid in different operational scenarios, such as disconnection of DGs, or contingencies in transmission lines. The following sections describe details of each level of optimisation.

4.3.2 Level 1) Online Topology Optimisation Algorithm

When a new DG is ready to operate, it should first negotiate with servers of the utility company to receive updated communication topology. This requires that the DG controller first obtains the geographical location of DG in the microgrid based on global positioning system (GPS) data, then communicate a new topology. After establishing communication to form a new topology, DG can be connected to a microgrid using circuit breakers. Here, the following cost function is proposed for the tertiary control layer to decide the optimal communication graph:

$$\min\ J_G = \frac{1}{|\mathcal{E}|} \sum_{i=1}^{N} \sum_{j=1}^{N} \tau_{ij} \tag{4.27}$$

where $|\mathcal{E}|$ is the cardinality of graph edge set $\mathcal{E}$, and τ_{ij} is the maximum measured delay on a specific communication edge. According to presented consensus stability requirements (i.e. being a connected graph and exposing a stable gain matrix), the topology assignment algorithm must fulfil the following constraints during switching between updated graphs:

- There must be a spanning tree in the communication graph after plugging a DG;
- DGs must be plugged sequentially to satisfy the uniform boundedness of switching time intervals (i.e. one DG at any time interval).
- Non-zero elements of the adjacency matrix A must be bounded by positive constants at each interval.

Implementation details of the proposed topology assignment for tertiary layer control are provided in Algorithm 1. It searches through all feasible topologies with the maximum nodal degree of d_{max} and finds an optimal solution.

4.3.3 Level 2) Consensus Controller Tuning

In the second level of optimisation, the objective is to find the optimal value for σ_{max} to minimise convergence time defined in equation (4.26), and to provide a feasible event-triggered condition in equation (4.3). Up to this level, a cost-effective communication graph is selected, and only controllers need to be tuned for parameter σ_i. According to Theorem 1, $0 < \sigma_i < 1$, and it directly affects event generation rate, which is limited by the activation time of the medium

Algorithm 1 Communication Topology Optimisation Algorithm

Inputs: (Current Topology $\mathcal{G}(\mathcal{V}, \mathcal{E})$), (GPS data of new DG)
Output: Calculated Topology

Initialisation:

$list \leftarrow$ Generate all regular graphs with the maximum nodal degree of d_{max}
$length \leftarrow$ Number of graphs in $list$
$A_{current} \leftarrow$ Compute the adjacency matrix of the current topology $\mathcal{G}$ (initial value = 0)
$L_{current} \leftarrow$ Compute the Laplacian matrix of the current topology $\mathcal{G}$ based on $A_{current}$
$\lambda_2^{max} \leftarrow$ Maximum algebraic connectivity of graphs in $list$ (initial value = λ_2 of first item in $list$)
$i_{\lambda_2^{max}} \leftarrow$ Index of the item with highest algebraic connectivity in $list$ (initial value = 0)
$delay_{avg}^{min} \leftarrow$ Value of average delay for the graph in the list with a minimum average delay

Loop: Finding graph with highest algebraic connectivity in list

for $i = 0$ to $length$ **do**
  $A_{new} \leftarrow$ Compute the adjacency matrix of the graph i
  $L_{new} \leftarrow$ Compute the Laplacian matrix of the graph i based on A_{new}
  $\lambda_2 \leftarrow$ Compute algebraic connectivity of the graph $list[i]$ based on L_{new}
  $delay_{avg} \leftarrow$ Find the average delay of the graph edges: $\frac{\sum_{i=1}^{N}\sum_{j=1}^{N}\tau_{ij}}{\text{number of links}}$
  if $(\lambda_2 > \lambda_2^{max})$ **then**
    if $(delay_{avg} \leq delay_{avg}^{min})$ **then**
      $\lambda_2^{max} \leftarrow \lambda_2$
      $i_{\lambda_2^{max}} \leftarrow i$
      $delay_{avg}^{min} \leftarrow delay_{avg}$
    end if
  end if
end for

Topology Adjustment:

$\mathcal{G}_{new} \leftarrow list[i_{\lambda_2^{max}}]$
return $\mathcal{G}_{new}$

access control (MAC) layer. Hence, by knowing the maximum allowed value for σ_i, no further optimisation of individual σ_i is required, because they are equal due to accessing the same medium via the same MAC layer. Thus, it is assumed that all controllers share the same $\sigma_i = \sigma_{max}$. Feasibility of event triggering condition is related to inter-event time, which is lower bounded by access rate of the communication channel. In this regard, we propose a variable, events per second E_{ps}, which depends on σ_{max}, τ_{ij}^{max} (i.e. maximum node-to-node communication delay) and p (i.e. model-related design parameter):

$$\sigma_{max} > \frac{p}{E_{ps} \times \tau_{ij}^{max}} \tag{4.28}$$

Equations (4.28) and (4.26), form a second-level optimisation problem to find the optimal value for σ_{max}. In the following section, the dynamics of the DC microgrid are modelled according to the proposed event-based control strategy.

Note that the proposed optimizer will not find the best solution that provides the fastest consensus speed among the distributed controllers. The high priority constraint in its design was response time to a topology change, which leaves only a few seconds for the computationally expensive tasks. This can be further improved by doing resource analysis on the algorithm as the microgrid size grows.

4.4 Secondary Control Layer Consensus

In this section, the mathematical model of the secondary control layer for the DC microgrid is developed. First, voltage correction terms for control objectives, voltage regulation, and SoC balancing, are introduced, along with related SoC dynamics for batteries. An average consensus protocol for bus voltage regulation is developed, followed by cooperative control for SoC balancing, where a small-signal stability analysis is described.

4.4.1 Modified Droop Control for Battery Systems

DC-DC converters operate at a high pulse width modulation (PWM) switching frequency, with at least one switching interval delay (i.e. T_s) in the current control (CC) mode. In Figure 4.2, a diagram of converter interfacing batteries to the DC microgrid is shown. As noticed, bus voltage regulation is designed as an outer-loop between the output voltage of battery v_i^{ref}, and local bus voltage v_i. The transfer function for the internal loop is given by $H_i^{v_{ol}}$.

$$H_i^{v_{cl}} = \frac{H_i^{v_{ol}}}{1 + H_i^{v_{ol}}} \ , \quad H_i^{v_{ol}} = \frac{G_i^{v}}{sC_i(T_s s + 1)} \tag{4.29}$$

Hence, the closed-loop transfer function of local bus voltage of DC microgrid is given by:

$$V = \mathbf{H^{v_{cl}}} V^{ref} \tag{4.30}$$

A first-order model is used for battery per-unit energy level charging and discharging:

$$\dot{SoC_i} = -\frac{v_i i_i}{E_i^{max}} \tag{4.31}$$

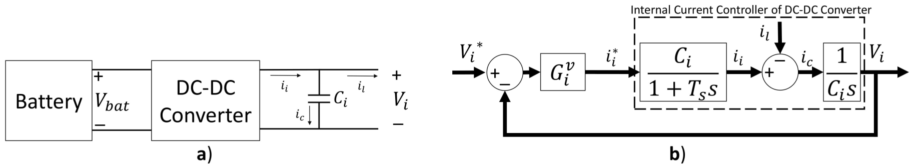

Figure 4.2: DC-DC converter model for interfacing batteries to microgrid: a) converter circuit; b) internal controller. Due to the increased computational complexity of the simulated model to run in real-time on dSPACE SCALEXIO experimental setup, using an equivalent switching model for DC-DC converter was not possible in this work.

where E_i^{max} is the battery charge capacity of the ESS, v_i is the bus voltage, and i_i is the converter current. It is assumed that converter loss is negligible.

In the secondary control layer, voltage reference (v^{ref}) for DC-DC converter is set by modified droop control with two correction terms for each bus controller for battery systems, as follows:

$$v_i^{ref} = v_{mg} - r_i^{drp} i_i + \delta v_i^v + \delta v_i^{soc} \tag{4.32}$$

where δv_i^{soc} is SoC balancing correction term, and δv_i^v is the bus voltage regulating correction term.

The average consensus protocol of each battery local bus voltage through graph $\mathcal{G}$ is:

$$\bar{v}_i = v_i + \int \sum_{j \in \mathcal{N}_i} a_{ij} \left(\bar{v}_j - \bar{v}_i\right) dt \tag{4.33}$$

where $\bar{v}_i$ is local bus voltage estimation. Thus, $\{\bar{v}_i\}$ are exchanged in the communication network between battery controllers for the local bus voltage average consensus protocol. Global dynamics of distributed average consensus protocol can be given as:

$$\dot{\overline{\mathbf{v}}} = \dot{\mathbf{v}} - \mathbf{L}\overline{\mathbf{v}} \tag{4.34}$$

which can be realised using the event-based consensus protocol defined in Theorem 1.

Applying Laplace transform yields the following transfer function matrix for the average consensus protocol [4]:

$$\mathbf{G}_{\text{avg}} = \frac{\overline{\mathbf{V}}}{\mathbf{V}} = \frac{s}{(s\mathbb{I}_N + \mathbf{L})} \tag{4.35}$$

where $\overline{\mathbf{V}}$ and $\mathbf{V}$ are the Laplace transforms of $\overline{v}$ and v, respectively.

For a balanced communication graph with a spanning tree, steady-state gain of average consensus protocol is given by averaging matrix:

$$\lim_{s \to 0} \mathbf{G}_{\text{avg}} = Q, \text{where } [Q]_{ij} = \frac{1}{N} \tag{4.36}$$

Final value theorem shows that for a vector of step inputs, elements of $\overline{\mathbf{x}}(t)$ converge to the global average of steady-state values $\mathbf{v}^{ss}$:

$$\lim_{t \to \infty} \overline{\mathbf{v}}(t) = \lim_{s \to 0} \mathbf{G}_{\text{avg}} \lim_{t \to \infty} s\mathbf{v} = Q\mathbf{V}^{ss} = \mathbf{v}^{ss} \tag{4.37}$$

To maintain the average local bus voltage of the battery at rated value v_{mg},, a conventional proportional-integral (PI) controller is utilised. Local bus voltage correction term in (4.32) is then computed as:

$$\delta v_{1i} = H_i \left(v_{mg} - \bar{v}_i \right), H_i = k_{Pi}^{\bar{v}} + \frac{k_{Ii}^{\bar{v}}}{s} \tag{4.38}$$

where H_i is PI controller, $k_{Pi}^{\bar{v}}$ and $k_{Ii}^{\bar{v}}$ are proportional and integral PI gains, respectively. This PI controller regulates the average value of local bus voltages of DC-DC converter output of the battery to rated microgrid voltage. Hence, bus voltage offset from primary droop control is compensated.

Another consensus control balances the SoC level among batteries. Data of $\{SoC_i\}$ are exchanged between neighbouring ESSs. Correction term δv_{2i}^b in (5) is defined as:

$$\delta v_{2i}^b = G_i^b \sum_{j \in \mathcal{N}_i} a_{ij} \left(SoC_j - SoC_i \right), G_i^b = k_{Pi}^{SoC} \tag{4.39}$$

where k_{Pi}^{SoC} is the control gain of SoC cooperative balancing control.

4.4.2 Small Signal Stability Analysis

Output currents of ES converters are derived from multiplying bus voltages with bus admittance matrix, constructed based on line and load impedance values:

$$I = YV \tag{4.40}$$

Total SoC level dynamics can be summarised in vector form based on (4.31):

$$E = MYV, \quad M = diag\{-\frac{v^{mg}}{E_i^{max} s}\} \tag{4.41}$$

Based on equations (4.32), (4.38), (4.39), and (4.41), the total multi-variable form of closed-loop secondary and primary control system dynamics can be described as follows:

$$\mathbf{V} = \left(\left(\mathbf{H}^{\mathbf{v_{cl}}}\right)^{-1} + \left(\mathbf{G^b LM} + \mathbf{r}_{drp}\right) Y + \mathbf{HG}_{avg} \right)^{-1} \quad (4.42)$$

$$\left(\left(\mathbf{H} + \mathbf{I_N}\right) \mathbf{v}_{mg}\right) \quad (4.43)$$

where $\mathbf{G}_{\text{avg}}$ is the transfer function of voltage average consensus protocol, $\mathbf{v}_{mg}$ is the nominal voltage, Y_{net} is the admittance matrix, and I_N is an $N \times N$ identity matrix.

$$\begin{aligned} &\mathbf{V} = [V_1, V_2, \ldots, V_p]^T, \mathbf{r}_{drp} = \text{diag}\left\{r_i^{drp}\right\} \\ &\mathbf{H} = \text{diag}\left\{H_i\right\}, \mathbf{H}^{\mathbf{v_{cl}}} = \text{diag}\left\{H_i^{v_{cl}}\right\} \\ &\mathbf{G} = \text{diag}\left\{G_i^b\right\} \end{aligned} \quad (4.44)$$

To analyse the stability of the dynamics in (4.42), it is assumed that the reference voltage is given as:

$$\mathbf{v}_{mg} = \left(\frac{v_{mg}}{s}\right) \mathbf{1}_N \quad (4.45)$$

where $\mathbf{1}_N \in \mathbb{R}^{N \times 1}$ is the vector with all the elements equal to one. Using the final value theorem of Laplace transform, steady-state values of total microgrid dynamics are derived. By defining the steady-state total bus voltage vector, $\mathbf{v}^{ss}$, the final value is:

$$\begin{aligned} \mathbf{v}^{ss} = \lim_{s \to 0} &\left(s\left(\mathbf{H}^{\mathbf{v_{cl}}}\right)^{-1} + s\left(\mathbf{G^b LM} + \mathbf{r}_{drp}\right) Y + s\mathbf{HG}_{avg} \right)^{-1} \\ &\left(\left(s\mathbf{H} + s\mathbf{I_N}\right) \mathbf{v}_{mg}\right) \end{aligned} \quad (4.46)$$

Based on the work in [46], it can be shown that:

$$The\ final\ steady\ state\ value: \ \langle \mathbf{v}^{ss} \rangle = v_{mg} \quad (4.47)$$

4.5 Experimental Results: Analysis and Discussion

A feasibility case study for DC microgrid, based on IEEE 5 Bus reference, has been appropriately selected for performance evaluation of consensus-based controller, and P&P topology switching algorithm. Values of interest for a consensus problem in the microgrid are 1) average bus voltage, and 2) average SoC level of ESSs (per-unit). The developed experimental setup is shown in Figure 4.3. It consists of dSPACE SCALEXIO real-time simulator for HIL

Table 4.1: Comparison of the proposed communication-centric control system for DC microgrids with state-of-the-art.

Control Strategy	Event-Based	Minimum Time Convergence	Robust to Time Delays	Topology Optimisation
Zhang [96]	No	Yes	Yes	No
Baranwal [97]	No	No	Yes	No
Mathew [98]	No	No	Yes	No
Trip [99]	No	Yes	No	Yes
Rahman [100]	Yes	No	No	Yes
This work	**Yes**	**Yes**	**Yes**	**Yes**

simulation of DC microgrid, dSPACE MicroLabBox for real-time simulation of communication links using TrueTime network modelling framework, and developed multi-agent embedded controllers based on Arduino boards with corresponding signal conditioning interface circuits. Controllers that support WiFi communication protocol, have also been connected to the real-time microgrid simulator, dSPACE SCALEXIO. Moreover, the proposed strategy has been developed using digital signal processing (DSP) instructions of ARM Cortex-M0+, and model-based implementation and measurements have been carried out using MATLAB/Simulink and publish/subscribe communication model, respectively.

Multiple subscribers can listen for a predetermined topic, and also multiple publishers can publish new data on certain topics. In Table 4.1, the proposed controller has also been compared with previously reported works based on: 1) event transmission, 2) convergence time, 3) robustness to time delays, and 4) topology optimisation.

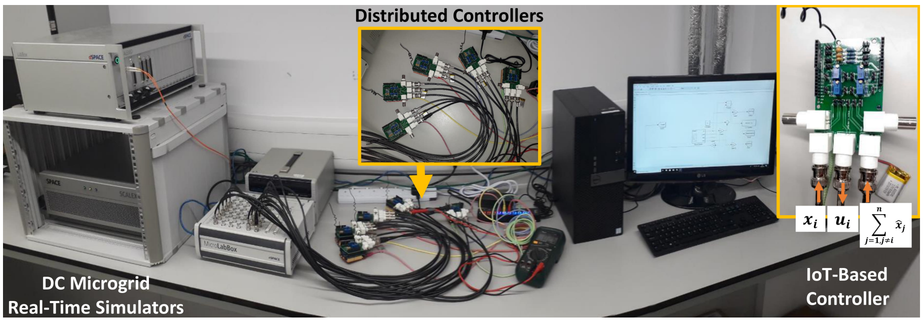

Figure 4.3: Developed testbed for experimental analysis and validation of proposed multilayer microgrid control system, consisting of real-time simulators and distributed IoT-based control units.

4.5.1 DC Microgrid Configuration

Figure 4.4 presents the DC microgrid structure employed in the deployed case study. The microgrid includes one storage on each bus. The nominal operating voltage of the microgrid is 380 V±5%, as most industrial microgrids use this nominal DC voltage, especially data centres [68]. 30 kWh (78.947 Ah) batteries are installed at all buses as ESSs of the microgrid. Constant power loads are assumed in the experiment. Thus, there is an internal controller to assure constant power is absorbed from the microgrid. Values for constant power loads are 150 W for buses 1 to 3, and 50 W for buses 4 and 5, leading to the total power consumption of 550 W. The initial energy level of storage systems is 50% of their capacity. Other parameters used in the experimental analysis, such as controller gains, are shown in Table 4.2. DG dynamics are abstracted by the corresponding ESS that buffers generated energy. With this assumption, the proposed distributed controller becomes agnostic to the size and dynamics of installed DGs on buses. As reference in the experimental setup, DGs have a nominal rating of 100 W, which supplies 500 W to the microgrid in total.

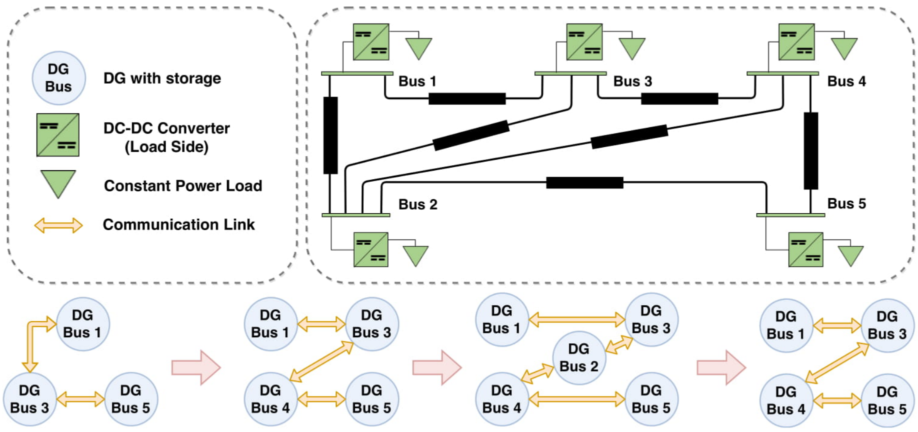

Figure 4.4: IEEE 5 bus configuration and topology optimisation results during operation of developed DC microgrid.

4.5.2 Microgrid Operation Analysis

The experiment has been conducted for 80s to show the dynamic response of the whole system in a short time frame in two scenarios. In the first scenario, Scenario A, load on all buses switches from 0% to 100% in steps of 20% every 20s. The average communication delay between distributed controllers is 100 milliseconds. In the second scenario, Scenario B, there are time-varying loads installed on buses, and the average communication delay between controllers is 200 milliseconds. Communication graph also switches from graph according to Figure 4.4 every 20s. Communication delay between agents is a random Gaussian process.

Figure 4.5 shows bus voltages are stabilised with less than 2% deviation, and consensus controllers are further converged in each step, along with the average consensus value shown in Figure 4.6. It can be seen that voltage is stabilised around nominal 380 V of microgrid, and destabilising effect of addition or removal of DGs is mitigated. A balanced per-unit energy level is also achieved, as shown in Figure 4.7 and Figure 4.8 in each step. When DG is in a disconnected state, consensus voltage is reset to the nominal voltage of the microgrid. However, after DG addition into the microgrid, the corresponding controller cooperatively works with other controllers to reach the average value of consensus voltage. Figure 4.9 shows injected power of ESSs on each bus in Watts, which supplies power in the DC microgrid. Results confirm that consensus is achieved during the operation of distributed controllers with event-based delayed communication.

Table 4.2: Parameters of microgrid case study and controller.

R_{dc}	10 Ω	k_{Pi}^{SoC}	5000	$k_{Pi}^{\bar{v}}$	500
L_{dc}	7 μH	r	0.2533	$k_{Ii}^{\bar{v}}$	10
σ_i	0.5	e_{max}	30 kWh	Load$_{total}$	550 W

Table 4.3: Communication delay between controllers for both scenarios.

Communication Link	Scenarios A	Scenario B
Bus 1 - Bus 3	50ms	100ms
Bus 2 - Bus 3	150ms	250ms
Bus 2 - Bus 4	80ms	180ms
Bus 3 - Bus 4	120ms	220ms
Bus 3 - Bus 5	60ms	160ms
Bus 4 - Bus 5	140ms	240ms

4.6 Summary

This chapter introduced a multilayer cooperative event-based control for DC microgrids, which is resilient to communication delays, and further supports P&P addition or removal of DGs. It has been shown that convergence time is reduced using the bi-level optimisation approach. Average consensus is achieved among distributed controllers using the developed event-based protocol, considering

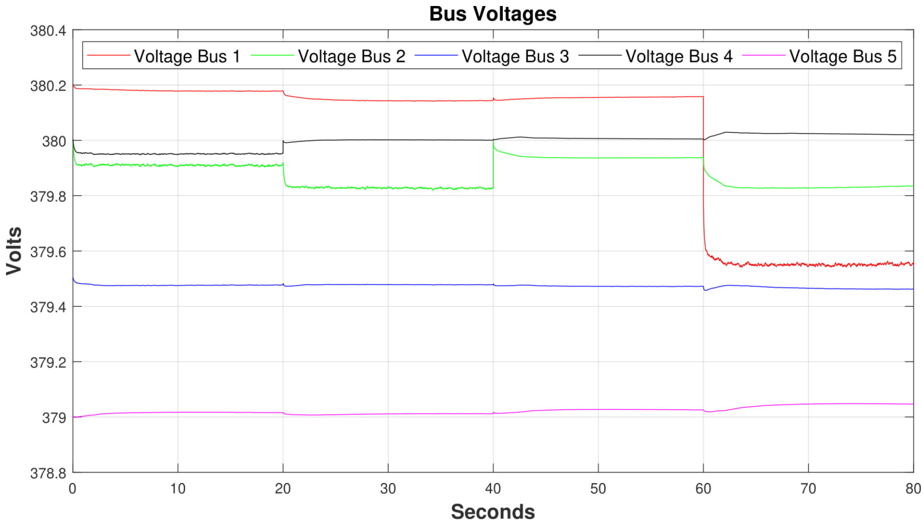

Figure 4.5: Scenario A, step by step incremental loads with 100ms average time delay: Voltage profiles of buses during the experiment. Voltage is stabilised around nominal 380 V of microgrid and destabilising effect of DGs addition or removal is mitigated.

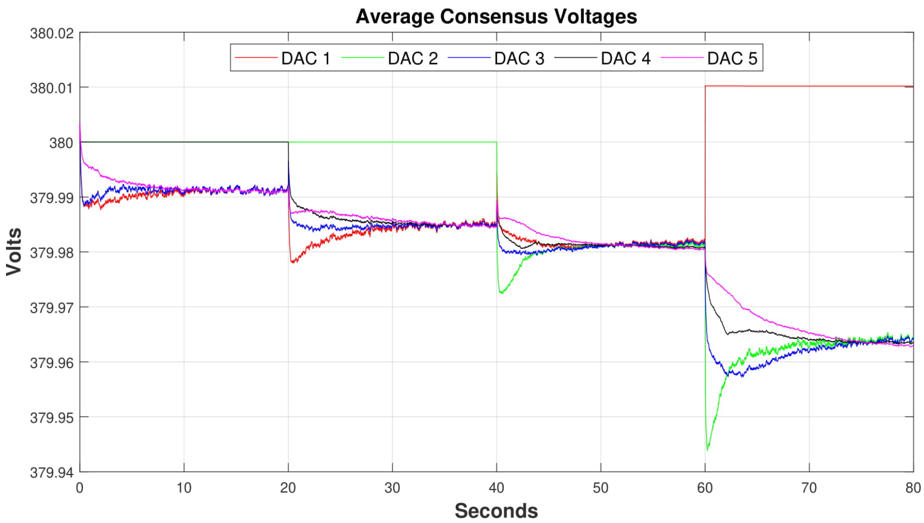

Figure 4.6: Scenario A, step by step incremental loads with 100ms average time delay: Consensus voltage profile of DG controllers during the experiment. When DG is in the disconnected state, consensus voltage is reset to the nominal voltage of the microgrid, however, after DG is added into the microgrid, the corresponding ESS controller cooperatively works with other controllers to reach an average voltage consensus value.

non-uniform delays. Moreover, a practical case study using the HIL simulation testbed has validated the performance of the proposed controller for voltage stabilisation, as well as balanced power-sharing in DC microgrids. Besides, the

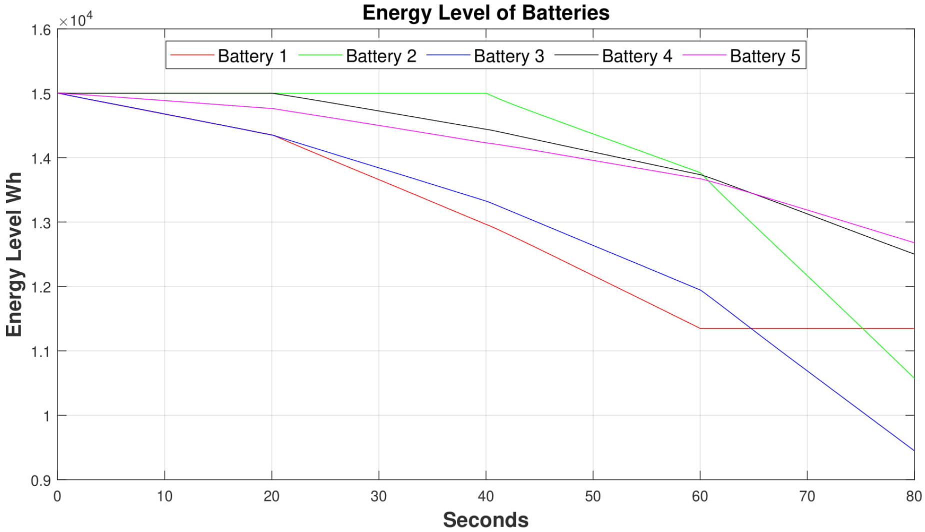

Figure 4.7: Scenario A, step by step incremental loads with 100ms average time delay: Energy level profile of storage systems during the experiment. All DGs include battery storage to compensate for the DGs supply deficit in the microgrid. When DG is in a disconnection state, its corresponding storage stops charging/discharging, however, after DG is added into the microgrid, the corresponding ESS controller cooperatively uses storage for demand response.

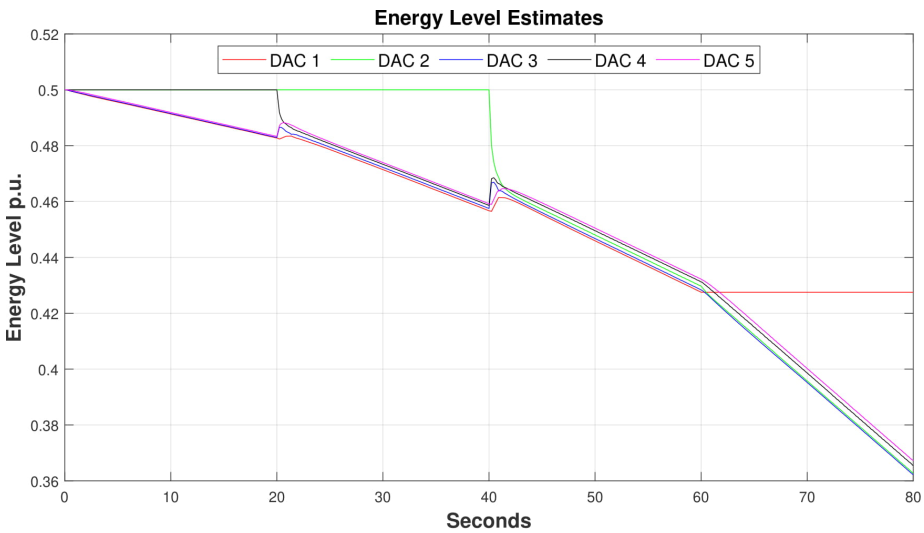

Figure 4.8: Scenario A, step by step incremental loads with 100ms average time delay: Energy level per-unit consensus profile during the experiment. Values are provided in a per-unit format for better comparison, which is proportional to the capacity of energy storage systems.

feasibility of beamforming technology and its potential for future integration in IoT-centric aspects of microgrids have been discussed.

Experimental results confirmed that microgrid could be stabilised although

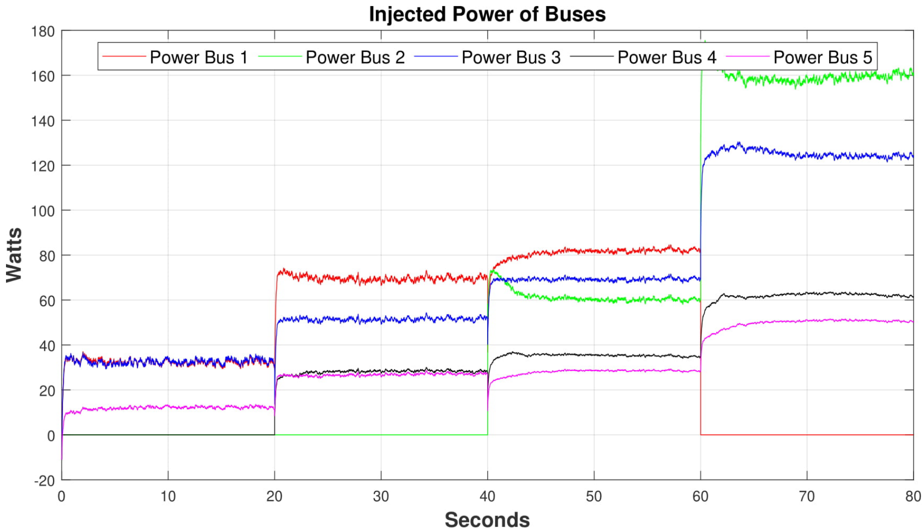

Figure 4.9: Scenario A, step by step incremental loads with 100ms average time delay: Injected power profile of buses during the experiment. When DG is in the disconnected state, it provides zero energy supply, however, after DG is added into the microgrid, the corresponding ESS controller cooperatively adjusts power based on the average consensus value of voltage and per-unit energy level of its corresponding storage.

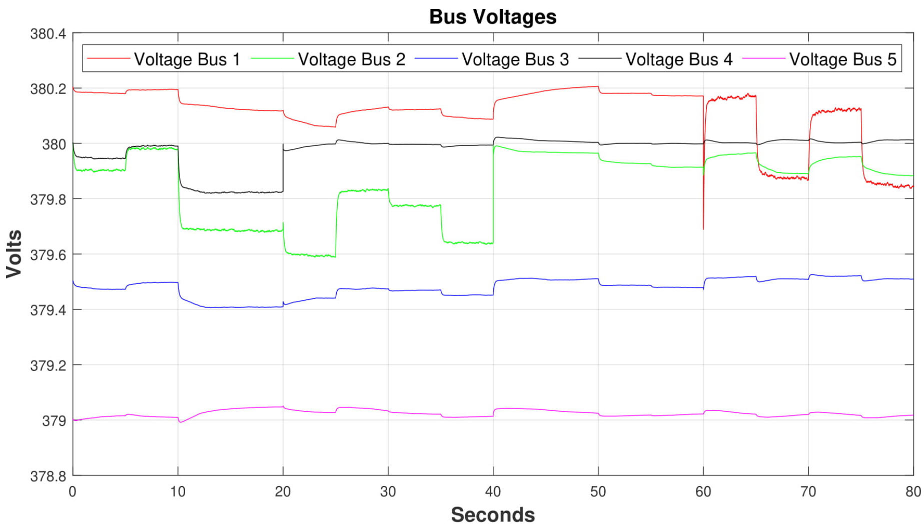

Figure 4.10: Scenario B, time-varying loads with 200ms average time delay: Voltage profiles of buses during the experiment. Voltage is stabilised around nominal 380 V of microgrid and destabilising effect of DGs addition or removal is mitigated.

communication network has large delays and data are transmitted in an event-based approach. Moreover, the proposed topology assignment algorithm was able to maintain connectivity of distributed controllers in event of addition or removal of DGs from the microgrid. This is very important as it forms the basis

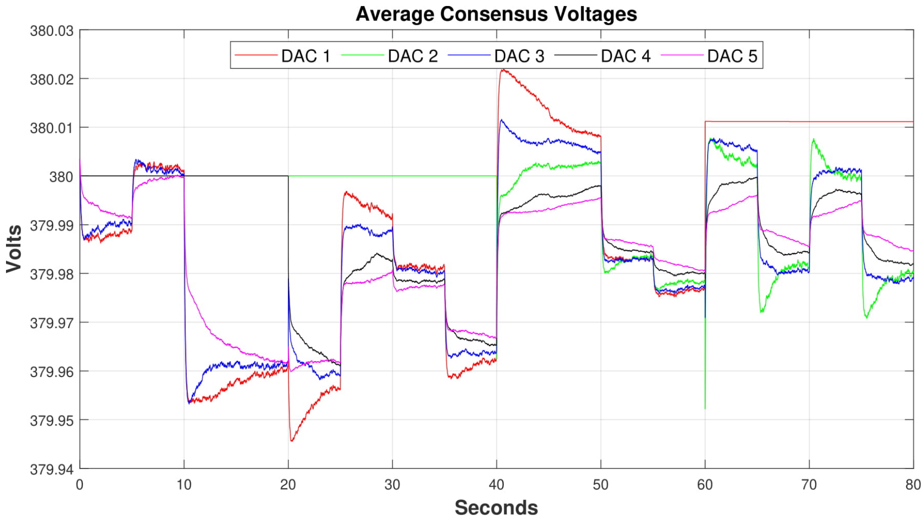

Figure 4.11: Scenario B, time-varying loads with 200ms average time delay: Consensus voltage profile of DG controllers during the experiment. When DG is in the disconnected state, consensus voltage is reset to the nominal voltage of the microgrid, however, after DG is added into the microgrid, the corresponding ESS controller cooperatively works with other controllers to reach an average voltage consensus value.

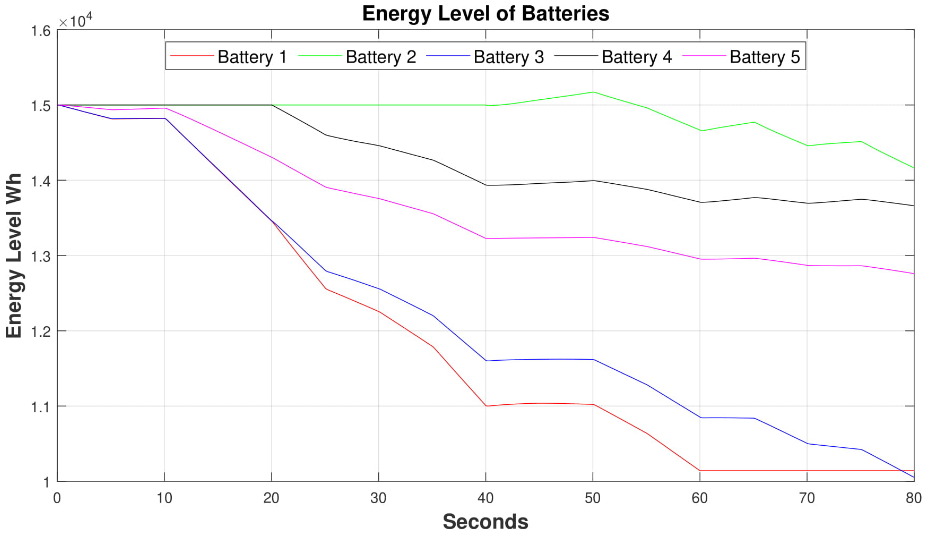

Figure 4.12: Scenario B, time-varying loads with 200ms average time delay: Energy level profile of storage systems during the experiment. All DGs include battery storage to compensate for the DGs supply deficit in the microgrid. When DG is in a disconnection state, its corresponding storage stops charging/discharging, however, after DG is added into the microgrid, the corresponding ESS controller cooperatively uses storage for demand response.

for the P&P operation of microgrid due to the intermittent nature of RES.

For the future extension of this work, artificial intelligence (AI)-driven con-

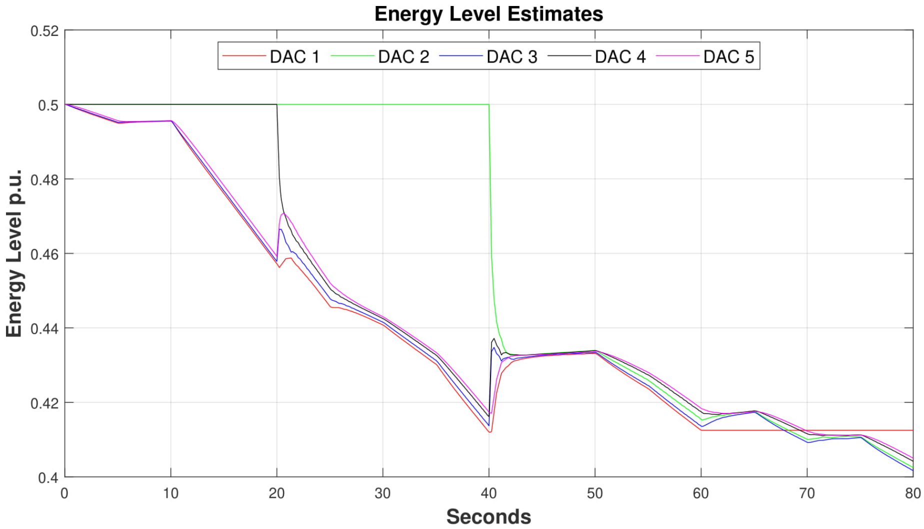

Figure 4.13: Scenario B, time-varying loads with 200ms average time delay: Energy level per-unit consensus profile during the experiment. Values are provided in a per-unit format for better comparison, which is proportional to the capacity of energy storage systems.

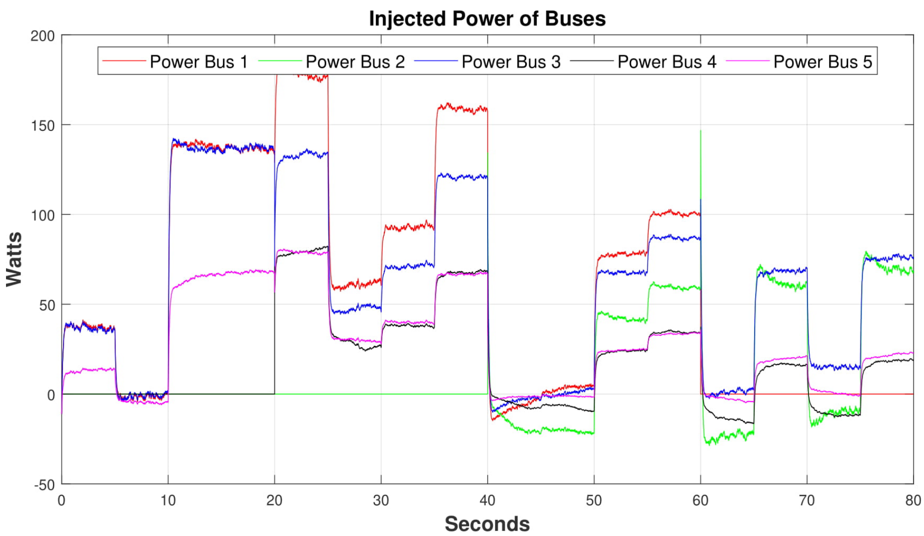

Figure 4.14: Scenario B, time-varying loads with 200ms average time delay: Injected power profile of buses during the experiment. When DG is in the disconnected state, it provides zero energy supply, however, after DG is added into the microgrid, the corresponding ESS controller cooperatively adjusts power based on the average consensus value of voltage and per-unit energy level of its corresponding storage.

trol systems can be employed to improve the efficiency of the proposed bi-level topology assignment framework, along with its coordination with the real-time secondary control model. Graph optimisation problems can also be solved using machine learning methods. Furthermore, it is recommended to use a switching model for a bi-directional DC-DC converter, which provides more realistic results compared to the simplified average model.

Chapter 5

Observer Design with Adaptive Send-on-Delta Sampling

State estimation is one of the main challenges in the microgrids, due to the complexity of the system dynamics and the limitations of the communication network. In this regard, a novel real-time event-based optimal state estimator is proposed in this chapter, which uses a novel adaptive send-on-delta (SoD) non-uniform sampling method over wireless sensors networks. The proposed estimator requires low communication bandwidth and incurs lower computational resource cost. The threshold for the SoD sampler is made adaptive based on the average communication link delay, which is computed in a distributed form using the event-based average consensus protocol. The SoD non-uniform signal sampling approach reduces the traffic over the wireless communication network due to the events transmitted only when there is a level crossing in the measurements. The state estimator structure is extended on top of the traditional Kalman filter with the additional stages for the fusion of the received events. The error correction stage is further improved by optimal reconstruction of the signals using projection onto convex sets (POCS) algorithm. Finally, an Internet of things (IoT) experimental platform based on LoRaWAN and IEEE 802.11 (WiFi) protocols is developed to analyse the performance of the state estimator for the IEEE 5 Bus case study microgrid. The results of this chapter formed the basis for publishing [5].

The contributions of this chapter can be summarized as the proposal of the following:

- An optimal event-based state estimation framework for microgrids that consists of the proposed event-triggered Kalman filter with the POCS-based signal reconstruction.

- An adaptive threshold SoD sampling method to mitigate the communication delay for accurate state estimation.
- An event-based average consensus protocol for average delay consensus of sampling units such as smart meters.

This chapter is organized as follows. In Section 5.1, data modelling for both AC and DC microgrids and the architecture of the estimator are discussed. An overview of observer design process is provided in Section 5.2. Then after, the event-based Kalman filter is developed in Section 5.3 and the POCS signal reconstruction technique is discussed in Section 5.4. The time delay consensus protocol for adaptive threshold SoD sampling is provided in Section 5.5. The optimality of the solution is analysed from different aspects in Section 5.6. In Section 5.7, the results for validation of the observer performance are provided, which is evaluated on a experimental DC microgrid test-bench. The model used for the closed loop control system is derived from our previous work in [4], in which we have proposed a distributed control system for DC microgrids. Finally, the chapter is summarized in Section 5.8.

5.1 Data modelling and architecture of state estimator

In this section, the microgrid state estimation problem is modelled from the measurement data viewpoint. A microgrid usually consists of energy storage (ES) systems, renewable energy sources (RESs), consumer loads and power converters. Generally, two voltage systems are considered for microgrids: DC (Direct Current) and AC (Alternating Current) microgrids. Each of these different types are dynamic systems that can be modelled using a set of (non)linear differential equations. Like any other type of dynamical system, every process has internal state variables, outputs, and inputs. The measurements set for DC microgrids state estimation are {voltage of buses, injected current into each bus}, respectively:

$$\begin{aligned} v_i \in V, &\ \text{voltage of buses} \\ i_i \in I, &\ \text{injected current into each bus} \end{aligned}$$

Other variables such as phase can be considered for AC microgrids as well, but the phasor measurement units (PMUs) are required for this high speed synchronization, which can be expensive. Therefore, indirect measurements with active and reactive power are used here, which have higher feasibility with lower cost. It is assumed that the measurements from the distributed sensors have the following error dynamics:

$$\mathbf{z} = \mathbf{h}(x) + \begin{bmatrix}\mathbf{e_1 e_2} \ldots \mathbf{e_n}\end{bmatrix}^\top \tag{5.1}$$

where $\mathbf{z}$ is the output of the sensors, $\mathbf{h}(x)$ is the state to output mapping, and $\mathbf{e_i}$ is the sensor error, which can be due to the noise, or inaccuracy. Also the state dynamics are modelled with the nodal admittance matrix (Y bus) of the grid.

The architecture of the proposed state estimator with event-based measurements is shown in Figure 5.1. The three parts are: the event-based adaptive Kalman state estimator, the event-based signal reconstructor and the mean square error (MSE) comparator. The microgrid estimation input quantities are collected using the proposed adaptive send-on-delta (SoD) measurement technique. The event-based Kalman filter works based on the knowledge that the signal between the events is bounded by the δ threshold in the SoD sampler. The original signal is reconstructed in the signal conditioner based on the received events using the projection onto convex sets (POCS) algorithm, which is mainly used in the literature as a promising approach for low quality image reconstruction. In the last stage, the error comparator updates the estimated state input based on the difference of the reconstructed signal and the predicted output of the previous filtering stage. The SoD sampler threshold is adapted distributively based on the consensus value of the average communication delay. In this mechanism, each sensor calculates the round trip delay between itself the and the microgrid estimator, and adjusts the threshold according to the fused data from neighbor sensors. The main advantage of this mechanism shows itself when the microgrid components communicate over a shared wireless medium, which is usually the case in IoT-enabled microgrids [46]. Optimal usage of network resources, meanwhile providing a high quality estimate of the microgrid state is the aim of the proposed estimation strategy. For example, consider that a microgrid is operating in a transient mode. Usually, in transient modes, the system exposes fast dynamics that lead to a very large number of events using the delay-independent SoD sampling method, which was tackled in our previous work [57]. Communication delay directly proportional to the traffic rate (or packet generation rate) in a shared medium. As a result, the delay on the shared communication medium increases, which considerably de-

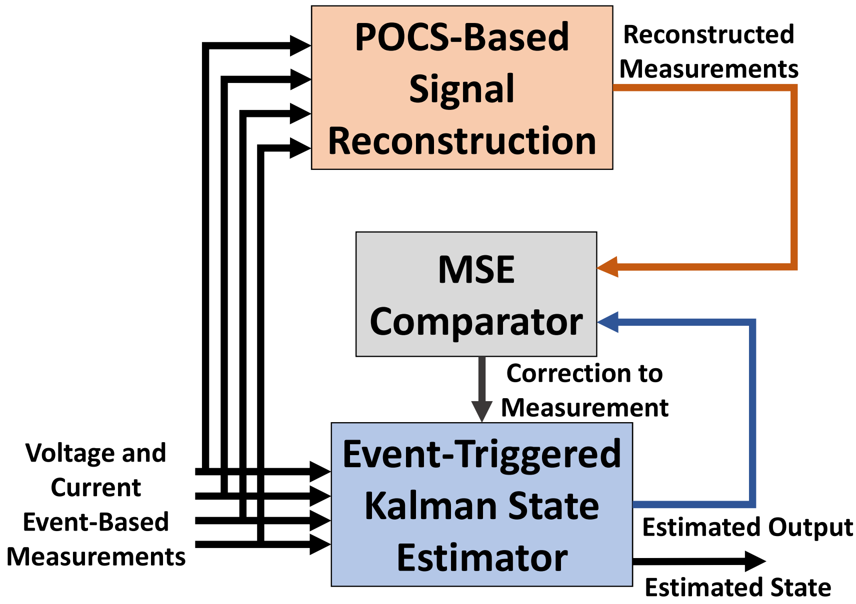

Figure 5.1: Proposed event-based structure for microgrid state estimation.

creases the quality of data and the state estimation accuracy. However, in our proposal, if the sensors achieve a consensus on the average communication delay on the shared communication medium, they can automatically adjust the SoD sampling threshold to a wider region, which leads to a lower number of events generated. As a result of this adaptivity, the quality of the data and the state estimation accuracy will be improved considerably, comparing to the previous proposed delay-independent method. To provide this average delay consensus for the sensors in a microgrid, a novel event-based average consensus protocol is proposed in Section 5.5, which works in parallel with the SoD sampling data flow.

5.2 Observer design process

This section summarizes the steps required for the microgrid state estimator, in a simplified sequence:

1. Finding the global small signal model of the microgrid in the form of a linear state space equation. In this step, the covariance for the process noise and the measurement noise should be chosen according to the microgrid specifications and sensor accuracies. In this work, we have converted the closed loop transfer function matrix, defined in equation (36) of [4], into

minimal state space model to get equation (5.2).

2. Choosing the initial value for the threshold of the SoD sampler. This value should be selected in accordance with the covariance values chosen in the previous steps, in order to prevent the noisy measurements generate unnecessary events and the resulted traffic.

3. Building the communication topology graph for the event-based average consensus protocol defined in Theorem 1. The graph should be strongly connected, but doesn't need to be deterministic, as the average consensus protocol, designed in the next step, adjusts the SoD threshold dynamically.

4. Choosing the average consensus parameters to have a guaranteed convergence rate for the consensus protocol. This value affects the event generation, therefore a trade-off takes place between the number of events and the convergence rate of the protocol.

After these steps are taken in the design process, the parameters of the state estimator and the nodes are initialized with the corresponding microgrid parameters. In the results section, the values for the parameters of the case study microgrid are provided together with the results of the experiment. In the next section, the mathematical framework of the event-based Kalman filter with SoD sampling is developed.

5.3 Event-based Kalman filter based on send-on-delta

Minimal realization of the microgrid admittance bus (Y bus) and the small signal model of the controllers, results in the following multi-variable system for the estimation problem:

$$\begin{aligned} ll\dot{x} &= Ax\left(t\right) + w\left(t\right) \\ y(t) &= Cx(t) + v(t) \end{aligned} \tag{5.2}$$

where $x \in \mathrm{R}^{\mathrm{n}}$ is the system state and $y \in \mathrm{R}^{\mathrm{p}}$ is the measured output. $w\left(t\right)$ and $v(t)$ are the process noise and measurement noise, respectively, which are the uncorrelated, zero-mean white Gaussian random processes, satisfying the following:

$$\mathrm{E}\left\{w(t);w(s)'\right\} = Q;\delta(t-s) \tag{5.3}$$
$$\mathrm{E}\left\{v(t);v(s)'\right\} = R;\delta(t-s) \tag{5.4}$$
$$\tag{5.5}$$

R is the measurement noise covariance, and Q is the process noise covariance. Also, w_i and v_j are the i-th and j-th elements of the w and v, respectively. It is presumed that the i-th sensor only transmits the data when the difference between the current value and the previous value is greater than the SoD threshold δ_i. Using SoD method [39], the estimator continuously samples the data with a period of T from the measurement nodes. For example, if the last received i-th sensor value is y_i at time $t_{last,i}$, and there is no data received from i-th node for $t > t_{last,i}$, then $y_i(t)$ is estimated as:

$$y_i\left(t_{last,i}\right) - \delta_i \leq \; y_i\left(t\right) \leq y_i\left(t_{last,i}\right) + \delta_i \tag{5.6}$$

The last received i-th sensor data is used to compute the output $y_{computed,i}$ even if there is no sensor data transmission:

$$y_{computed,i}\left(t\right) = y_i\left(t_{last,i}\right) = C_i x\left(t\right) + v_i\left(t\right) + \Delta_i\left(t, t_{last,i}\right) \tag{5.7}$$

where $\Delta_i\left(t, t_{last,i}\right) = y_i\left(t_{last,i}\right) - y_i\left(t\right)$ and:

$$\left|\Delta_i\left(t, t_{last,i}\right)\right| \leq \delta_i \tag{5.8}$$

In (5.7), measurement deviation increases from $v_i\left(t\right)$ to $v_i\left(t\right) + \Delta_i\left(t, t_{last,i}\right)$. $\Delta_i\left(t, t_{last,i}\right)$ is assumed to have the uniform distribution constrained by (5.8), therefore, the variance of $\Delta_i\left(t, t_{last,i}\right)$ is $\frac{(2\times\delta)_i^2}{12}$, which will be added to the *output noise covariance matrix*, $\mathrm{R}(i,i)$, in the Kalman estimator.

SoD-based State Estimation Algorithm: In order to suitably improve the *update* part of the standard Kalman filter algorithm, an improved algorithm is proposed here, which makes it adapted to the SoD event triggering condition by increasing the input covariance $\overline{R}_k$, at the instant of the events:

1. **Initialization step**

$$\hat{x}^{-}(0), P_0^{-}$$
$$y_{last} = C\hat{x}^{-}\left(0\right) \tag{5.9}$$

2. **Input measurement update**

$$\overline{R}_k = R \tag{5.10}$$

if *i*-th event are received

$$\hat{y}_{last,i} = y_i\,(kT) \tag{5.11}$$

else

$$\overline{R}_k\,(i,i) = \overline{R}_k\,(i,i) + \frac{(2\times\delta)_i^2}{12} \tag{5.12}$$

end if

$$\begin{aligned} K_k &= P_k^- C'(CP_k^- C' + \overline{R}_k)^{-1} \\ \hat{x}\,(kT) &= \hat{x}^-\,(kT) + K_k(\hat{y}_{last} - C\hat{x}^-(kT)) \\ P_k &= (I - K_kC)P_k^- \end{aligned} \tag{5.13}$$

3. **Project ahead**

$$\begin{aligned} \hat{x}^-\,((k+1)T) &= \exp{(AT)}\hat{x}\,(kT) \\ P_{k+1}^- &= \exp{(AT)}P_k\exp{(A'T)} + Q_d \end{aligned} \tag{5.14}$$

where Q_d is the covariance of the process noise for the discretized microgrid state space realization, and y_{last} is defined as follows (5.15):

$$y_{last} = [y_{last,1}, y_{last,2}, \ldots, y_{last,p}]' \tag{5.15}$$

The presented event-based estimator is also able to be used in the implementation of the distributed controllers in networked systems. For further studies on the convergence analysis, one may refer to [46]. It should be noted that in the proposed event-based observer, convergence is achieved by knowing the fact that Kalman filer is an optimal observer. Nevertheless, choosing smaller values for δ_i would result in the a significant decrease in convergence time [39].

5.4 Optimized reconstruction of sampled signals

The SoD sampled version of a signal contains the time instants that the original signal has changed more than the threshold in the SoD sampling (i.e. δ). If no sample has been generated by the SoD sampler, then it means that the original signal has remained in the region around the last event value with the radius of δ. Here, this is called the implicit information in the event data, which is used to solve the optimization problem of signal fitting and reconstruction. To formulate the optimization problem, the solution boundaries need to be determined. The implicit information from the SoD sampled signals are used to determine the required boundaries for the solution of the convex optimization problem, which is modelled in the following. To model and solve the optimization problem, projection onto convex sets (POCS) technique is used, which has been previously used for image reconstruction from low resolution cameras [101, 102] and for signal recovery from level crossing samples [103]. SoD sampling is a generalization of level crossing or Lebesgue sampling, which also considers the signal initial value. To adjust this sampling technique to POCS formulation, the results of level-crossing sampling from [104] are extended, detailed in the next Section.

5.4.1 Implicit information of send-on-delta sampled signal

Send-on-Delta sampling is a type of event-based sampling, where each event shows a crossing of the signal $x(t)$ from a one dimensional region bounded by δ around the last sample. The event time instants $t_n \in \mathbb{Z}, n \in \mathbb{Z}$ are defined as:

$$t_n = \min\{t > t_{n-1}, x(t) - x(t_{n-1}) > \delta\} \tag{5.16}$$

The output of SoD sampler is the sequence of pairs $(t_n, x(t_n))$. The set of possible samples by assuming zero initial conditions is $X_e = \{x(t_0), x(t_1), x(t_2), \ldots, x(t_n)\}$. In order to formulate the convex optimization problem, a convex region for the possible range of the reconstructed signal is defined according to (5.16):

$$\theta^-(t) \leq x(t) < \theta^+(t) \tag{5.17}$$

where $\theta^-(t)$ and $\theta^+(t)$ are the piece-wise constant lower and upper boundaries respectively, that are created from the following constraints:

$$\begin{aligned} \theta^-(t) &= \{r \in \mathbb{R}, r = x(k) - \delta, k \in t_n\} \\ \theta^+(t) &= \{r \in \mathbb{R}, r = x(k) + \delta, k \in t_n\} \end{aligned} \tag{5.18}$$

With this definition, the sign of the signal slope at the event instants (t_n) is defined as:

$$S(t_n) = \begin{cases} x(t_n) - x(t_{n-1}), & x(t_n) \neq x(t_{n-1}) \\ S(t_{n-1}), & x(t_n) = x(t_{n-1}) \end{cases} \tag{5.19}$$

The samples along with the implicit boundary information, take a form of sets membership. Therefore, the solution for the reconstructed signal $x(t)$ will fall into the following convex sets ($C(\mathbb{R})$ and $\mathbb{L}^2$ denote continuous function and Hilbert space, respectively):

1. From the explicit information (signal values at the time of events):

$$\xi = \{u(t) \in C(\mathbb{R}) : u(t_n) = x(t_n) \text{ for all } n \in \mathbb{Z}\} \tag{5.20}$$

2. From the implicit information (the value of the threshold that generated this event):

$$\mathbb{I} = \{u(t) \in C(\mathbb{R}) : \theta^- \leq u(t) < \theta^+(t) \text{ for all } t \in \mathbb{R}\} \tag{5.21}$$

3. From the knowledge that the signal is band-limited with maximum frequency Ω (Fourier decomposition of the highest order dynamics in the signals of the system):

$$\mathbb{B} = \left\{ u(t) \in \mathbb{L}^2(\mathbb{R}) : \forall |\omega| > \Omega, \int_{-\infty}^{+\infty} u(t) e^{-j\omega t} dt = 0 \right\} \tag{5.22}$$

The set $\mathbb{B}$ is convex as the band-limited signals form a linear space. For the sets $\mathbb{I}$ and ξ, [104] provides the proof of convexity. The reconstructed signal should be a member of the set $\xi \cap \mathbb{I} \cap \mathbb{B}$ as the constraint of the optimization. This constraint is usually a large region that makes finding the optimal solution a computation intensive task. Fortunately, because $\theta^-(t) \leq x(t) < \theta^+(t)$, one can easily derive that $\mathbb{I} \subset \xi$. Therefore, the constraint is limited to the boundary defined by $\mathbb{I} \cap \mathbb{B}$, which needs less computations for the task of real-time signal estimation.

5.4.2 Projection onto convex sets signal reconstruction

There are two methods to solve the formulated POCS problem in the literature, one-step and iterative projection. A detailed comparison of these two methods is provided in [104]. As real-time state estimation for microgrids is the aim of this chapter, the later method of iterative projection onto convex sets is used, which exhibits fast computations with low precision loss. Iterative solution for POCS works by having two or more convex sets, and on each iteration the initial solution is projected to one of those convex solutions sets. By repeating the projection iteratively to those sets, the initial estimate gets closer to the optimal solution.

The projection of the signal g onto a continuous convex set C results in another signal $\hat{x}(t)$, which is nearest to signal g:

$$\hat{x} = P_{C}g = \arg\min_{y \in C} ||g - y|| \tag{5.23}$$

where the projection $P_{C}g$ is closer to any $y \in C$ than g:

$$||P_{C}g - x|| < ||g - y|| \tag{5.24}$$

For the event-based signal reconstruction problem, the initial guess $\hat{x}_0$ should be first projected onto convex set $\mathbb{B}$ with the following projection operator:

$$\begin{aligned} P_{\mathbb{B}}g(t) &= \hat{x}(t) * \frac{\Omega}{\pi}\mathrm{sinc}(\Omega t) \\ &= \int_{-\infty}^{\infty} \hat{x}(\tau)\frac{\Omega}{\pi}\mathrm{sinc}(\Omega(t-\tau))d\tau \end{aligned} \tag{5.25}$$

having defined $sinc(y) = \frac{sin(y)}{y}$. ($*$ is the convolution)

The projection operator onto convex set $\mathbb{I}$ for clipping the signal to the boundary defined by θ is:

$$P_{\mathbb{I}}g(t) = \begin{cases} \theta^+(t), & \hat{x}(t) > \theta^+(t) \\ \hat{x}(t), & \theta^-(t) \leq \hat{x}(t) < \theta^+(t) \\ \theta^-(t), & \hat{x}(t) < \theta^-(t) \end{cases} \tag{5.26}$$

Finally, by applying this operator for both projections, the desired accuracy of signal reconstruction will be achieved:

$$\hat{x}_{m+1} = P_{\mathbb{B}}gP_{\mathbb{I}}g\hat{x}_m, \quad m \in \mathbb{Z} \tag{5.27}$$

The condition for stopping the projections depends on the required accuracy measures and is application dependant. By practical experiments, authors have found that 10 iterations provides an acceptable accuracy for the microgrid experiment duration, which is used in the experiment.

5.4.3 Mean-square error comparator update rule

Normally, the measurements from the nodes arrive with the added noise signal. The noise is assumed to be the derivative of the Brownian motion, which is called white noise or Gaussian noise. The traditional Kalman filter is build on top of this assumption that the noise is Gaussian, however, by using the SoD sampling technique, the reconstructed signal becomes a non-Gaussian stochastic process. This leads to degradation of the estimation accuracy and longer convergence time, if it converges. Therefore, an estimator update rule is proposed here that compares the output of the Kalman filter and the reconstructed signal in real-time, and injects the correction value to the input of the Kalman filter, respectively. The correction is a dynamic offset value, which is added as described in the following:

$$y_i\left(t_{last,i}\right) = \begin{cases} y_i(kT), & \|y_{i_{predict}} - y_{i_{construct}} < \delta\| \\ \\ y_{i_{construct}}(kT), & \|y_{i_{predict}} - y_{i_{construct}} \geq \delta\| \end{cases} \tag{5.28}$$

where $y_{i_{predict}}$ and $y_{i_{construct}}$ are the output of the signal reconstructor and the event-based Kalman filter, respectively.

5.5 Adaptive SoD threshold consensus with event-based communication

Each measurement unit, calculates the estimator communication link delay using acknowledgment round-trip delay (RTD) [105]. This value is then shared with neighbor units using the proposed event-based communication protocol. Each unit then decides the value of its SoD sampler threshold based on the average communication delay, using a linear droop mapping. In other words, when the average delay increases, the threshold for SoD sampling is also increased in order to reduce the network traffic. The droop rate can be different for the units, which provides the potential to prioritize the sampling of each unit, however for simplicity of the results comparison, a shared practical droop value is assumed in this chapter. The value of the droop is tuned based on the IoT network setup of the microgrid. In the following section, the event-based average delay consensus protocol is described.

The measurement unit are connected by an undirected graph $\mathcal{G}(\mathcal{V}, \mathcal{E})$ with the nodes or vertices $\mathcal{V} = (1, ..., \mathcal{N})$, and the set of edges $\mathcal{E} \subset \mathcal{V} \times \mathcal{V}$. The nodes in the graph represent the measurement units, and the edges denoting the communication link between the nodes. The condition $(i, j) \in \mathcal{E}$ holds if there is a link allowing the information flow from node i to node j and vice versa. $A = [a_{ij}] \in R^{N \times N}$, represents the graph adjacency matrix, where $a_{ij} > 0$ if $(i, j) \in \mathcal{E}$, and $a_{ij} = 0$ otherwise. $d_i = \sum_{j=1}^{N} a_{ij}$ denotes the weighted degree of agent v_i. The degree matrix of the graph is given by $\mathbf{D} = diag\{d_i\}$, and the

Laplacian matrix of the graph is derived from $\mathbf{L} = \mathbf{D} - \mathbf{A}$. An undirected graph is connected, if there exists at least one path between any two agents.

5.5.1 Average consensus protocol

By considering a multi-agent network with N single integrator agents, the distributed average consensus will be:

$$\dot{x}_i = u_i(t) = -\sum_{j=1}^{N} L_{ij} x_j(t) \tag{5.29}$$

Since it is often not practical to have a continuous stream of data over a communication link, it is considered that each agent broadcasts its state information at specific instances (i.e. event instances) to its neighbors. Hence, we propose the following event-triggered consensus protocol:

$$\dot{x}_i = u_i(t) = -\sum_{j=1}^{N} L_{ij} \hat{x}_j(t) \tag{5.30}$$

The increasing sequence $\{t_l^i\}_{l=1}^{\infty}$ and $\{t_{l+1}^i - t_l^i\}_{l=1}^{\infty}$, are called the triggering times and inter-event times of agent i, respectively. In order to simplify the notations, let $x(t) = [x_1(t), \ldots, x_n(t)]^T$, $\hat{x}(t) = [\hat{x}_1(t), \ldots, \hat{x}_n(t)]^T$, and $e(t) = [e_1(t), \ldots, e_n(t)]^T = \hat{x}(t) - x(t)$. The aim is to find the correct event-triggering condition to prove the stability of the proposed consensus protocol. We state the following theorem, knowing the fact that λ_2 is the second smallest eigenvalue of L, using Lemma 1.

Lemma 3. *[87] The Laplacian matrix L of a connected graph $\mathbb{G}$ is positive semi-definite,i.e. $z^T L z \geq 0, \forall z \in \mathbb{R}^n$. Moreover, $z^T L z = 0$ if and only if $z = a\mathbf{1}_n, a \in \mathbb{R}$, and $0 \leq \lambda_2(L) K_n \leq L$, where λ_2 is the second smallest eigenvalue of L and $K_n = I_n - \frac{1}{n} 1_n 1_n^T$.*

Theorem 4. *Consider a strongly connected multi-agent directional graph with N agents and the consensus protocol defined in (5.30). Let $0 < \sigma_i < 1$ be a constant design parameter. Given the first triggering time $t_1^i = 0$, the network exponentially achieves average consensus under the event-triggering function given as follows:*

$$e_i^2(t) - \frac{\sigma_i}{4L_{ii}} \sum_{j=1}^{N} L_{ij} (\hat{x}_j(t) - \hat{x}_i(t))^2 \leq 0 \tag{5.31}$$

with the convergence rate, upper bounded by:

$$\exp\left(-\frac{(1-\sigma_{max})min_i\{L_{ii}\}\lambda_2(L)t}{2min_i\{L_{ii}\}+||L||\sigma_{max}}\right) \tag{5.32}$$

Proof. Following the notation of [89], $\delta(t)$ is defined as the disagreement vector with the following change of variable:

$$x(t) = a\mathbf{1} + \delta(t) \tag{5.33}$$

where a is average of the initial state values, $a = \frac{1}{N}\sum x_i(t)$. Using (5.33), the control input of the agents will be derived as:

$$\begin{aligned}\dot{\delta}(t) &= -\sum_{i=1}^{N} L_{ij}(a + \hat{\delta}_j(t))\\ &= -a\sum_{i=1}^{N} L_{ij} - \sum_{i=1}^{N} L_{ij}\hat{\delta}_j(t))\\ &= -\sum_{i=1}^{N} L_{ij}\hat{\delta}_j(t))\end{aligned} \tag{5.34}$$

Now to prove the stability, we propose the following Lyapunov function, which covers the dynamics of consensus:

$$V(\delta(t)) = \frac{1}{2}\sum_{i=1}^{N}\delta_i^2 \geq 0 \tag{5.35}$$

The derivative of the Lyapunov function along the dynamic trajectory (5.30) will be:

$$
\begin{aligned}
\dot{V}(\delta(t)) &= \sum_{i=1}^{N} \delta_i \dot{\delta}_i = \sum_{i=1}^{N} \delta_i \sum_{j=1}^{N} -L_{ij}\hat{\delta}_j(t) \\
&= \sum_{i=1}^{N} (\hat{\delta}_i - e_i(t)) \sum_{i=1}^{N} -L_{ij}\hat{\delta}_j(t) \\
&= \frac{1}{2} \sum_{i=1}^{N} \sum_{j=1}^{N} L_{ij}(\hat{\delta}_j(t) - \hat{\delta}_i(t))^2 \\
&\quad - \sum_{i=1}^{N} \sum_{j=1}^{N} e_i(t) L_{ij} \hat{\delta}_j(t) \\
&= \frac{1}{2} \sum_{i=1}^{N} \sum_{i=1}^{N} L_{ij}(\hat{\delta}_j(t) - \hat{\delta}_i(t))^2 \\
&\quad - \sum_{i=1}^{N} \sum_{j=1, j\neq i}^{N} e_i(t) L_{ij}(\hat{\delta}_j(t) - \hat{\delta}_i(t))
\end{aligned} \tag{5.36}
$$

To simplify equation (5.36), let:

$$
\hat{f}_i = -\sum_{i=1}^{N} L_{ij}(\hat{\delta}_j(t - \tau_{ij}) - \hat{\delta}_i(t))^2 \tag{5.37}
$$

Therefore, equation (5.36) becomes:

$$
\dot{V}(\delta(t)) = \frac{1}{2} \sum_{i=1}^{N} \hat{f}_i - \sum_{i=1}^{N} \sum_{j=1, j\neq i}^{N} e_i(t) L_{ij} \hat{\delta}_j(t) \tag{5.38}
$$

Since $ab < a^2 + \frac{1}{4}b^2, \forall a, b \in \mathbb{R}$, and

$$
\sum_{i=1}^{N} \hat{f}_i = -\sum_{i=1}^{N} \sum_{j=1}^{N} L_{ij}(\hat{\delta}_j(t - \tau_{ij}) - \hat{\delta}_i(t))^2 = \hat{\delta}^T(t) L \hat{\delta}(t) \tag{5.39}
$$

the following inequality holds:

$$
\begin{aligned}
\dot{V}(\delta(t)) &\leq -\frac{1}{2} \sum_{i=1}^{N} \hat{f}_i - \sum_{i=1}^{N} \sum_{j=1, j\neq i}^{N} L_{ij} e_i^2(t) \\
&\quad - \sum_{i=1}^{N} \sum_{j=1, j\neq i}^{N} L_{ij} \frac{1}{4} (\hat{\delta}_j(t - \tau_{ij}) - \hat{\delta}_i(t))^2 \\
&= -\frac{1}{4} \sum_{i=1}^{N} \hat{f}_i + \sum_{i=1}^{N} L_{ij} e_i^2(t)
\end{aligned} \tag{5.40}
$$

From (5.31) and (5.40), we have:

$$\dot{V}(\delta(t)) \le -\frac{1}{4}\sum_{i=1}^{N}\hat{f}_i + \sum_{i=1}^{N} L_{ij}e_i^2(t)$$
$$\le -\frac{1}{2}(1-\sigma_{max})\hat{\delta}^T(t)L\hat{\delta}(t) \tag{5.41}$$

where $\sigma_{max} = \max\{\sigma_1, \ldots, \sigma_n\}$. In addition, we have:

$$\delta^T(t)L\delta(t) = (\hat{\delta}(t)+e(t))^T L(\hat{\delta}(t)+e(t))$$
$$\le 2\hat{\delta}^T(t)L\hat{\delta} + 2e^T(t)Le(t) \tag{5.42}$$
$$\le 2\hat{\delta}^T(t)L\hat{\delta} + \frac{||L||\sigma_{max}}{2\min_i\{L_{ii}\}}\sum_{i=1}^{N}\hat{f}_i \tag{5.43}$$
$$= \left(2 + \frac{||L||\sigma_{max}}{2\min_i\{L_{ii}\}}\right)\hat{\delta}^T(t)L\hat{\delta} \tag{5.44}$$

where (5.42) holds because L is a positive semi-definite matrix and $2a^TLb \le a^TLa+b^TLb, \forall a,b \in \mathbb{R}^n$ and (5.43) holds since (5.31) and $a^TLa \le ||L||\,||a||^2, \forall a \in \mathbb{R}^n$. Finally we have:

$$\dot{V}(\delta(t)) \le -\frac{(1-\sigma_{max})\min_i\{L_{ii}\}}{4\min_i\{L_{ii}\}+2||L||\sigma_{max}}\delta^T(t)L\delta(t)$$
$$\le -\frac{(1-\sigma_{max})\min_i\{L_{ii}\}\lambda_2(L)}{2\min_i\{L_{ii}\}+1||L||\sigma_{max}}V(\delta(t)) \tag{5.45}$$

(5.45) holds due to Lemma 1, hence:

$$\dot{V}(\delta(t)) \le V(\delta(0))\exp\left(-\frac{(1-\sigma_{max})\min_i\{L_{ii}\}\lambda_2(L)t}{2\min_i\{L_{ii}\}+||L||\sigma_{max}}\right). \tag{5.46}$$

This shows that the multi-agent system (5.30) with event-triggering condition (5.31) exponentially reaches stability, as long as $\mathcal{G}$ is connected. □

5.6 Analysis of the observer optimality

The optimality of the proposed solution can be analysed from several aspects. From the state estimation aspect, the employed Kalman state estimator is known to be an optimal linear state estimator in the literature of state estimation. It follows from theory that the Kalman filter is the optimal linear filter in cases where:

- The model perfectly matches the real system
- The measurement noise is white (uncorrelated)

- The covariances of the noise are exactly known

When a Kalman filter works optimally, the update sequence (the output prediction error) is white noise, therefore, the whiteness property of the updates defines the estimation performance. The existence, optimality and stability of the Kalman filter with partial observations are discussed in [106].

The proposed POCS signal re-constructor is a recursive method that converges to a convex set consisting of the original signal after several iterations. The reconstructed signal found by the POCS method, is an optimal solution that can be build from the SoD generated samples. The convergence to the solution is proved in [107] along with the analysis on the convergence rate. From the communication and channel utilization aspect, the solution is optimal compared to the traditional time-based sampling technique such as zero-order-hold (ZOH). In the proposed solution, the network packet is only generated when there is a deviation from the SoD threshold or the average consensus protocol requires a new data-sharing event.

5.7 Experimental results and discussion

In order to evaluate the state estimator performance, an IoT-based setup is designed that consists of IoT smart meters based on Seeeduino® Dragon IoT evaluation boards and a DC microgrid real-time simulator from dSPACE® (SCALEXIO Real-Time Simulator). Each node has a long range wide area network (LoRaWAN) communication module and supports IEEE 802.11 b/g/n (WiFi) communication protocol. The nodes are interfaced to the real-time microgrid simulator via an interface stackable shield that can be measure analog input and output signals. The setup is shown in Figure 5.2. The proposed SoD sampling strategy is implemented using digital signal processing instructions of ARM Cortex M0+, and the microgrid model is implemented by using MATLAB/Simulink real-time code generator. WiFi protocol necessitates a router gateway to be used for the data collection. In this setup, a Raspberry Pi computer with the supporting communication modules for the gateway operation is used. This gateway receives the data from the measurement nodes via MQTT (Message Queuing Telemetry Transport) protocol. Thingsboard® software implements the MQTT broker, which is used for data archiving and processing. By using the mentioned protocols and devices, the microgrid monitoring cost can be considerably cheaper than other smart metering technologies such as IEC 61850 [108]. The state estimator was implemented on the real-time microgrid simulator. The nodes measure the signals and transmit them over the wireless network to the real-time simulator. Therefore, all of the results are observed at the real-time simulator. The IEEE 5 bus reference microgrid with the nominal 110 V bus voltage and 10kW reference power for per-unit calculations, as shown in Figure 5.3, is chosen for the case study. The droop controllers are designed based on the technique proposed in [4]. The Y bus admittance matrix for state representation of the microgird is derived based on the line parameters in Table 5.1. Also the covariance parameters and initial SoD threshold of the estimator is shown in Table 5.2. The IEEE 5 bus microgrid system is standardized with a set of reference line parameters which includes the resistance, reactance, and the susceptance of the lines based on 50 Hz AC frequency. In a DC microgrid, the values of resistance, inductance, and capacitance are the important line dynamics required to be modelled in the simulation. Therefore, we have converted the corresponding values in the AC system to their equivalent DC system with the following simple formula in per-unit: $R_{dc} = R_{ac}$ (not considering the corona effect), $L_{dc} = \frac{X_L}{2*\pi*f}$, and $C_{dc} = \frac{2*\pi*f}{X_C}$

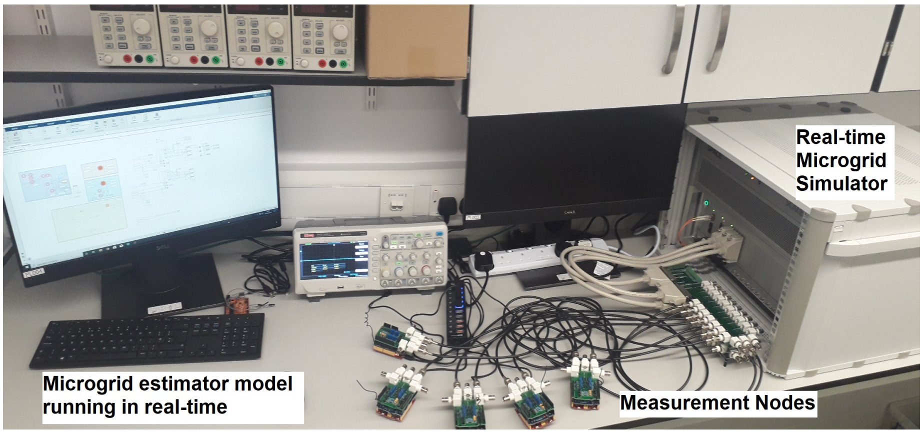

Figure 5.2: Experimental setup for evaluation of the proposed estimator.

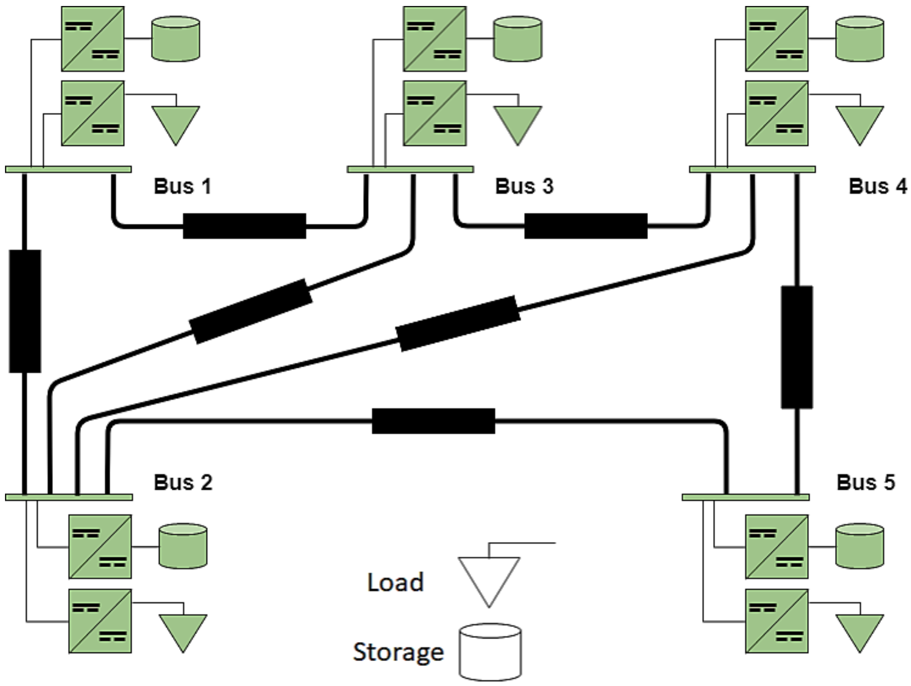

Figure 5.3: IEEE 5 bus case study for estimator validation.

Table 5.1: Line parameters of the IEEE 5 bus microgrid .

Line	Line Impedance (p.u.)	Line Susceptance (p.u)
1-2	$0.02 + j0.06$	$j0.03$
1-3	$0.08 + j0.24$	$j0.025$
2-3	$0.06 + j0.25$	$j0.02$
2-4	$0.06 + j0.18$	$j0.02$
2-5	$0.04 + j0.12$	$j0.015$
3-4	$0.01 + j0.03$	$j0.01$
4-5	$0.08 + j0.24$	$j0.025$

The simulations is run for 5 seconds, and the estimator converges to the actual state in 600 milliseconds, as shown in Figure 5.4. Furthermore, Figure 5.5 shows that the proposed estimation strategy has achieved a better performance comparing to the traditional Kalman filter by converging to lower steady state error. For this simulation, the traditional Kalman filter runs in a digital platform with 0.1 millisecond period, needs 10,000 events in 1 second to achieve the same performance as our proposed estimation strategy, with only a few hundred events. The Kalman filter has always been challenged for its high speed measurement requirements, however the proposed estimator has opened new doors for event-based state estimators with low communication speed requirements. The event generation density over the time is shown in Figure 5.6. Also as shown in Figure 5.8, the steady state estimation error is comparatively lower comparing to the classic Kalman filter. The comparison of the observer methods are provided in Table 5.3. From the network traffic perspective, Figure 5.9 illustrates the comparison of the proposed adaptive SoD sampler estimator with the static threshold state estimator. The accumulative number of packets transmitted in the network, is reduced more than 40% from the static threshold SoD sampling method. This further depicts that the energy consumption in battery based sensors drops more that 40% as the processing burden and network load is considerably reduced. Also, the existence of the threshold, guarantees that the Zeno behaviour will never happen, as can be seen in Figure 5.6. During the experimental, it was found that the LoRaWAN communication protocol has significant limitations, which can decrease the accuracy of estimation. It introduces a large value of delay between the events transmission in the range of seconds, especially when the number of messages per unit of time gets higher than the capacity of the network. The threshold of the SoD sampler directly affects the amount of messages, therefore, a tuning algorithm will be required in order to make a relation between the estimation error, sampling threshold, and the number of events. Nevertheless, by using a high speed WiFi communication network, the ideal performance was achieved, fulfilling the data collection strategy requirements.

Table 5.2: State estimator parameters for simulation.

$\delta(0)$ (threshold initial value)	1
Q (Process Noise Covariance)	0.1
R (Measurement Noise Covariance)	0.36
T (Estimator Sampling Time)	100 microseconds
σ_{max} (Even generation parameter)	0.6

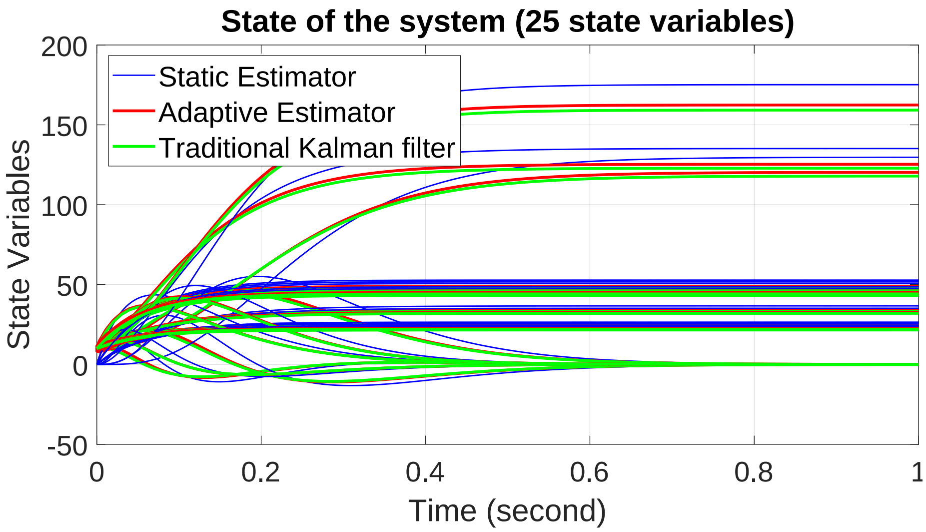

Figure 5.4: Experiment result 1: State variables of the microgrid. The microgrid is realized into 25 state variables that need to be estimated by the proposed observer.

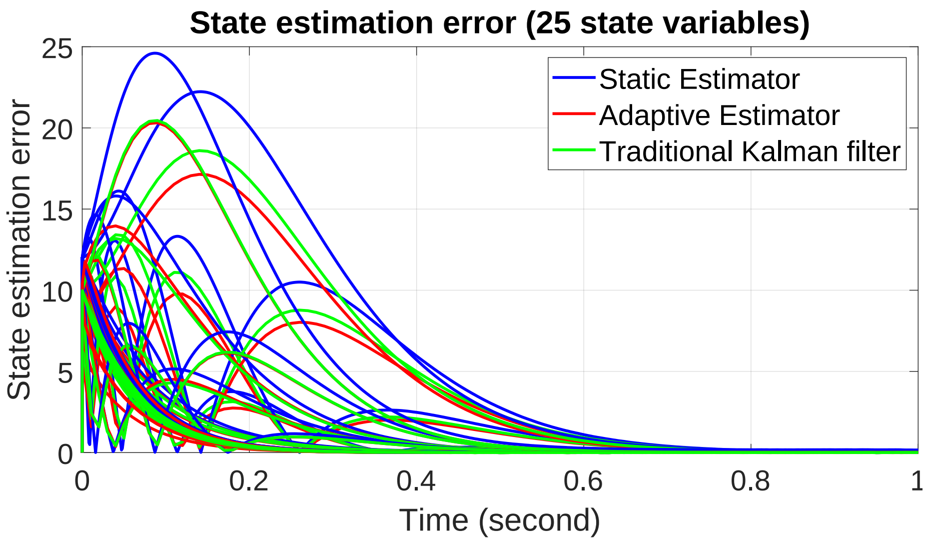

Figure 5.5: Experiment result 2: The estimation error of the observers for comparison. The static estimator has a constant threshold with the value "1", and the adaptive estimator is initialized with the same value.

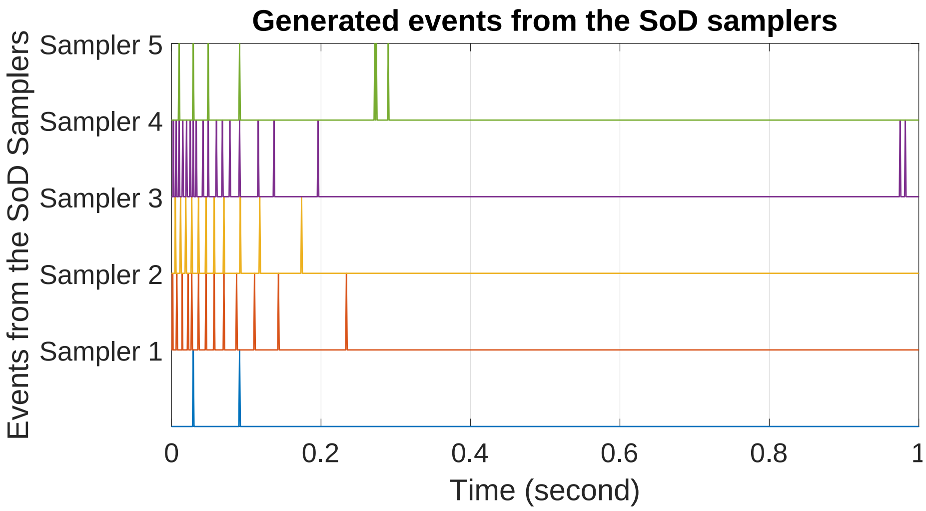

Figure 5.6: Experiment result 3: Event generation density from the adaptive SoD sampler nodes. As can be seen, the number of generated events gets decreased as the system enters into its steady state mode.

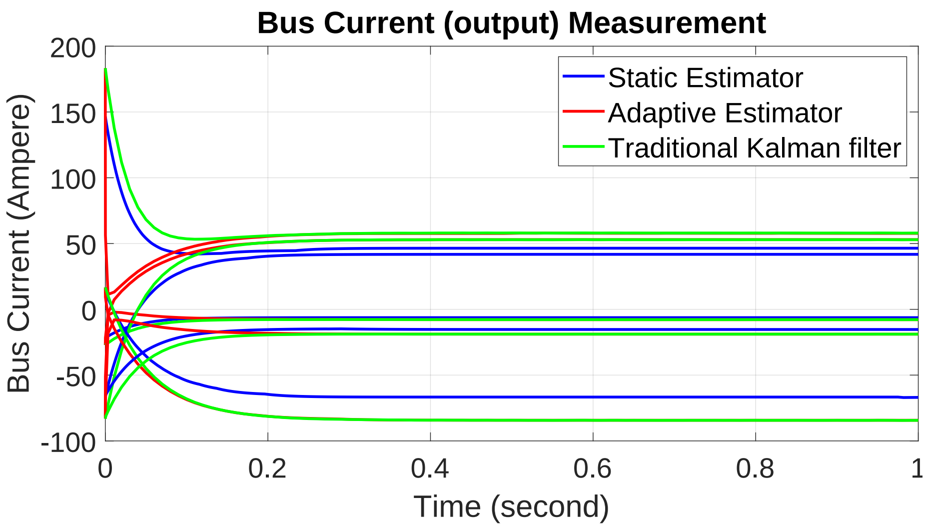

Figure 5.7: Experiment result 4: The injected currents of the buses (system outputs). The nominal voltage is 110 V. Negative current means power generation and positive current means consumption at the buses.

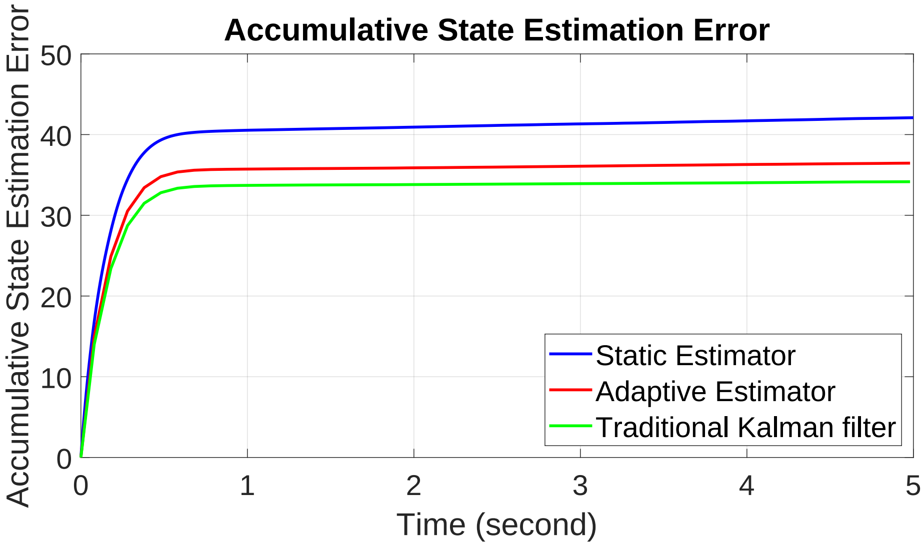

Figure 5.8: Experiment result 5: Accumulative estimation error comparison between the traditional Kalman filter, the proposed adaptive threshold state estimator, and the static state estimator.

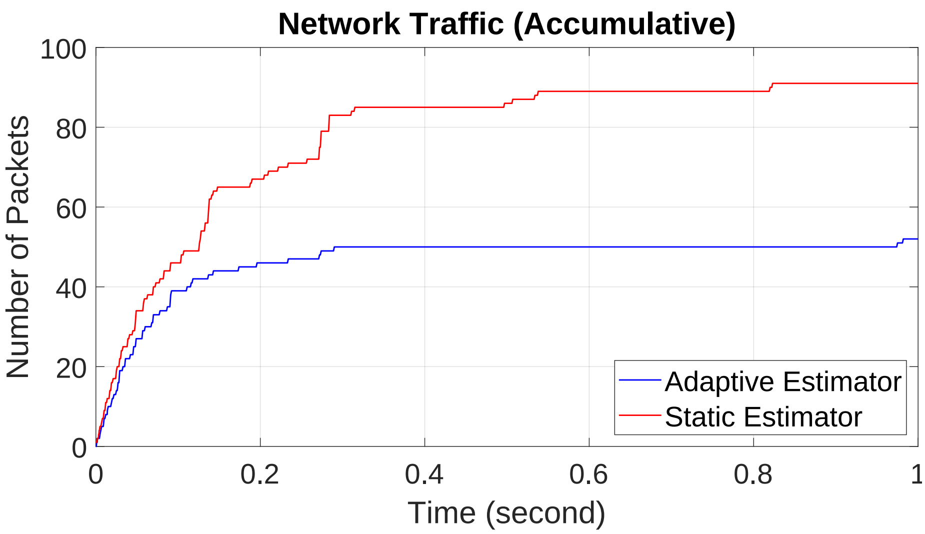

Figure 5.9: Experiment result 6: Network traffic comparison between the static SoD sampler and the proposed adaptive strategy. It can be seen that the overall traffic is reduced by more than 40%.

5.8 Summary

In this chapter, an event-based optimal observer is proposed for the microgrids. The proposed estimator works based on send-on-delta (SoD) non-uniform sam-

Table 5.3: Comparison of the observers by their required network characteristics.

Observer	Sampling Type	Delay	Resource Usage	Operation Type	Accuracy
Traditional (Classic) Kalman Filter [106]	Periodic	Not considered	High	Centralized	High
Static Threshold SoD-Based Kalman Filter [57]	Event-based	Not considered	Low	Centralized	Medium
Proposed Adaptive Observer with POCS Conditioner	Event-based	Adaptive	Medium	Distributed	High

pling method and furthermore, the SoD threshold is adaptive with regard to the average communication delay. The average delay is decided using the event-based average consensus protocol. The estimation error is further corrected by projection onto convex sets algorithm to have a higher estimation accuracy. It was resulted that the estimator has low estimation error comparing to the classic Kalman filter, with only a few events exchanged in the communication network. The optimality of the solution is analysed along with a step by step design procedure. The performance of the observer is studied in the reference IEEE 5 Bus microgrid. For the future study, the results can be extended to consider the packet drop out in the observer performance.

Chapter 6

Prioritized Control of Energy Storage Systems Based on Short-Term Demand-Side Forecasting

In a microgrid, renewable energy sources (RES) exhibit stochastic behaviour, which affects the microgrid continuous operation. Normally, energy storage systems (ESSs) are installed on the main branches of the microgrids to compensate for the load-supply mismatch. However, their state of charge (SoC) level needs to be balanced to guarantee the continuous operation of the microgrid in case of RES unavailability. This chapter introduces a distributed forecast-based consensus control strategy for DC microgrids that balances the SoC levels of ESSs. By using the load-supply forecast of each branch, the microgrid operational continuity is increased while the voltage is stabilized. These objectives are achieved by prioritized (dis)charging of ESSs based on the RES availability and load forecast. Each branch controller integrates a load forecasting unit based on long short-term memory (LSTM) deep neural network that adaptively adjusts the (dis)charging rate of the ESSs to increase the microgrid endurability in the event of temporary generation insufficiencies. Furthermore, due to the large training data requirements of the LSTM models, distributed extended Kalman filter algorithm is used to improve the learning convergence time. The performance of the proposed strategy is evaluated on an experimental 380V DC microgrid hardware-in-the-loop test-bench and the results confirm the achievement of the controller objectives. The results of this chapter formed the basis for publishing [6].

The proposed control strategy has three components: 1) primary layer virtual resistance droop control, 2) secondary layer distributed consensus control for voltage offset correction, and SoC balancing of ESSs, 3) short-term load forecast LSTM distributed learning adapter for predictive (dis)charging of ESSs.

The main contributions of this chapter can be summarized as the proposal of the following items:

- A distributed consensus control system that stabilizes the bus voltages co-designed to balance the SoC levels of ESSs in a DC microgrid;
- Prioritized (dis)charging controller for ESSs based on short-term energy forecast of the branches to achieve higher endurability for the DC microgrid;
- Integration of the load forecasting unit in the secondary control layer of the microgrid based on LSTM neural network with DEKF learning algorithm;

The rest of this chapter is organized as follows. Section 6.1 reviews the state of art in energy forecasting methods and shows the advantage of LSTM models for this purpose. Section 6.2 introduces the components of DC microgrids. The proposed control strategy is discussed in Section 6.3 in detail. Section 6.4 provides information about the proposed load forecast adaptation method and the prioritized (dis)charging logic. The training of the distributed LSTM forecasting models is then described in Section 6.5. The experimental results for the case study microgrid are demonstrated in Section 6.6. Finally, the chapter is summarized in Section 6.7.

6.1 Energy forecasting methods in different horizons

Different factors affect the forecasting performance thus making such prediction a sophisticated process. Among these factors, the forecasting horizon is the most important decision parameter, which is the future time duration for output forecasting [115]. The main types of forecasting horizons introduced in the literature can be categorized as [116]: very short-term, short-term, medium-term, and long-term.

Very short-term forecasting

Very short-term forecasting is used in power system and smart grid planning with the prediction period from seconds to several hours min [117].

Table 6.1: Comparison of the energy forecasting methods in terms of computational complexity, data requirements, optimizer operation, and the evaluated forecast horizon.

Forecasting Method	Computational Complexity	Data Requirements	Optimizer Operation	Evaluated Forecast Horizon
Exponential Smoothing [109]	Very Low	Equally Spaced Samples	Centralized	hourly
ARMA [110]	Low	Equally Spaced Samples	Centralized	monthly
ARIMA [111, 112]	Low	Equally Spaced Samples	Centralized	hourly
MLPNN [113]	Medium	High Resolution, Noise Free	Centralized	monthly
RNN [69]	High	High Resolution, Noise Free	Centralized	daily
RBFNN [114]	Very High	High Resolution	Distributed	monthly
LSTM [72]	High	High Resolution	Distributed	weekly

Short-term forecasting

This is the most common horizon chosen in the electricity market, where decisions comprise of economic load dispatch and power system operation. It is also useful in the control of renewable energy integrated power management systems, therefore, in this chapter, short-term load forecasting is selected for the ESS SoC balancing problem. Generally, the temporal horizon is between several hours to seven days [115].

Medium-term forecasting

Medium-term forecasting spans up to a month ahead as being in this category. It is essential for maintenance scheduling of conventional or solar energy integrated power systems consisting of high-end transformers and different types of electromechanical machinery [115].

Long term forecasting

Long-term forecasts predict scenarios for a month to a year [115]. Such a prediction horizon is suitable for long term power generation, transmission, distribution and solar energy rationing [118], as well as seasonal trends prediction.

6.1.1 Energy forecasting methods

The collection of energy data over time results in time series. These time series are stochastic by their nature, therefore, deterministic model-based methods such as model predictive control (MPC) lack the suitable performance required. Time series provides statistical information to foresee the nature of the quantified element. These observations are generally recorded overtime at successive points in regular intervals [119]. The main established time series prediction techniques are [116, 120]: exponential smoothing, autoregressive moving average (ARMA) and autoregressive integrated moving average (ARIMA), RNN, radial basis function neural network (RBFNN), and LSTM neural network.

Exponential smoothing

The exponential smoothing method or exponentially weighted moving average (EWMA) is a technique that adopts exponential window function for statistical analysis of historical time series data to make predictions. The technique was first formulated by Brown [119] and has since seen many applications. Generally, it allocates an unequal set of weights over equal weights to historical observations, thereby exponentially reducing the data from the most recent to the most distant data points.

Autoregressive moving average model (ARMA)

ARMA is a time series statistical analysis frequently used in forecasting. The model has been evaluated by many researchers in different applications of forecasting (solar and wind forecasting) and it has consistently performed with good prediction accuracy. The model incorporates two polynomials: AR and MA for forecasting from historical data [110].

Autoregressive integrated moving average (ARIMA)

ARIMA is also known as the Box-Jenkins model and was developed by George Box and Gwilym Jenkins in 1976 [112]. ARIMA model is an extended version of ARMA and it is a popular time series analysis technique as it supports a standard level of forecast accuracy for short term horizon. Moreover, this model can clip non-stationary values from the analyzed data. Its structure consists of autoregression (AR), integration (I), and moving average (MA) to evaluate and predict time series characteristics [111].

Multi-layer perceptron neural network (MLPNN))

Many researchers treat the MLPNN model as a benchmark [113]. It is a technique for elementary and effective artificial neural network (ANN) approach to designing and prediction. It is so powerful that this network is used in universal approximation, nonlinear modeling, and complex problems that cannot be solved by an ordinary single-layer neural network [113]. Generally, MLP is a composite of three or more layers of incoherently activating nodes. Therefore, it can correlate the input and output relationship through learning.

Recurrent neural network (RNN)

RNN is a class of ANN that can learn and process different relationships as well as computational structures. This network provisionally relies on time series data by the feedback system to inherit the previous time step values; demonstrating temporal dynamic characteristics. The model has a simple structure with a built-in feedback loop, which allows it to act as a forecasting engine. RNN output of the concerned neural layer is summed with the next input vector and fed back into the same layer which is the only layer in the entire network. The applications are versatile ranging from speech recognition to driverless cars.

Radial basis function neural network (RBFNN)

RBFNN is a quicker and better approach to machine learning than other ANN approaches. Hence, it is used in approximation, time series prediction, classification, and system control [114]. The structure uses radial basis functions as activation functions. This network generally has two layers. The characteristics are merged with the radial basis activation function in the first layer, and then the output of the first layer is used to compute the same output in the next time step.

Long short-term memory(LSTM) neural network

The LSTM neural network is a type of RNN. As mentioned, RNNs use previous time events to inform the later ones. RNNs work well if the problem requires only recent information to perform the present task. If the problem requires long term dependencies, RNN doesn't provide the required performance. The LSTM was designed to learn long term dependencies. It remembers the information for long periods. LSTM was introduced by S Hochreiter, J Schmidhuber in 1997 [70].

Due to the following advantages of LSTM deep learning model, it was chosen in this work to solve the forecasting problem:

- LSTM models are proven to have superior performance when there are long term dependencies in the forecasted times series.
- As LSTM models are deep neural networks, the feature analysis is automatically done through the learning process, therefore, it has an easier application and less error-prone.
- LSTM neural networks support distributed training using the DEKF training algorithm. Therefore, it enables its integration with distributed control tasks that work over the neighbor communication system.

The comparison of different forecasting methods is summarized in Table 6.1.

We have chosen the short-term forecasting horizon due to the following reasons:

- The secondary and tertiary control systems for microgrids are usually operating at a high speed, therefore, the energy forecasting horizon can not be very long, otherwise, the adaptiveness of the control parameters to the transient in energy supply and demand would be lost. Therefore, from the control system performance viewpoint, either short-term and very short-term forecasting horizons should be considered.
- The (dis)charging cycles of energy storage systems in a microgrid take place with a time duration of several hours to several days. This is because their capacity is often large and for maintenance and storage health reasons, their (dis)charging currents are limited to increase the lifetime of the energy storage systems.
- The renewable energy sources such as wind turbines and PV panels are intermittent sources dependant on the weather condition, temperate and other environmental parameters. Most of these environmental parameters exhibit dynamics in several hours to a few days. Therefore, it is required to prioritise the (dis)charging of the energy storage systems based on the forecasts for the same time duration.

6.2 Radial DC microgrid components and configuration

The schematic of a solar DC microgrid is shown in Figure 6.1, which consists of battery ESSs, PV panels, and loads. PV panels are connected to the main bus through a voltage controllable boost converter, working in maximum power point tracking (MPPT) mode. The DC loads are connected to the bus through

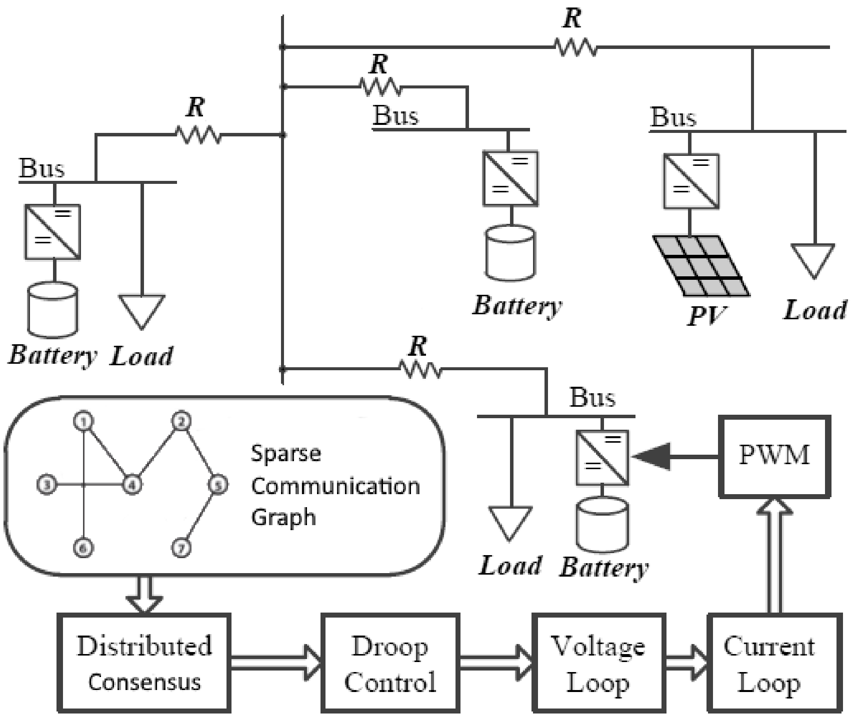

Figure 6.1: Schematic of a solar DC microgrid with batteries and PV panels.

a voltage controllable buck converter and are considered as constant power loads (CPLs). The battery ESSs are connected to the system by DC-DC bidirectional converters and are used to compensate for power mismatch between PVs and loads to regulate the bus voltage.

Conventionally, droop control provides proportional power-sharing among multiple ESSs. The primary control for ESSs satisfies:

$$v_i^{ref} = v_{mg} - r_i^{drp} i_i \tag{6.1}$$

where v_i^{ref} is the set-point voltage of the DC-DC converter, v_{mg} is the nominal voltage of the microgrid, r_i^{drp} is the virtual droop resistor, and i_i is the output current of the DC-DC converter. To achieve proportional power-sharing, the virtual resistance is designed based on the following equation for an individual DG:

$$r_i^{drp} = \frac{\Delta v}{P_{\max}/v_{\min}} \tag{6.2}$$

where Δv is the maximum acceptable deviation of the microgrid voltage, $P_{\max}$ is the maximum power of the converter, and $v_{\min}$ is the minimum acceptable microgrid voltage. Commonly a 5% deviation is an acceptable threshold [4].

The secondary layer effect on the voltage output of the converter is then adjusted by introducing voltage correction terms for each control objective to equation (6.1). In the next section, the structure of the secondary layer control is introduced.

6.3 Secondary layer consensus control

In this section, the mathematical model of the secondary control layer for the DC microgrid is developed. First, the voltage correction terms for the control objectives, voltage regulation, and SoC balancing, are introduced, along with the related SoC dynamics for the batteries. Second, the average consensus protocol for bus voltage regulation is developed. Third, the cooperative control for SoC balancing is developed, and the small-signal stability analysis is described. In the end, the proposed online deep learning framework for load forecast based secondary layer control adjustment is introduced.

6.3.1 Modified droop control for battery systems

DC-DC converters operate at a high PWM (pulse width modulation) switching frequency with at least one switching interval delay (i.e. T_s) in the current control (CC) mode. In Figure 6.2, the diagram of the converter interfacing batteries to the DC microgrid is shown, in which the bus voltage regulation dynamics is designed as an outer-loop between the output voltage of the battery v_i^{ref}, and the local bus voltage v_i. The transfer function for the internal loop is given by $H_i^{v_{ol}}$.

$$H_i^{v_{cl}} = \frac{H_i^{v_{ol}}}{1 + H_i^{v_{ol}}} \ , \ \ H_i^{v_{ol}} = \frac{G_i^v}{sC_i(T_s s + 1)} \tag{6.3}$$

Therefore, the local bus voltage closed-loop transfer function of the DC microgrid is given by:

$$V = \mathbf{H^{v_{cl}}} V^{ref} \tag{6.4}$$

A first-order model is used for the battery per-unit energy level charging and discharging:

$$\dot{SoC_i} = -\frac{v_i i_i}{E_i^{max}} \tag{6.5}$$

where E_i^{max} is the battery charge capacity of the ES system, v_i is the bus voltage and i_i is the converter current. It is assumed that converter loss is negligible.

In the secondary layer control, the voltage reference (v^{ref}) for the DC-DC converter is set by the modified droop control with two correction terms for each

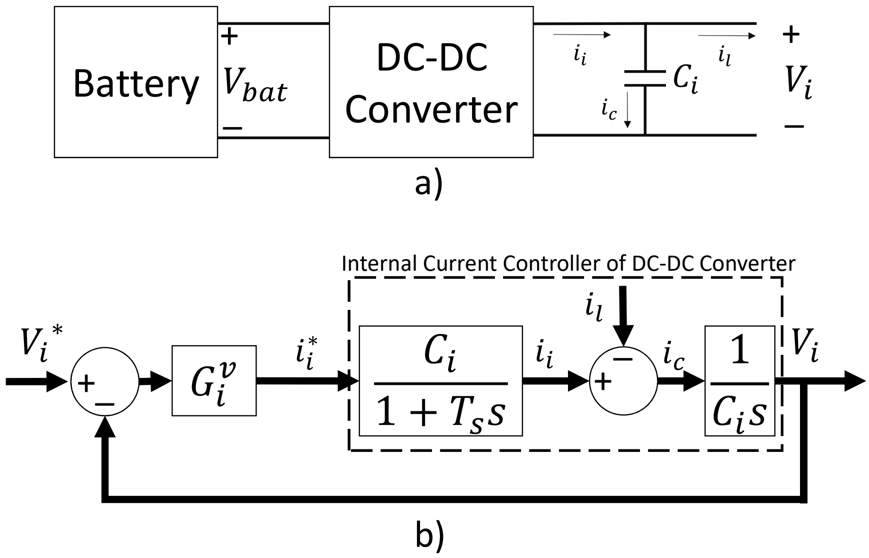

Figure 6.2: DC-DC converter model for interfacing batteries to DC microgrid a) converter circuit, b) block diagram of the internal controller.

bus controller with battery ESSs, as the following:

$$v_i^{ref} = v_{mg} - r_i^{drp} i_i + \delta v_i^v + \delta v_i^{soc} \tag{6.6}$$

where δv_i^{soc} is the SoC balancing correction term and δv_i^v is the bus voltage regulating correction term.

6.3.2 Average consensus for voltage regulation

The secondary layer ES control agents are connected via a sparse communication graph $\mathcal{G}(\mathcal{V}, \mathcal{E})$, with nodes $\mathcal{V} = \{1, \ldots, N\}$ and edges $\mathcal{E}$. Each graph node represents an ES system and the graph edges represent communication links between them. $(i, j) \in \mathcal{E}$ if there is an information flow between node i and node j. The neighbours of node i are given by $\mathcal{N}_i$, where $j \in \mathcal{N}_i$, if $(i, j) \in \mathcal{E}$. The graph adjacency matrix is given by

$$\mathcal{A} = [a_{ij}] \in \mathbb{R}^{N \times N}, a_{ij} = \begin{cases} 1, (j, i) \in \mathcal{E} \\ 0, \text{ otherwise} \end{cases} \tag{6.7}$$

The communication graph Laplacian matrix is given by $\mathbf{L} = \mathcal{D} - \mathcal{A}$, where $\mathcal{D} = \text{diag}\{d_i\}$, and $d_i = \sum_{j=1}^{N} a_{ij}$ is the in-degree of the communication network. $\mathcal{G}$ describes only the communication network between battery ES controller systems. The graph is bidirectional, meaning that each battery ES system can both receive and send information on the same link. Through the communication links, the local consensus controller computes the average values of state variables based on the information from its neighbors $j \in \mathcal{N}_i$. Assuming that the microgrid contains N ES systems, including N battery systems. The average consensus protocol of each battery local bus voltage through the graph $\mathcal{G}$ is:

$$\bar{v}_i = v_i + \int \sum_{j \in \mathcal{N}_i} a_{ij} \left(\bar{v}_j - \bar{v}_i \right) dt \tag{6.8}$$

where $\bar{v}_i$ is the local bus voltage estimation . Therefore, the $\{\bar{v}_i\}$ are exchanged in the communication network between battery controllers for local bus voltage average consensus protocol. The global dynamics of the distributed average consensus protocol are given by:

$$\dot{\overline{\mathbf{v}}} = \dot{\mathbf{v}} - \mathbf{L}\overline{\mathbf{v}} \tag{6.9}$$

Applying the Laplace transform yields the following transfer function matrix for the average consensus protocol [4]:

$$\mathbf{G}_{\text{avg}} = \frac{\overline{\mathbf{V}}}{\mathbf{V}} = \frac{s}{(s\mathbb{I}_N + \mathbf{L})} \tag{6.10}$$

$\overline{\mathbf{V}}$ and $\mathbf{V}$ are the Laplace transforms of $\overline{v}$ and v, respectively.

For a balanced communication graph with a spanning tree, the steady-state gain of the average consensus protocol is given by the averaging matrix:

$$\lim_{s \to 0} \mathbf{G}_{\text{avg}} = Q, \text{where } [Q]_{ij} = \frac{1}{N} \tag{6.11}$$

The final value theorem shows that for a vector of step inputs, the elements of $\overline{\mathbf{x}}(t)$ converge to the global average of the steady-state values $\mathbf{v}^{ss}$:

$$\lim_{t \to \infty} \overline{\mathbf{v}}(t) = \lim_{s \to 0} \mathbf{G}_{\text{avg}} \lim_{t \to \infty} s\mathbf{v} = Q\mathbf{V}^{ss} = \mathbf{v}^{ss} \tag{6.12}$$

To maintain the average battery local bus voltage at the rated value v_{mg}, a PI controller is used. Then, the local bus voltage correction term in (6.6) is then computed as:

$$\delta v_{1i} = H_i \left(v_{mg} - \bar{v}_i \right), H_i = k_{Pi}^{\bar{v}} + \frac{k_{Ii}^{\bar{v}}}{s} \tag{6.13}$$

where H_i is the PI controller, $k_{Pi}^{\bar{v}}$ and $k_{Ii}^{\bar{v}}$ are proportional and integral PI gains, respectively. This PI controller regulates the average value of the local bus voltages of the battery DC-DC converter output to the rated microgrid voltage.

Thus, the bus voltage offset from the primary droop control is compensated.

Another consensus control balances the SoC level among the batteries. The data of $\{SoC_i\}$ are exchanged between neighboring ESSs. The correction term δv_{2i}^b in (5) is defined as:

$$\delta v_{2i}^b = G_i^b \sum_{j \in \mathcal{N}_i} a_{ij} \left(SoC_j - SoC_i\right), G_i^b = k_{Pi}^{SoC} \tag{6.14}$$

where k_{Pi}^{SoC} is the control gain of the SoC cooperative balancing control.

6.3.3 Small signal stability analysis of the control system

The output currents of the ES converters is derived from multiplying the bus voltages with the bus admittance matrix, constructed based on the line and load impedances:

$$I = YV \tag{6.15}$$

The total SoC level dynamics is summarized in vector form based on (6.5):

$$E = MYV, \quad M = diag\{-\frac{v^{mg}}{E_i^{max} s}\} \tag{6.16}$$

The total multi-variable form of the closed-loop secondary and primary control system dynamics is then described as the following, derived from equations (6.6), (6.13), (6.14), and (6.16):

$$ll\mathbf{V} = \quad \left(\left(\mathbf{H}^{\mathbf{v_{cl}}}\right)^{-1} + \left(\mathbf{G^b LM} + \mathbf{r}_{drp}\right) Y + \mathbf{HG}_{avg}\right)^{-1} \tag{6.17}$$

$$\left(\left(\mathbf{H} + \mathbf{I_N}\right) \mathbf{v}_{mg}\right) \tag{6.18}$$

where $\mathbf{G}_{\text{avg}}$ is the transfer function of the voltage average consensus protocol; $\mathbf{v}_{mg}$ is the nominal microgrid voltage, Y_{net} is the microgrid grid admittance matrix, I_N is an $N \times N$ identity matrix.

$$\begin{aligned} &\mathbf{V} = \left[V_1, V_2, \ldots, V_p\right]^T, \mathbf{r}_{drp} = \text{diag}\left\{r_i^{drp}\right\} \\ &\mathbf{H} = \text{diag}\left\{H_i\right\}, \mathbf{H}^{\mathbf{v_{cl}}} = \text{diag}\left\{H_i^{v_{cl}}\right\} \\ &\mathbf{G} = \text{diag}\left\{G_i^b\right\} \end{aligned} \tag{6.19}$$

To analyze the stability of the total dynamics in (6.17), it is assumed that the microgrid voltage reference voltage is:

$$\mathbf{v}_{mg} = \left(v_{mg}/s\right) \mathbf{1}_N \tag{6.20}$$

where $\mathbf{1}_N \in \mathbb{R}^{N\times 1}$ is the vector with all elements equal to one. Using the final value theorem, the steady-state values of the total microgrid dynamics are derived. By defining the steady-state total bus voltage vector, $\mathbf{v}^{ss}$, the final value is:

$$\begin{aligned}\mathbf{v}^{ss} = &\lim_{s\to 0}\left(s\left(\mathbf{H}^{\mathbf{v}_{\mathbf{cl}}}\right)^{-1} + s\left(\mathbf{G}^{\mathbf{b}}\mathbf{LM} + \mathbf{r}_{drp}\right)Y + s\mathbf{H}\mathbf{G}_{avg}\right)^{-1} \\ &\left(\left(s\mathbf{H} + s\mathbf{I}_{\mathbf{N}}\right)\mathbf{v}_{mg}\right)\end{aligned} \tag{6.21}$$

Based on the work in [4], it can be shown that:

$$The\ final\ steady\ state\ value: \ \langle \mathbf{v}^{ss} \rangle = v_{mg} \tag{6.22}$$

6.4 Prioritised (dis)charging of energy storage systems

The primary and secondary layer control strategies described in the previous sections can maintain the first two control objectives (i.e. voltage offset compensation and balancing SoC of ESSs), without the resiliency considerations in the event of generation disconnection. Now this question must be answered: How to increase the time duration for the microgrid to continue its operation without any generation supply. The answer is in the reliability and resiliency of the microgrid. This time duration is dependant on the SoC of the batteries and the load profile on branches. As the exact instant of time for generation outage is unknown, the mathematical model of the resiliency should be independent of this instant. Therefore, in this chapter a load forecast based approach is proposed to increase the endurance time of the microgrid based on the following non-restrictive basic assumptions:

Assumption 1. *The microgrid is based on a single bus architecture and has a radial load distribution on branches.*

Assumption 2. *The capacities of the installed ESSs on the main branches are known to the forecasting adapter unit of the distributed controllers. By knowing the capacity, the outage time can be computed as $T_{outage} = 10h$, which is the time that the ESS supplies the branch on which installed after the supply outage. For example, a 1 kWh storage for a branch with a peak load of 100 W leads to $T_{outage} = 10h$.*

Assumption 3. *Each ESS distributed controller has access to the load prediction for all of the branches in the microgrid. DGs are connected to the single bus architecture via a branch, therefore, the controllers have access to the generation forecast, additionally.*

Table 6.2: Description of the variables for the proposed 2TSA dynamic programming model.

Variable	Definition
$P^{f_1}_{gen}$, $E^{f_1}_{gen}$	First step generation forecast, power and energy
$P^{f_1}_{L_i}$, $E^{f_1}_{L_i}$	First step branch load forecast, power and energy
$E^{f_1}_{diff}$	Load/generation energy difference for the first step
$P^{f_2}_{L_i}$, $E^{f_2}_{L_i}$	Second step branch load forecast, power and energy
$E^{f_2}_{L} = \sum E^{f_2}_{L_i}$	Sum of the branches load forecast energy
$C_{L_i} = \frac{E^{f_2}_{L_i}}{E^{f_2}_{L}}$	Load contribution factor of the branch

The load/generation forecast is predicted based on LSTM deep neural networks due to their advantages, discussed earlier. The amount of training data gets large when all of the controllers broadcast their information to the other controllers, which increases the burden on the communication network significantly. Therefore, in the next section, a distributed learning algorithm is proposed that is based on a DEKF learning model with the neighbor communication.

By knowing the load/generation forecast for each branch of the DC microgrid, a dynamic programme can be formulated which prioritizes the (dis)charging of ESSs based on the corresponding load forecast of the branch. In this chapter a two-time steps ahead (2TSA) programming method is proposed for the dynamic programming of the ESSs. In the first time step, the distributed controllers compute the excess power or supply shortage of distributed generation based on the generation forecast of each branch. Then, the controllers distributively compute the (dis)charging prioritizes based on the second time step prediction and will adjust the SoC balancing distributed controller accordingly. For the simplicity of the presentation, a daily time step is assumed for the results section. In the following, the mathematical model of the prioritizing function is developed.

The variables used in the proposed 2TSA dynamic model are defined in Table 6.2. The programming model consists of two steps, excess/supply shortage energy calculation step, and the (dis)charging prioritization based on the load forecast in the second step. In the first step, distributed LSTM models provide the load forecast and the generation of the branches. This information is available at every distributed controller because LSTM training was run distributively, according to the learning framework provided in the next section. Therefore, the variables $P_{gen}^{f_1}$, $E_{gen}^{f_1}$, $P_{L_i}^{f_1}$, and $E_{L_i}^{f_1}$ are computed for the first step. Knowing the generation and load energy forecast, the different show how much energy is available for (dis)charging the storage in the first step:

$$E_{diff}^{f_1} = E_{gen} - \sum E_{L_i}^{f_1} \tag{6.23}$$

The objective is now to assign this energy difference to the ESSs, to increase the endurabiliy of the microgrid, in the event of generation failure. Therefore, a load contribution factor is defined, $C_{L_i} = \frac{E_{L_i}^{f2}}{E_L^{f2}}$, that forms the basis for prioritized (dis)charging of the ESSs. The priorities are ordered from the branch with the highest load contribution to the branch with the lowest load contribution, in the second step:

$$E_{max_i}^{new} = \frac{C_{L_i} \times E_{diff}^{f_1} + SoC_i \times E_{max_i}^{old}}{E_{diff}^{f_1} + \sum(SoC_i \times E_{max_i}^{old})} \tag{6.24}$$

The new calculated value for the maximum SoC of the ESS, adapts the parameter E_i^{max} in equation (6.5):

$$\dot{SoC}_i = -\frac{v_i i_i}{E_{max_i}^{new}} \tag{6.25}$$

Then, the proposed secondary layer SoC balancing controller distributively regulates the balanced charging of ESSs with the new priorities, defined by the $E_{max_i}^{new}$. The new outage time, T_{outage} is re-calculated with the new SoC condition for each branch, according to Assumption 2:

$$T_{outage} = \frac{P_{max_i}}{SoC_i \times E_{max_i}^{new}} \tag{6.26}$$

Results in Section 6.6 provides the analysis on the prioritized SoC balancing for a case study 380 V DC microgrid.

6.5 Short-term forecasting of energy supply and demand

At each node i, the load forecast LSTM predictor sequentially receives $\{p_{i,t}\}_{t\geq 1}, p_{i,t} \in \mathbb{R}$, and matrices, $\{X_{i,t}\}_{t\geq 1}$, defined as $X_{i,t} = \left[x_{i,t}^{(1)} x_{i,t}^{(2)} \ldots x_{i,t}^{(m_t)}\right]$, where $x_{i,t}^{(l)} \in \mathbb{R}^p, \forall l \in \{1, 2, \ldots, m_t\}$ and $m_t \in \mathbb{Z}^+$ is the number of columns in $X_{i,t}$. $p_{i,t}$ is the sampled load power/generation power, and $X_{i,t}$ is the sampling timestamps used for training the LSTM network, which changes with time t, as

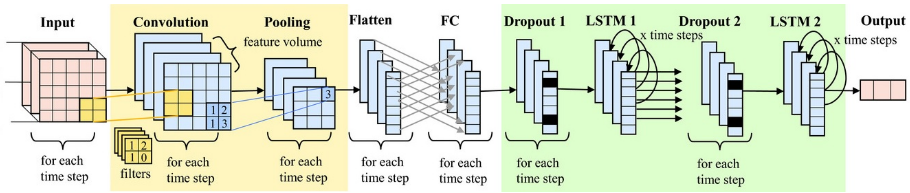

Figure 6.3: Data processing flow chart in the LSTM neural network [1]. The input layer consists of convolution and pooling layers for feature extraction. At first the input data are injected as multidimensional time-series into the neural network. The convolution layer applies different filters to the input data and the pooling layer compresses the output of the previous steps using mean pooling. LSTM neurons learn the history output from previous layers by their internal recurrent loops. Finally, the output is derived for the predicted time series in the next time step.

microgrid operation continues. In this chapter, a daily sampling timestamp set ($\{0, 1, \ldots, 24\}$) is used, but a longer or shorter training set can also be used, for example weekly or monthly. In this network, each node i aims to learn a certain relation between the desired value $p_{i,t}$ and $X_{i,t}$ signals. After receiving $X_{i,t}$ and $p_{i,t}$ samples, each node i first updates its belief about the relation and then exchanges an updated information with its neighbours. This information exchange helps faster training and results in a more accurate model, due to collective training of the multi-agent system. After receiving $X_{i,t}$, each node i estimates the next signal $p_{i,t+1}$ as $\hat{p}_{i,t+1}$. Based on $p_{i,t+1}$, each node i calculates the loss function $loss\left(p_{i,t+1}, \hat{p}_{i,t+1}\right)$ at time instance $t+1$.

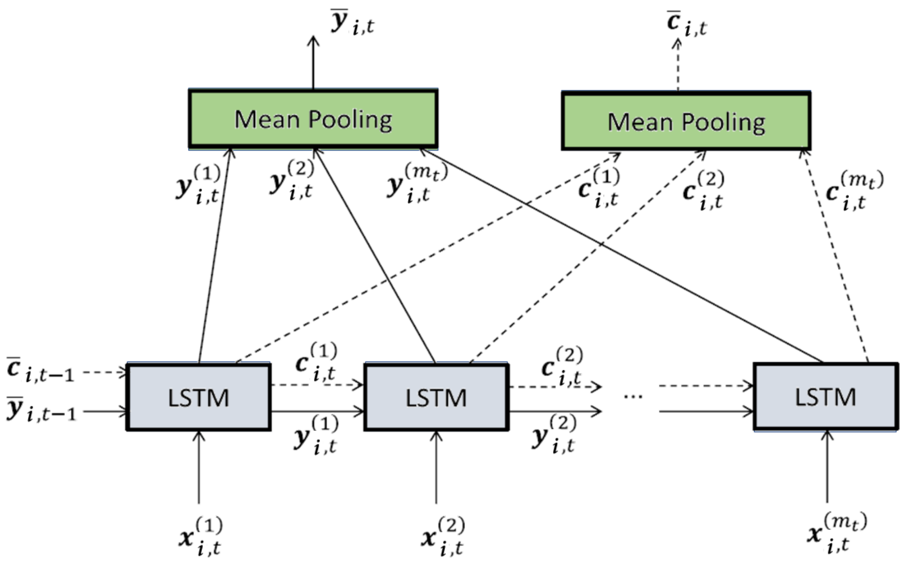

Figure 6.4: Distributed LSTM neural network structure for each node. LSTM units learn the time series sequences with their internal recurrent feedback path and memories.

The data flow chart in the layers of the LSTM neural network is illustrated in Figure 6.3. The input layer consists of convolution and pooling layers for feature extraction. At first, the input data are injected as multidimensional time-series into the neural network. The convolution layer applies different filters to the input data and the pooling layer compresses the output of the previous steps using mean pooling. LSTM neurons learn the history output from previous layers by their internal recurrent loops. Finally, the output is derived for the predicted time series in the next time step. Mean pooling or average pooling layer performs down-sampling by dividing the input into rectangular pooling regions and computing the average values of each region in the input matrix.

Each node i generates an estimate $\hat{p}_{i,t}$ using the LSTM architecture. The LSTM network architecture without peephole connections is used in this chapter. The input $X_{i,t}$ is first fed to the LSTM architecture as illustrated in Figure 6.4, where the internal equations of the neural network are given in [121].

Given the outputs of LSTM for each column of $X_{i,t}$, shown in Figure 6.4, the estimate for each node i is generated as:

$$\hat{p}_{i,t} = w_{i,t}^T \overline{y}_{i,t} \tag{6.27}$$

where $w_{k,t} \in \mathbb{R}^n$ is a vector of the regression coefficients and $\bar{y}_{k,t} \in \mathbb{R}^n$ is a vector obtained by taking average of the LSTM outputs for each column of $X_{k,t}$, i.e. known as the mean pooling method, as described in Figure 6.4.

By simplifying this model in Figure 6.4 with the LSTM equations in [121], the following nonlinear state space form for each node i will be derived:

$$\begin{aligned}
\overline{c}_{i,t} &= \Omega\left(\overline{c}_{i,t-1}, X_{i,t}, \overline{y}_{i,t-1}\right) \\
\overline{y}_{i,t} &= \Theta\left(\overline{c}_{i,t}, X_{i,t}, \overline{y}_{i,t-1}\right) \\
\theta_{i,t} &= \theta_{i,t-1} \\
p_{i,t} &= w_{i,t}^T \overline{y}_{i,t} + \varepsilon_{i,t}
\end{aligned} \tag{6.28}$$

where $\Omega(\cdot)$ and $\Theta(\cdot)$ represent the nonlinear mappings performed by the consecutive LSTM units and the mean pooling operation as in Figure 6.4, and $\theta_{i,t} \in \mathbb{R}^{n_\theta}$ is the neural network weight vector. Furthermore, $\varepsilon_{i,t}$ represents the error in observations and it is a zero mean Gaussian random variable with variance $R_{i,t}$. The DEKF algorithm is used for distributed training the LSTM network. DEKF was proposed for distributed learning of neural networks and has a higher learning performance and a faster convergence rate comparing to the commonly used stochastic gradient descent (SGD) method. The details of the DEKF training method are discussed in [121].

Due to the choice of short-term energy forecasting horizon, the predictions models are only valid for the same time duration chosen for the horizon. Therefore, to have a robust control system that is able to continuously stabilize the microgrid and prioritise the (dis)charging of the energy storage systems, the prediction models should be built regularly at the end of the last forecasting horizon. This operation consists of data collection and re-training of the LSTM deep neural models, which provides robustness against the prediction model uncertainties due to the short-time forecasting horizon. In Figure 6.5, the operations in the proposed control system are illustrated. The three main operations are: LSTM prediction modelling, ESS (dis)charging priority calculation, and the ESS interfacing DC-DC converter operation.

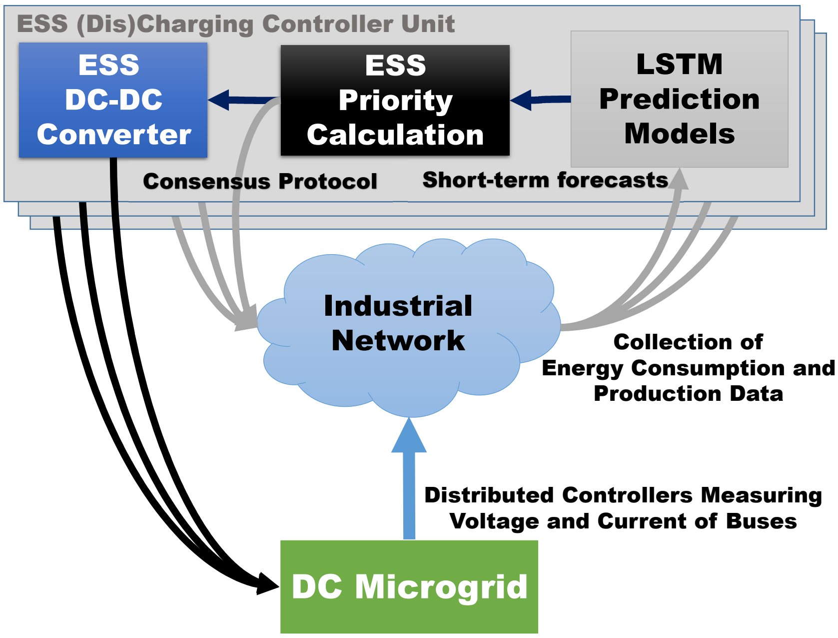

Figure 6.5: Summary of the operations in the proposed distributed forecast-based consensus control system. The ESS controller unit consists of three components: LSTM prediction models, ESS (dis)charging priority calculation, and the ESS interfacing DC-DC converter.

6.6 Experimental results and discussion

To validate the performance of the proposed control strategy, we have used a 380 V data centre DC microgrid real-time HIL test bench with 5 buses as the main branches. The test bench consists of the dSPACE real-time simulators (SCALEXIO and MicrolabBox), and the Internet of things (IoT) embedded controllers for each bus of the case study, which run the forecast based control tasks. Load and generation forecast models are optimized using "Tensorflow

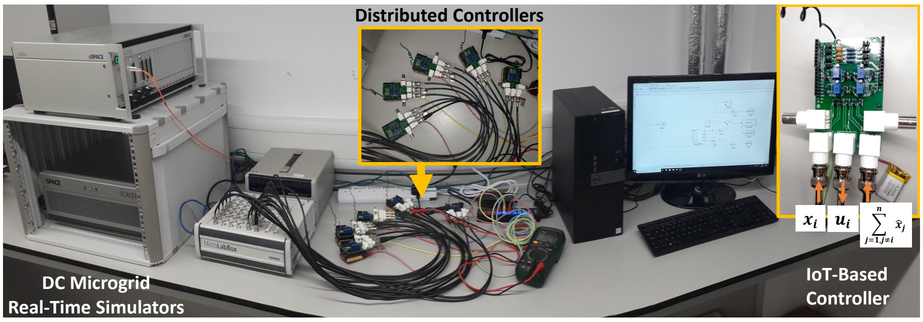

Figure 6.6: Laboratory HIL test bench used for the performance analysis of the proposed forecast based distributed control strategy. The test bench consists of dSPACE real-time simulators (SCALEXIO and MicrolabBox), and IoT embedded controllers for each bus of the case study, which run the forecast based control tasks. Load and generation forecast models are optimized using "Tensorflow lite for microcontrollers" deep learning framework released by Google. The embedded controllers are based on the Seeduino development boards with ATSAMD21G18 32-Bit ARM Cortex M0+ CPU.

lite for microcontrollers" deep learning framework released by Google™. Load forecasting models are developed in Python programming language, and Keras deep learning interface is used for online training of the LSTM models using the DEKF algorithm.

In this setup, a Raspberry Pi computer with the supporting communication modules for the gateway operation is used. This gateway receives the data from the measurement nodes via MQTT (Message Queuing Telemetry Transport) protocol. Thingsboard® software implements the MQTT broker, which is used for data archiving and processing. By using the mentioned protocols and devices, the microgrid control system cost becomes considerably cheaper than other smart metering technologies such as IEC 61850. The architecture of the test bench and the communication graph is shown in Figure 6.7. The laboratory setup is also shown in Figure 6.6.

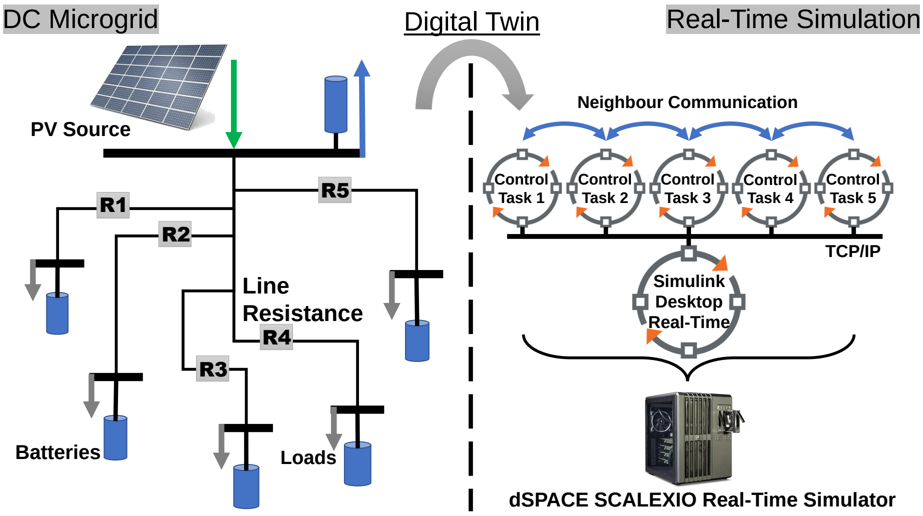

Figure 6.7: Real-time simulation architecture of the distributed controllers with neighbor communication graph, and the 380 V DC microgrid.

On each bus, a 400 Wh battery ESS is installed with the nominal maximum power at 400 W that leads to nominal $T_{outage} = 1h$, according to the calculation in Assumption (2). Furthermore, to show the effectiveness of the prioritized (dis)charging method, the maximum load of each bus is different as shown in Table 6.3. Also, the initial SoC of ESSs is set to different values (i.e. 80%, 90%, and 100%) as shown in the same table. Line and controller parameters are also provided in Table 6.4.

The microgrid is emulated for three consecutive days using the real residential sample PV data from 11 July to 13 July 2014 of the UK Power Network [122]. The PV generation forecasting LSTM model is trained by the whole month data of July 2014 from the same source.

For this experiment, the whole month of July 2014 is used for the training, testing, and validation. The forecasting horizon was decided to be three consecutive days, and the dataset is divided into 80%, 10%, and 10% for the LSTM model training, testing and, validation purposes, respectively, and the data selection for each subset was done randomly.

Table 6.3: Maximum load power of each bus and the initial SoC of ESSs.

Bus Number	Constant Power Load (W)	Initial SoC (%)
1	110	80%
2	120	100%
3	120	80%
4	130	100%
5	120	90%

The load profile dynamics are generated following the total load profile from the same source to allow testing different transient conditions. For each day, the total load of the buses increases from 20% to 100% and then decreases from 100% to 20%. This allows testing the performance of the proposed method during peak load and low load values in the daily forecast horizon. Figure 6.8 shows the PV generation and the load power. The load profile is chosen as the worst case scenario and it is not based on real load pattern. To highlight the advantages of the proposed control strategy, the experimental results are derived in two configurations:

- **Configuration A**: Traditional droop control, which is a decentralized method commonly used for comparison.
- **Configuration B**: Proposed forecast based distributed control system using LSTM energy forecasting method.

Table 6.4: Parameters of the distributed controllers for the HIL simulation.

R_{dc}	10 Ω	k_{Pi}^{SoC}	5000	$k_{Pi}^{\bar{v}}$	500
L_{dc}	7 μH	r	0.2533	$k_{Ii}^{\bar{v}}$	10

The microgrid is emulated for three consecutive days with the initial E_{max_i} of 400 Wh for the first day as outlined in Table 6.3. On the third day, the PV source is disconnected and the microgrid continues its operation only by the battery ESSs. The disconnection happens after 12 hours.

In configuration A, only the droop control system stabilizes the microgrid, in which the local droop controller acts based on local measurements only. The results for configuration A are shown in figures Figure 6.9, Figure 6.11, and Figure 6.13. As can be seen in Figure 6.9, the ESSs run out of energy between 14h to 19h on the third day, one by one. This is due to the disconnection of the PV sources at time 12h.

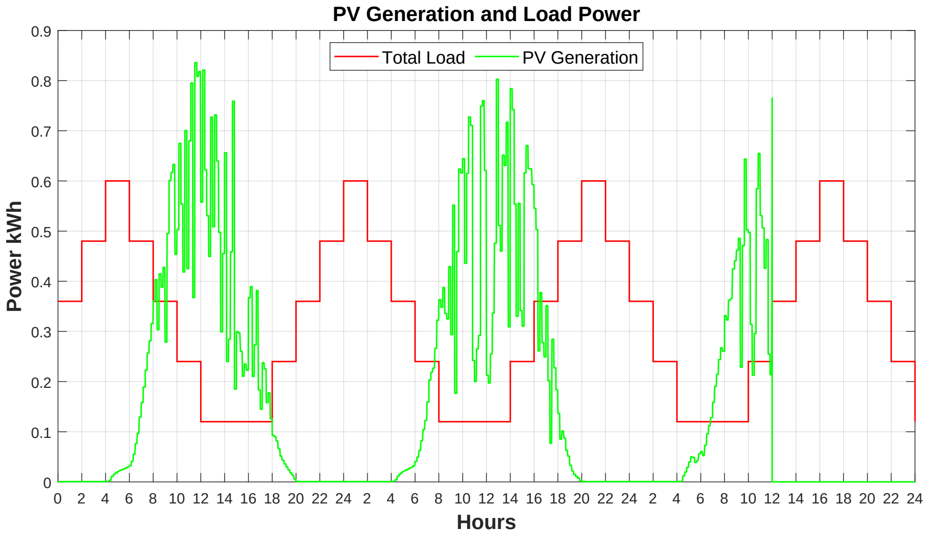

Figure 6.8: Case study PV generation and total load profile. The total load profile was generated as a multi-step one to better show the response of the control system to disturbances such as fast load switching.

After the ESSs are depleted, the branch is switched off, therefore the voltages drop to zero as shown in Figure 6.11. The output power of the ESSs is also shown in Figure 6.13 and Figure 6.13. It can be observed that there is a voltage offset of 1 V from the nominal 380 V due because of the droop controllers.

The results for configuration B, the proposed control strategy, is shown in Figure 6.10, Figure 6.12, and Figure 6.14. In this strategy, $E^{new}_{max_i}$ of the second day, are calculated using equation (6.24), based on the third-day forecast of distributively trained LSTM models. As shown in Figure 6.10 and Figure 6.13, the proposed prioritised (dis)charging has changed the power balance in the second and third day, to increase the priority of bus 4 ESS for getting charged with a higher rate than the others. This is because the load on bus 4 is higher comparing to the other buses. Also the charging rate of ESS at bus 1 is decreased due to the lower load comparing to the buses 2, 3, and 5.

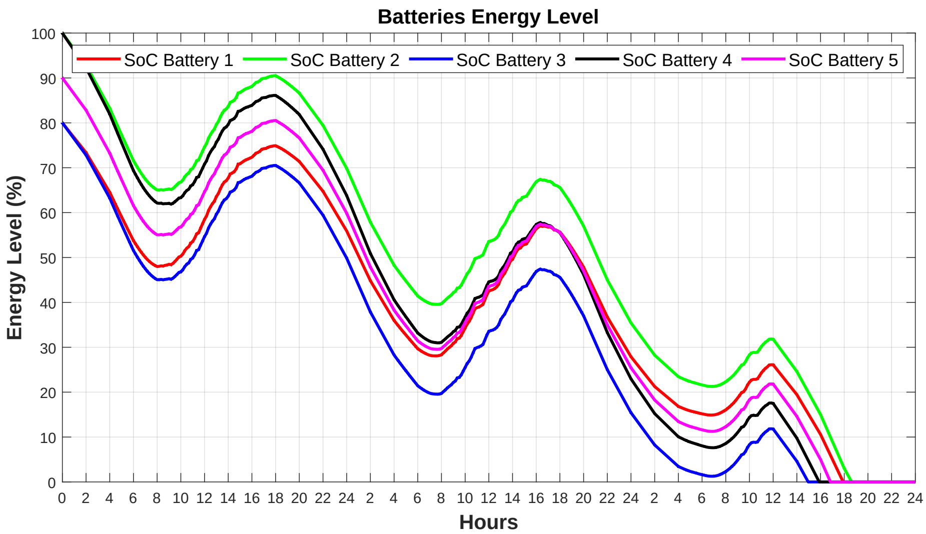

Figure 6.9: Configuration A: SoC of ESSs. After the PV outage in the third day at 12h, the ESS has run out of energy from 14h to 19h. When energy level becomes zero, the corresponding energy storage system becomes inactive and gets disconnected from the main grid.

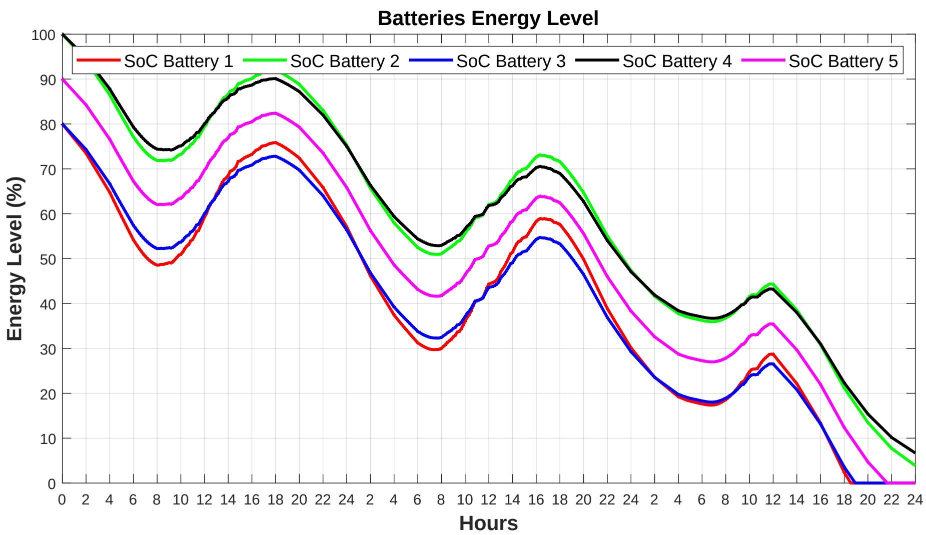

Figure 6.10: Configuration B: SoC of ESSs. After the PV outage on the third day at 12h, the ESS has run out of energy from 18h to the following day. This shows how the prosed forecast-based control increased the endurability of the microgrid in cases of a supply outage.

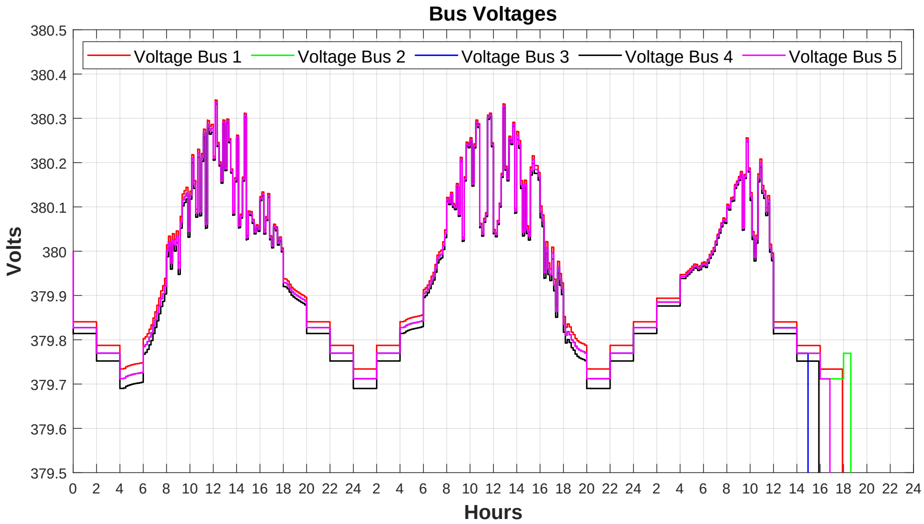

Figure 6.11: Configuration A: Voltage of buses. There is a large voltage offset of 1 V from the nominal 380 V due because of the droop controllers. The voltage becomes 0 after the branch ESS has run out of energy.

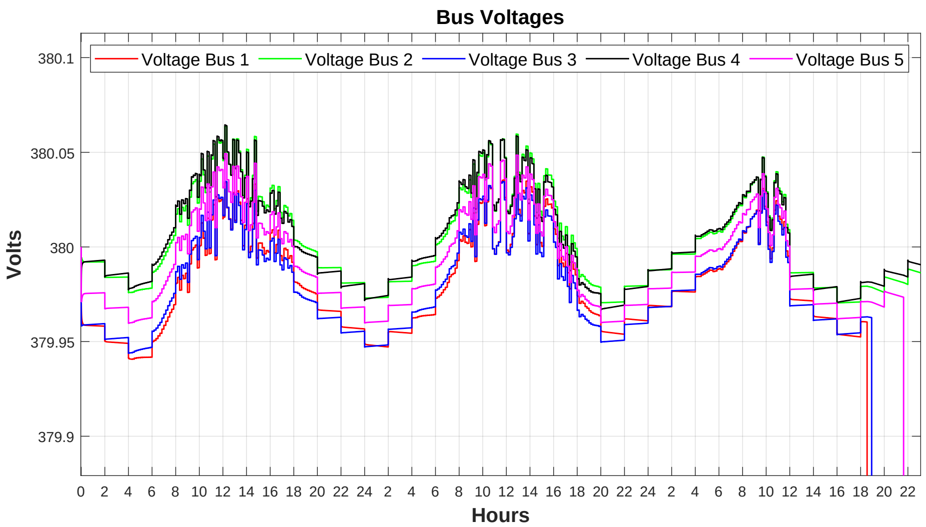

Figure 6.12: Configuration B: Voltage of buses. The voltage offset is considerably lower comparing to the droop controllers, less than 0.1 V (90% less). The voltage becomes 0 after the branch ESS has run out of energy.

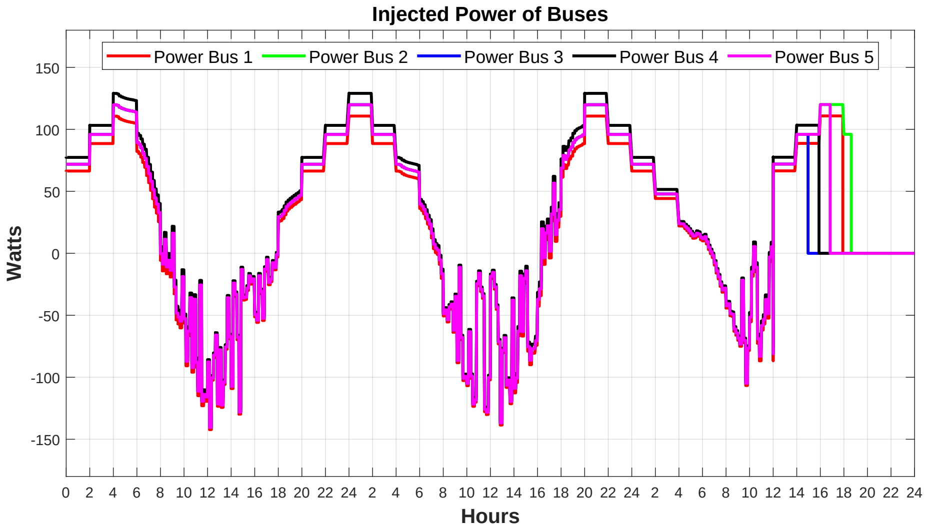

Figure 6.13: Configuration A: Injected power of ESSs with the local droop controllers.

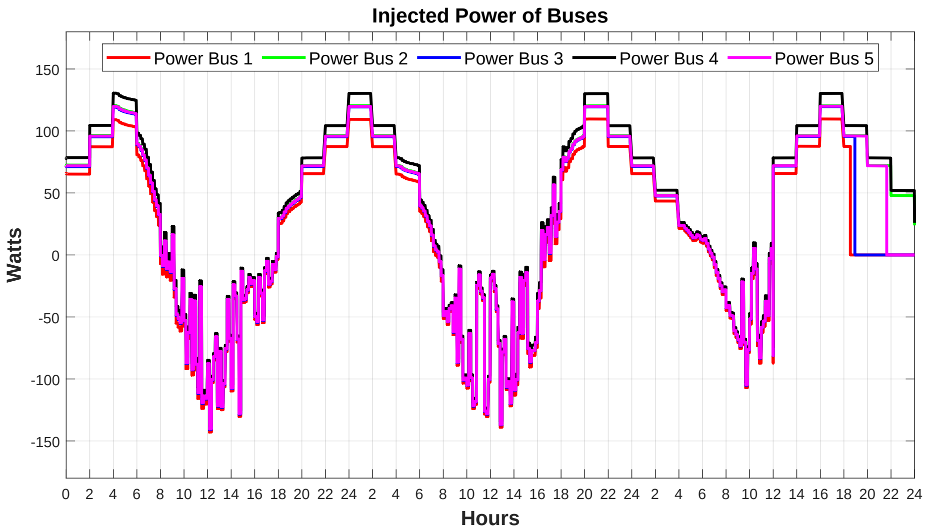

Figure 6.14: Configuration B: Injected power of ESSs with the proposed forecast based control system.

On the third day, it can be seen in Figure 6.10 that the ESSs run out of energy after 18h. This is because of the prioritized (dis)charging method that has distributed the PV energy on the second day based on the load forecast of the third day. Furthermore, the voltage offset is considerably lower comparing to the droop controllers, less than 0.1 V (90% less). The voltage becomes 0 after the branch ESS has run out of energy.

The increase in the continuity of the microgrid operation confirms that the resiliency and the endurability of the microgrid are increased by at least 4 hours of longer operation after the fault on PV generation. Furthermore, the voltage of the microgrid is stabilized with lower offset comparing to the decentralized droop control system as shown in Figure 6.11 and Figure 6.12.

6.7 Summary

A novel distributed load forecast based control for DC microgrids was presented in this chapter. The proposed control strategy achieves the following objectives:

- Stabilizing the bus voltages co-designed to balance the SoC levels of ESSs in a DC microgrid.
- Prioritized (dis)charging controller for ESSs based on short-term energy forecast of the branches to achieve higher endurability for the DC microgrid.
- Integration of the load forecasting unit in the secondary control layer of the microgrid based on LSTM neural network with DEKF learning algorithm.

The load and generation profiles are predicted using LSTM deep learning models. Due to the large training data requirements of LSTM models, DEKF distributed learning algorithm is used to improve the prediction convergence time. Hardware in-the-loop real-time simulation results confirm the validity of the proposed control strategy for an islanded 380 V DC microgrid. The proposed 2TSA algorithm can get enhanced by considering different ESSs characteristics, in the future.

Chapter 7

Conclusion and future work

This thesis provides a study on event-triggered distributed control system and state estimator designs for DC microgrids based on constrained communication networks. The developed distributed control and estimation strategies are designed for operation over constrained communication networks that have low data transmission speed and no central coordinator for synchronization of the control tasks. This forms a multi-agent environment in which the controller agents cooperatively achieve the DC microgrid control objectives. These objectives are voltage stabilization, proportional power-sharing, and balancing of ESSs' energy levels.

To overcome the communication network constraints, event-based controllers and estimators are designed, which effectively have reduced the network traffic and as a result, provided higher throughput with reduced delays for the real-time control loops in the primary and secondary control layer of DC microgrids. The developed controllers' operations are distributed to remove the single point of failure, which leads to use cases such as autonomous islanded microgrids, smart villages, and plug-and-play mobile microgrids. The feasibility of the control and estimation strategies is validated in several DC microgrid experimental setups in the real-time control and power (RCPS) laboratory in Queen Mary University of London (QMUL). The mathematical analysis and the experimental results confirm the performance of the proposed control and estimation strategies for DC microgrids to operate with higher reliability and robustness in the delivered power quality.

7.1 Summary of contributions

For the sake of brevity, this section hereby overviews the key contributions of this work on distributed control and estimation of DC microgrids based on constrained communication networks:

- Analysis of distributed control systems for DC microgrids over communication networks and the corresponding control challenges.
- Analysis and design of an event-based Kalman consensus filter (KCF) for both state estimation and distributed control of DC microgrids.
- Analysis and design of an event-based consensus control strategy for DC microgrids that is resilient to communication delays and change of communication graph topology.
- Analysis and design of an optimized state estimator for DC microgrids with adaptive threshold SoD sampling strategy that is resilient to communication delays.
- Analysis and design of a distributed control system with short term load forecasting for optimized (dis)charging of ESSs using the proposed 2TSA prioritized (dis)charging strategy.
- Development of an experimental test bench for operational analysis of distributed control systems in DC microgrids based on dSPACE SCALEXIO real-time simulators and embedded constrained controllers over wireless communication.
- Analysis of IoT communication protocols and patterns for data sharing between the controllers such as publish/subscribe, request-response, and event multicasting.

7.2 Future work

In this section, a technique for the effective realisation of the topology assignment algorithm is briefly introduced, which has the potential to be deployed further in a microgrid with distributed controllers. This concept is based on directional communication links and beamforming techniques, developed for next-generation wireless and telecommunication infrastructures. Directional links can be summarised as a group of communication technologies, operating based on directional antennas and feeding systems. There are many advantages associated with the utilisation of such radio links over omnidirectional systems, including 1) lower interference with other nodes, 2) improved spatial reuse and spectrum efficiency, 3) longer transmission range allowing DGs far from each other to communicate, and 4) lower power requirement and consumption, due to the inverse proportion of minimum transmission power to antenna gains.

In this regard, beamforming methods, as an effective approach to introduce an extra layer of control over transmission and propagation of signals, can be further employed to generate distinct radio beams with significant gains, to accommodate desired directional transmission in wireless sensor networks (WSNs), and to realise proposed topology assignment algorithm [123, 124]. This would result in transmission being only carried out in desired directions, which could significantly reduce contention and traffic in the channel. Once the decision is made on network topology, the beamforming-aided system updates the communication core in the microgrid among DG controllers.

The recently proposed IEEE 802.11ac wireless local area network (WLAN) standard has adopted beamforming technology for the implementation of directional radio links. This can be further integrated as part of practical system design and performance evaluation of studied DC microgrid. In the following, three different beamforming methods are discussed and compared in terms of transmission gain. In particular, the gain parameter is chosen for comparison, as it has a direct effect on link capacity. Increased capacity obtained by directional links reduces transmission delay to a great extent. Different types of beamforming methods can be briefly described as [125]:

- *Switched-beam systems*: A fixed and pre-defined set of weights are applied to different antenna elements, to generate a uniform set of radio beams in terms of magnitude and phase values, to have control over electrical properties at each element of the array, and to further conduct electronic beam steering for the realisation of directional transmission. Moreover, when both transmitter (Tx) and receiver (Rx) are aware of the direction of transmission towards each other, transmission gain can be modelled by $G_d = G_t \times G_r = K^2$, where G_t and G_r are directional gains of Tx and Rx, respectively, and K is the number of elements at either end of the radio link [126].

- *Adaptive array systems*: Unlike the previous case, they adapt their weights to maximise the resulting signal-to-noise ratio (SNR), which helps to cope with multipath phenomena by adaptively changing radiation patterns. Although this comes at expense of added cost and complexity. Transmission gain can also be expressed as $G_a = (2\sqrt{K})^2 = 4K$ [125].

- *MIMO links*: A multiple-input multiple-output (MIMO) link utilises digital adaptive arrays at both ends of the radio link, to provide spatial multiplexing and diversity, to increase the capacity of the link, and to further generate multiple independent data streams. Besides, produced gain provides an increase in Shannon link capacity C, which is given by the following equation [125]:

$$C_m \approx K.C = Klog_2(1+\rho) \tag{7.1}$$

(ρ is the average SNR at any receiver antenna).

Hence, deployment of beamforming technology for event transmission will: (1) reduce transmission delay, as radio link is only established when the event is generated; (2) establish a deterministic communication behaviour (rather than a stochastic one) that significantly increases the reliability of NCS; (3) increase stability region of an event-triggered control strategy that is typically prone to event transmission delay.

Power systems are moving toward deep integration with communication and distributed control systems. This integration is not easy as expertise in different domains are required. Designing control systems for DC microgrids is a challenge as there is no common set of standards that are agreed on for DC microgrids. The only available standards for DC power systems are mainly related to data centers that operate on DC battery reserve. However, due to the limited operating modes of data centers comparing to microgrids, those standards don't cover the existing challenges in integration of RES.

There is an important standard under development in "DRI/2030.10 - Distribution Resources Integration WG/Remote DC Microgrid" workgroup of Institute of Electrical and Electronics Engineers (IEEE). This standard covers the design and operation of a DC microgrid for rural or remote applications based on extra low voltage DC to reduce cost and simplify stability. This standard was in its early stages of drafting at the time of writing this thesis, however future compatibility with this standard was considered in this thesis.

This work can be further extended in the following directions to cover the limitations and also investigate new types of distributed control systems over constrained communication networks for DC microgrids:

1. In this work, the effect of packet dropouts was abstracted via the medium access control (MAC) layer. Commonly, MAC layer protocols re-transmit the payload in the event of dropouts, which can be abstracted by a constant delay in the transmission of the payload from higher-level stacks such as the control system. This assumption is completely valid as long as the payload is received after a fixed number of trials. However, if the link is disconnected and no re-connection scheme is available, the control system should be updated accordingly. The proposed control system in Chapter 4 is resilient to switching topologies, but the detection of the need for topology switching and how fast it should operate can be the topic of future research.

2. The time delay considered in this thesis was assumed to be constant or with very small variations. This is an acceptable assumption when the distributed controller does not share the medium for peer to peer communication, which might be directional as well. From the practical aspects, variable time delays increase the computational complexity for the controllers due to variable prediction horizons in the event intervals. Therefore, the total cost is usually balanced by using more expensive communication technologies that provide a reliable deterministic delay. However, with the advances in computational technologies such as quantum computing, the variable horizon predictions might become feasible, which can be considered as a future work of this thesis.

3. The cybersecurity aspects of the proposed control systems were briefly studied in Appendix A. However, the cybersecurity considerations are not fixed and will change over time as new technologies and methods are introduced. A major issue for microgrids and in general power systems is to find a reliable platform that is open to feature updates for new protection and security schemes. Therefore, an open computational and control platform either at the software or hardware level is required that enables the power system designers to implement and analyse different control and cybersecurity methods for the desired operation of the microgrid.

4. The event-triggered protocols studied in this thesis were designed to operate on processors with very low computational resources. However, more powerful processors and field programmable gate arrays (FPGAs) are finding their place as their prices getting cheaper. The power of these

computational technologies could be further utilized with more advanced event-triggered protocols such as the ones with finite horizon predictors. Even machine learning training algorithms for load forecasting have the potential to run on these devices without relying on specialized servers. Therefore, this subject could be further studied and compared with the results provided here.

Appendix A

Appendix: Cyber Secure Operation of Distributed Systems

Distributed control systems are designed to stabilize microgrids and guarantee their continuous operation affected by the intermittent nature of renewable energy sources and sudden load changes. Therefore, it is crucial to preserve the security of controlling tasks against malicious cyber attacks. In this regard, the microgrid installer has to set up advanced intrusion detection and protection schemes to isolate the operations of controlling tasks. However, if the control system is inherently integrated with smart security regulators, the operational robustness increases while the complexity of the first security layer can be considerably reduced. Therefore, a novel distributed transactional control architecture is briefly discussed in this appendix for smart DC microgrids that integrates the cybersecurity regulators inside each distributed controller to provide inherent security functions in the control system operation. The proposed security regulators operate in a distributive manner to eliminate a single point of failure. These regulators are designed based on a distributed ledger with the Tangle transactional model for reliable detection of anomalies caused by malicious attackers where each controller validates the consensus reached with the other controllers in the network.

There are various distributed ledger technologies today that can be used in the realisation of transactional microgrids. The most popular ones are blockchain and directed acyclic graph (DAG). Most of the blockchain technologies exhibit high computational complexity due to the validation process of long ledgers [127]. Therefore, due to the real-time constraints and necessity for fast anomaly detection, we propose the usage of Tangle DAG in this appendix to implement the distributed ledger.

A.1 Transactional architecture for cyber security of microgrids

In this section, an overview of the proposed distributed transactional control architecture for cyber secure DC microgrids is provided (see Figure A.1), which has the following three main objectives:

- **Voltage stabilization:** The voltage deviation of buses must not be more than a predefined percentage from the nominal microgrid voltage.
- **Proportional power sharing:** Load power has to be shared between the DGs and ESSs with respect to their power supply capacity.
- **SoC balancing of ESSs:** The (dis)charging of ESSs must be managed to achieve a balanced SoC among all the battery storage systems for longer operation of the microgrid especially in the event of supply shortages.

A DC microgrid mainly consists of DGs, ESSs, and loads. The DGs and ESSs are connected to the common bus via an interface, i.e DC-DC converter operating in current control mode (CCM). Each battery storage system has a local controller able to share information with the other controllers via the microgrid communication network. A distributed control approach is adopted and the publish-subscribe communication pattern is used for data sharing between the controllers. In the publish-subscribe pattern, each controller subscribes to the important variables of the other controllers and publishes any change that occurred in the shared variables to its subscribers.

Message queue telemetry transport (MQTT) protocol is the most commonly used protocol for machine to machine (M2M) communication, which works based on publish-subscribe communication pattern. The shared variables between the controllers are grouped under different topics, and the data can be encoded in any format such as Javascript object notation (JSON) or concise binary object representation (CBOR).

To validate the data published by the distributed (local) controllers, a transaction validation framework is integrated using the Tangle distributed ledger. The distributed controllers publishing data streams through the communication network create transactions of the historical data shared between the controllers on a regular basis.

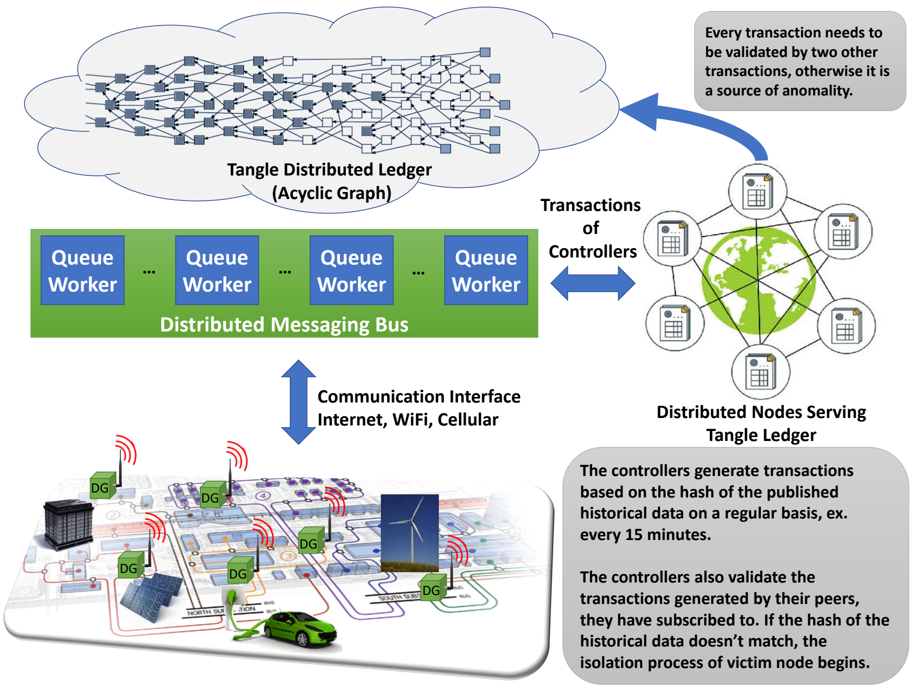

Figure A.1: Proposed distributed transactional architecture for cyber secure DC microgrid control system.

The transactions generated by the controllers will be kept on the distributed ledger, which can be either private or public, and consists of several distributed synchronized servers. We assume the transactions are created on a regular basis and the time between each transaction determines how fast the malicious activity can be detected. Even though setting short intervals between transactions may reduce the probability of a malicious attack, it can increase computational costs depending on the capacity of the controlling nodes and the communication infrastructure used.

In the proposed architecture, the controller nodes cooperatively achieve the DC microgrid objectives using distributed average consensus protocol. In this protocol, limited neighboring controllers communicate with each other in the communication graph. Therefore, controllers do not subscribe to every controllers' shared variables. In the Tangle distributed ledger, the transactions are fee-less and they can contain both data and currency. However, the data transfer feature is mainly used for the purpose of this architecture.

The transactions' data size is limited and the historical data shared by the controllers can not be included in their raw representation for security considerations. A special hashing mechanism is then required to compress and uniquely represents the historical data of the corresponding transaction interval for validation purposes. Here we propose the use of MD5 message-digest hashing algorithm, which is able to produce 128-bit hash values of the historical data, i.e. the time-series of the shared variables. This information will be further encrypted and signed by the controllers' certificate before being added to the distributed ledger to make the transactions tamper-proof and immutable (i.e. the details of the transactions can not be changed in any future time).

The tangle distributed ledger requires that the transactions are validated by at least two other transactions. Therefore, at least two other controllers should subscribe to the data shared by any controller. The security regulator of each controller computes the hash of the subscribed (historical) data on its own, and if it cannot validate the hash code, it means a malicious attacker has published invalid information in the communication network, or it has already taken control of a controller node. After the intrusion detection, the victim controller node (along with the corresponding DG or ESS under its control) is isolated or disconnected from the rest of the system for a temporary period until the issue gets solved. This protection guarantees continuous operation of the DC microgrid in case of malicious attack and losing control of the energy supply node. The details of the isolation scheme are provided in Section A.3.

A.2 Record of historical data for validation of transactions

The average consensus protocol used for modelling the DC microgrid dynamics is designed in continuous time, which is not useful for the purpose of historical data validation. Since the transactions require the hash of the historical data in their limited size, the average consensus protocol should be designed in discrete time. In our previous work [5], we designed an event-based average consensus protocol that only publishes the change in shared variables instead of time-triggered sampling. This provides optimal use of the communication network and a discrete number of historical data to generate the MD5 hash form. Hence, the following event-triggered consensus protocol from [5] will be used in real-time implementation of the distributed control system:

$$\dot{x}_i = u_i(t) = -\sum_{j=1}^{N} L_{ij}\hat{x}_j(t) \tag{A.1}$$

The increasing sequence $\{t_l^i\}_{l=1}^{\infty}$ and $\{t_{l+1}^i - t_l^i\}_{l=1}^{\infty}$, are called the triggering times and inter-event times of agent i, respectively. In order to simplify the notations, let The aim will then be finding the correct event-triggering condition to prove the stability of the proposed consensus protocol.

A.3 Tangle distributed ledger for real-time validation of controllers' transactions

The tangle is a network data structure designed to facilitate a range of secure transactions. Like blockchain, a distributed ledger involves a group of independent operators performing an array of data-transfer transactions and reaching the consensus on ownership. There is no reliance on centralized authorities, and it does not require a time consuming, computationally-intensive consensus protocol and blocks to store transactions. Each transaction is a unique block by itself, which must approve two older transactions to be added to the ledger. Tangle uses DAG in a transaction approved by the two older transactions and is added to the ledger through proof of work.

The unique tangle design makes it suitable for IoT networks due to fast validation support, scalability, and fee-less transactions. The main challenge, however, is choosing the two older transactions for validation. No rule is imposed by tangle on how to choose these two transactions, so the validation process can be fine-tuned according to the required application. Therefore, for the purpose of this chapter, the proposed malicious activity detection and isolation scheme are illustrated in Figure A.2 and Figure A.3 in the form of transaction generation flowchart and transaction validation flowchart respectively.

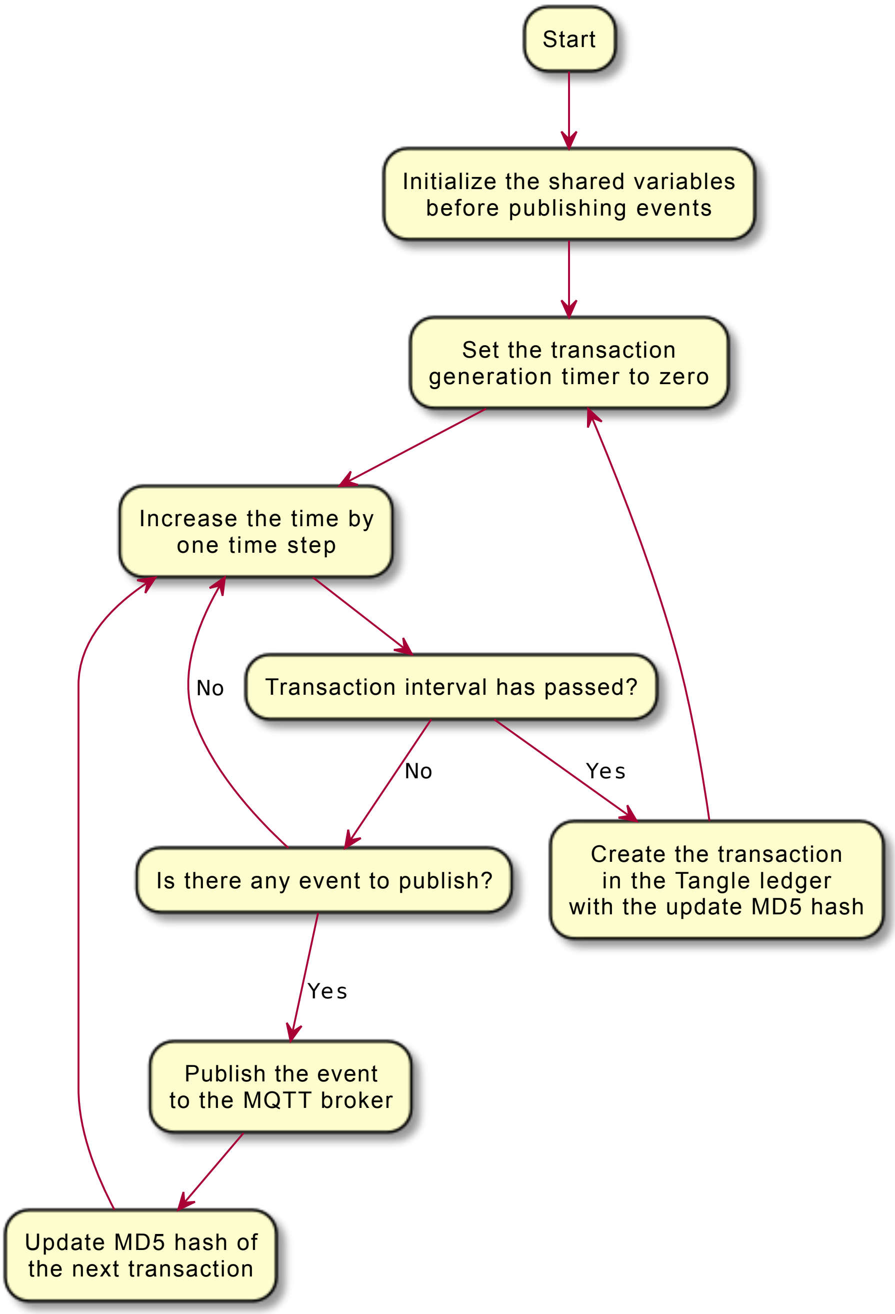

Figure A.2: Transaction generation flowchart in the distributed controllers.

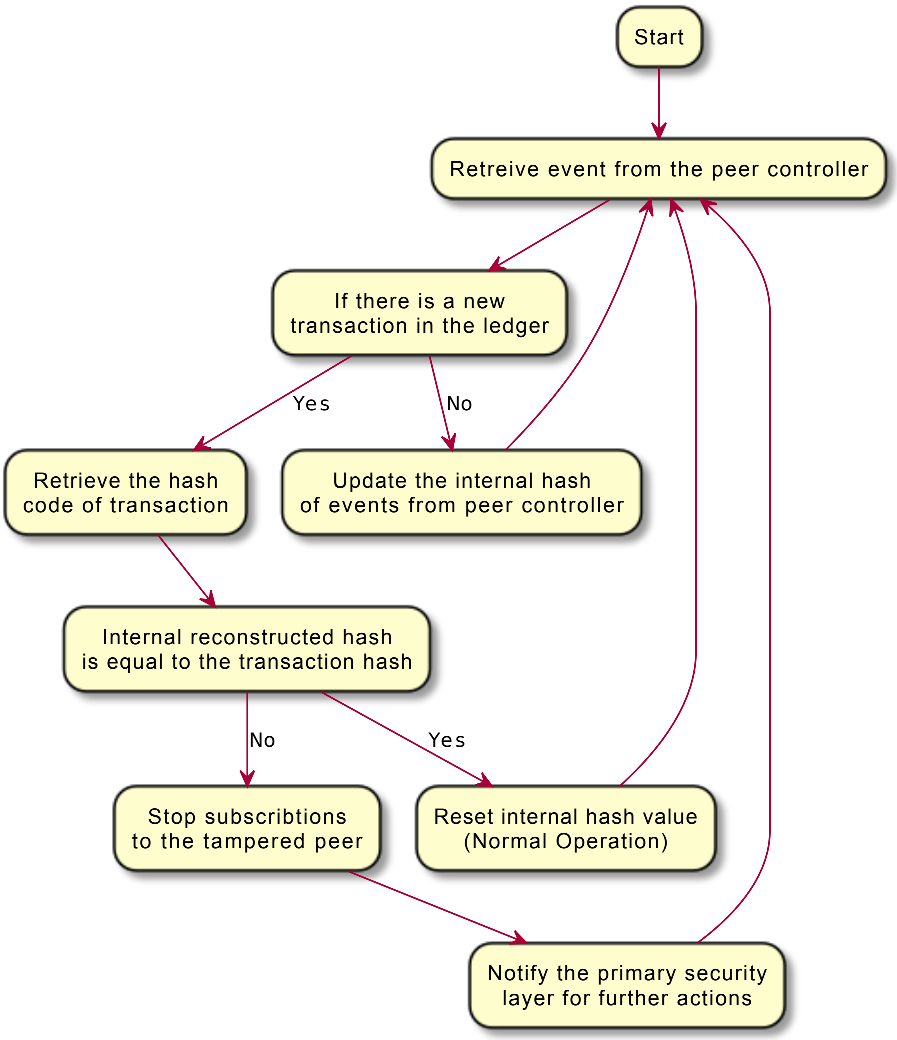

Figure A.3: Transaction validation and protection flowchart for the security regulators of the distributed controllers.

Bibliography

[1] I. Roesch and T. Günther, "Visualization of Neural Network Predictions for Weather Forecasting," *Computer Graphics Forum*, vol. 38, pp. 209–220, Feb. 2019.

[2] T. Dragičević, X. Lu, J. C. Vasquez, and J. M. Guerrero, "DC Microgrids - Part II: A Review of Power Architectures, Applications, and Standardization Issues," *IEEE Transactions on Power Electronics*, vol. 31, pp. 3528–3549, may 2016.

[3] L. E. Zubieta, "Are Microgrids the Future of Energy?: DC Microgrids from Concept to Demonstration to Deployment," *IEEE Electrification Magazine*, vol. 4, pp. 37–44, June 2016.

[4] S. A. Alavi, K. Mehran, Y. Hao, A. Rahimian, H. Mirsaeedi, and V. Vahidinasab, "A distributed event-triggered control strategy for dc microgrids based on publish-subscribe model over industrial wireless sensor networks," *IEEE Transactions on Smart Grid*, vol. 10, no. 4, pp. 4323–4337, 2019.

[5] S. A. Alavi, K. Mehran, and Y. Hao, "Optimal observer synthesis for microgrids with adaptive send-on-delta sampling over iot communication networks," *IEEE Transactions on Industrial Electronics*, vol. 68, no. 11, pp. 11318–11327, 2021.

[6] S. A. Alavi, K. Mehran, V. Vahidinasab, and J. P. S. Catalão, "Forecast based consensus control for dc microgrids using distributed long short-term memory deep learning models," *IEEE Transactions on Smart Grid*, pp. 1–1, 2021.

[7] V. C. Güngör, D. Sahin, T. Kocak, S. Ergüt, C. Buccella, C. Cecati, and G. P. Hancke, "Smart grid technologies: Communication technologies and standards," *IEEE Transactions on Industrial Informatics*, vol. 7, pp. 529–539, nov 2011.

[8] S. Moayedi and A. Davoudi, "Distributed Tertiary Control of DC Microgrid Clusters," *IEEE Transactions on Power Electronics*, vol. 31, pp. 1717–1733, feb 2016.

[9] P. A. Madduri, J. Poon, J. Rosa, M. Podolsky, E. A. Brewer, and S. R. Sanders, "Scalable DC Microgrids for Rural Electrification in Emerging Regions," *IEEE Journal of Emerging and Selected Topics in Power Electronics*, vol. 4, pp. 1195–1205, dec 2016.

[10] T. Samad and A. M. Annaswamy, "Controls for Smart Grids: Architectures and Applications," *Proceedings of the IEEE*, vol. 105, pp. 2244–2261, nov 2017.

[11] C. Li, S. K. Chaudhary, M. Savaghebi, J. C. Vasquez, and J. M. Guerrero, "Power flow analysis for low-voltage ac and dc microgrids considering droop control and virtual impedance," *IEEE Transactions on Smart Grid*, vol. 8, pp. 2754–2764, nov 2017.

[12] J. J. Justo, F. Mwasilu, J. Lee, and J. W. Jung, "AC-microgrids versus DC-microgrids with distributed energy resources: A review," *Renewable and Sustainable Energy Reviews*, vol. 24, pp. 387–405, aug 2013.

[13] E. Planas, J. Andreu, J. I. Gárate, I. Martínez De Alegría, and E. Ibarra, "AC and DC technology in microgrids: A review," *Renewable and Sustainable Energy Reviews*, vol. 43, pp. 726–749, mar 2015.

[14] S. Parhizi, H. Lotfi, A. Khodaei, and S. Bahramirad, "State of the art in research on microgrids: A review," *IEEE Access*, vol. 3, pp. 890–925, 2015.

[15] Z. Akhtar, S. Amir Alavi, and K. Mehran, "Voltage Control in LV Networks Using Electric Springs with Coordination," in *Canadian Conference on Electrical and Computer Engineering*, vol. 2018-May, pp. 1–5, Institute of Electrical and Electronics Engineers Inc., aug 2018.

[16] D. E. Olivares, C. A. Canizares, and M. Kazerani, "A centralized energy management system for isolated microgrids," *IEEE Transactions on Smart Grid*, vol. 5, pp. 1864–1875, jul 2014.

[17] D. I. Brandao, T. Caldognetto, F. P. Marafão, M. G. Simões, J. A. Pomilio, and P. Tenti, "Centralized Control of Distributed Single-Phase Inverters Arbitrarily Connected to Three-Phase Four-Wire Microgrids," *IEEE Transactions on Smart Grid*, vol. 8, pp. 437–446, jan 2017.

[18] L. I. Minchala-Avila, L. Garza-Castanon, Y. Zhang, and H. J. Ferrer, "Optimal Energy Management for Stable Operation of an Islanded Microgrid," *IEEE Transactions on Industrial Informatics*, vol. 12, pp. 1361–1370, aug 2016.

[19] Z. Fan, P. Kulkarni, S. Gormus, C. Efthymiou, G. Kalogridis, M. Sooriyabandara, Z. Zhu, S. Lambotharan, and W. H. Chin, "Smart grid communications: Overview of research challenges, solutions, and standardization activities," *IEEE Communications Surveys and Tutorials*, vol. 15, no. 1, pp. 21–38, 2013.

[20] A. Khorsandi, M. Ashourloo, H. Mokhtari, and R. Iravani, "Automatic droop control for a low voltage DC microgrid," *IET Generation, Transmission and Distribution*, vol. 10, pp. 41–47, jan 2016.

[21] A. Abessi, V. Vahidinasab, and M. S. Ghazizadeh, "Centralized support distributed voltage control by using end-users as reactive power support," *IEEE Transactions on Smart Grid*, vol. 7, pp. 178–188, jan 2016.

[22] T. L. Vandoorn, B. Meersman, J. D. De Kooning, and L. Vandevelde, "Analogy between conventional grid control and islanded microgrid control based on a global DC-link voltage droop," *IEEE Transactions on Power Delivery*, vol. 27, pp. 1405–1414, jul 2012.

[23] T. Morstyn, B. Hredzak, G. D. Demetriades, and V. G. Agelidis, "Unified distributed control for DC microgrid operating modes," *IEEE Transactions on Power Systems*, vol. 31, pp. 802–812, Jan. 2016.

[24] T. Wang, D. O'Neill, and H. Kamath, "Dynamic Control and Optimization of Distributed Energy Resources in a Microgrid," *IEEE Transactions on Smart Grid*, vol. 6, pp. 2884–2894, nov 2015.

[25] A. K. Singh, R. Singh, and B. C. Pal, "Stability analysis of networked control in smart grids," *IEEE Transactions on Smart Grid*, vol. 6, pp. 381–390, jan 2015.

[26] K. Wen and Z. Geng, "Modelling and analysis of distributed networked control systems," *IET Control Theory and Applications*, vol. 6, no. 9, pp. 1304–1312, 2012.

[27] M. Montazeri, A. Alavi, H. Rahmat Jou, J. Mehr Ardestani, and H. Jadali Pour, "Real time substation distributed control system simulator development based on IEC 61850 standard for a sample substation: Case study: Sheikh bahayi substation 400/230/63KV," in *Smart Grid Conference 2013, SGC 2013*, pp. 108–112, IEEE, dec 2013.

[28] Y. L. Wang, C. C. Lim, and P. Shi, "Adaptively Adjusted Event-Triggering Mechanism on Fault Detection for Networked Control Systems," *IEEE Transactions on Cybernetics*, vol. 47, pp. 2299–2311, aug 2017.

[29] L. Herrera, R. Murawski, F. Guo, E. Inoa, E. Ekici, and J. Wang, "PHEVs charging stations, communications, and control simulation in real time," in *2011 IEEE Vehicle Power and Propulsion Conference, VPPC 2011*, pp. 1–5, IEEE, sep 2011.

[30] P. H. Ellis, "Extension of phase plane analysis to quantized systems," *IRE Transactions on Automatic Control*, vol. 4, pp. 43–54, Nov. 1958.

[31] W. P. Heemels, R. J. Gorter, A. Van Zijl, P. P. Van Den Bosch, S. Weiland, W. H. Hendrix, and M. R. Vonder, "Asynchronous measurement and control: A case study on motor synchronization," *Control Engineering Practice*, vol. 7, pp. 1467–1482, Dec. 1999.

[32] P. Tabuada, "Event-triggered real-time scheduling of stabilizing control tasks," *IEEE Transactions on Automatic Control*, vol. 52, pp. 1680–1685, sep 2007.

[33] M. Guinaldo, D. V. Dimarogonas, K. H. Johansson, J. Sánchez, and S. Dormido, "Distributed event-based control for interconnected linear systems," *Proceedings of the IEEE Conference on Decision and Control*, vol. 7, pp. 2553–2558, apr 2011.

[34] B. A. Khashooei, D. J. Antunes, and W. P. Heemels, "Output-Based Event-Triggered Control with Performance Guarantees," *IEEE Transactions on Automatic Control*, vol. 62, pp. 3646–3652, jul 2017.

[35] M. Abdelrahim, R. Postoyan, J. Daafouz, and D. Nešić, "Stabilization of Nonlinear Systems Using Event-Triggered Output Feedback Controllers," *IEEE Transactions on Automatic Control*, vol. 61, pp. 2682–2687, sep 2016.

[36] R. Postoyan, P. Tabuada, D. Nešić, and A. Anta, "A Framework for the Event-Triggered Stabilization of Nonlinear Systems," *IEEE Transactions on Automatic Control*, vol. 60, pp. 982–996, apr 2015.

[37] C. Peng and Q. L. Han, "A novel event-triggered transmission scheme and l2 control co-design for sampled-data control systems," *IEEE Transactions on Automatic Control*, vol. 58, pp. 2620–2626, oct 2013.

[38] A. Anta and P. Tabuada, "To sample or not to sample: Self-triggered control for nonlinear systems," *IEEE Transactions on Automatic Control*, vol. 55, pp. 2030–2042, sep 2010.

[39] W. Li, Y. Jia, and J. Du, "Event-triggered Kalman consensus filter over sensor networks," *IET Control Theory and Applications*, vol. 10, pp. 103–110, jan 2016.

[40] C. Rodríguez-Domínguez, K. Benghazi, M. Noguera, J. L. Garrido, M. L. Rodríguez, and T. Ruiz-López, "A Communication model to integrate the Request-Response and the publish-subscribe paradigms into ubiquitous systems," *Sensors (Switzerland)*, vol. 12, pp. 7648–7668, jun 2012.

[41] Y. Sakurai, K. Takada, M. Anisetti, V. Bellandi, P. Ceravolo, E. Damiani, and S. Tsuruta, "Toward sensor-based context aware systems," *Sensors*, vol. 12, pp. 632–649, jan 2012.

[42] J. Zhu, M. Liu, J. Cao, G. Chen, H. Gong, and F. Xu, "CED: A community-based event delivery protocol in publish/subscribe systems for Delay Tolerant Sensor Network (DTSN)," in *Proceedings of the International Conference on Parallel Processing*, vol. 9, pp. 58–65, Molecular Diversity Preservation International, sep 2009.

[43] C. Flores, P. Grace, and G. S. Blair, "SeDiM: A middleware framework for interoperable service discovery in heterogeneous networks," *ACM Transactions on Autonomous and Adaptive Systems*, vol. 6, no. 1, pp. 6:1—-6:8, 2011.

[44] L. Roffia, F. Morandi, J. Kiljander, A. D'Elia, F. Vergari, F. Viola, L. Bononi, and T. Salmon Cinotti, "A Semantic Publish-Subscribe Architecture for the Internet of Things," *IEEE Internet of Things Journal*, vol. 3, pp. 1274–1296, dec 2016.

[45] G. Xylomenos, X. Vasilakos, C. Tsilopoulos, V. A. Siris, and G. C. Polyzos, "Caching and mobility support in a publish-subscribe internet architecture," *IEEE Communications Magazine*, vol. 50, pp. 52–58, jul 2012.

[46] S. Amir Alavi, A. Rahimian, K. Mehran, and J. Alaleddin Mehr Ardestani, "An IoT-Based Data Collection Platform for Situational Awareness-Centric Microgrids," in *Canadian Conference on Electrical and Computer Engineering*, vol. 2018-May, pp. 1–4, IEEE, 2018.

[47] T. Monajemi, A. Rahimian, and K. Mehran, "Energy management using a situational awareness-centric ad-hoc network in a home environ-

ment," in *Lecture Notes of the Institute for Computer Sciences, Social-Informatics and Telecommunications Engineering, LNICST*, vol. 203, pp. 15–24, Springer, Cham, mar 2017.

[48] J. Zhou, H. Zhang, Q. Sun, D. Ma, and B. Huang, "Event-based distributed active power sharing control for interconnected AC and DC microgrids," 2018.

[49] E. Harmon, U. Ozgur, M. H. Cintuglu, R. De Azevedo, K. Akkaya, and O. A. Mohammed, "The Internet of Microgrids: A Cloud-Based Framework for Wide Area Networked Microgrids," *IEEE Transactions on Industrial Informatics*, vol. 14, pp. 1262–1274, Mar. 2018.

[50] M. F. Zia, M. Benbouzid, E. Elbouchikhi, S. M. Muyeen, K. Techato, and J. M. Guerrero, "Microgrid transactive energy: Review, architectures, distributed ledger technologies, and market analysis," 2020.

[51] H. S. Nunna and D. Srinivasan, "Multiagent-Based Transactive Energy Framework for Distribution Systems with Smart Microgrids," *IEEE Transactions on Industrial Informatics*, vol. 13, pp. 2241–2250, Oct. 2017.

[52] Z. Zhao, J. Guo, X. Luo, J. Xue, C. S. Lai, Z. Xu, and L. L. Lai, "Energy Transaction for Multi-Microgrids and Internal Microgrid Based on Blockchain," *IEEE Access*, vol. 8, pp. 144362–144372, 2020.

[53] L. Liang, Y. Hou, and D. J. Hill, "An interconnected microgrids-based transactive energy system with multiple electric springs," *IEEE Transactions on Smart Grid*, vol. 11, pp. 184–193, Jan. 2020.

[54] M. N. Faqiry and S. Das, "Double Auction with Hidden User Information: Application to Energy Transaction in Microgrid," *IEEE Transactions on Systems, Man, and Cybernetics: Systems*, vol. 49, pp. 2326–2339, Nov. 2019.

[55] M. Daneshvar, B. Mohammadi-Ivatloo, K. Zare, and S. Asadi, "Two-Stage Robust Stochastic Model Scheduling for Transactive Energy Based Renewable Microgrids," *IEEE Transactions on Industrial Informatics*, vol. 16, pp. 6857–6867, Nov. 2020.

[56] M. Daneshvar, B. Mohammadi-Ivatloo, M. Abapour, S. Asadi, and R. Khanjani, "Distributionally Robust Chance-Constrained Transactive Energy Framework for Coupled Electrical and Gas Microgrids," *IEEE Transactions on Industrial Electronics*, vol. 68, pp. 347–357, Jan. 2021.

[57] S. A. Alavi, M. Javadipour, and K. Mehran, "Microgrid Optimal State Estimation Over IoT Wireless Sensor Networks With Event-Based Measurements," in *IECON 2019 - 45th Annual Conference of the IEEE Industrial Electronics Society*, pp. 4145–4150, IEEE, Oct. 2019.

[58] M. M. Gulzar, S. T. H. Rizvi, M. Y. Javed, U. Munir, and H. Asif, "Multi-agent cooperative control consensus: A comparative review," *Electronics (Switzerland)*, vol. 7, no. 2, 2018.

[59] C. Wang, J. Duan, B. Fan, Q. Yang, and W. Liu, "Decentralized High-Performance Control of DC Microgrids," *IEEE Transactions on Smart Grid*, vol. 10, pp. 3355–3363, May 2019.

[60] Q. Xu, X. Hu, P. Wang, J. Xiao, P. Tu, C. Wen, and M. Y. Lee, "A Decentralized Dynamic Power Sharing Strategy for Hybrid Energy Storage System in Autonomous DC Microgrid," *IEEE Transactions on Industrial Electronics*, vol. 64, pp. 5930–5941, July 2017.

[61] J. Peng, B. Fan, J. Duan, Q. Yang, and W. Liu, "Adaptive decentralized output-constrained control of single-bus DC microgrids," *IEEE/CAA Journal of Automatica Sinica*, vol. 6, pp. 424–432, Mar. 2019.

[62] Y. Hu, X. Wang, Y. Peng, J. Xiang, and W. Wei, "Distributed Finite-Time Secondary Control for DC Microgrids with Virtual Impedance Arrangement," *IEEE Access*, vol. 7, pp. 57060–57068, 2019.

[63] J. Xiao, P. Wang, L. Setyawan, and Q. Xu, "Multi-level energy management system for real-time scheduling of DC microgrids with multiple slack terminals," *IEEE Transactions on Energy Conversion*, vol. 31, pp. 392–400, Mar. 2016.

[64] X. Lei, T. Huang, Y. Yang, Y. Fang, and P. Wang, "A bi-layer multi-time coordination method for optimal generation and reserve schedule and dispatch of a grid-connected microgrid," *IEEE Access*, vol. 7, pp. 44010–44020, 2019.

[65] R. Zhang, B. Hredzak, and T. Morstyn, "Distributed Control with Virtual Capacitance for the Voltage Restorations, State of Charge Balancing and Load Allocations of Heterogeneous Energy Storages in a DC Datacenter Microgrid," *IEEE Transactions on Energy Conversion*, 2018.

[66] R. Han, J. M. Guerrero, M. Tucci, A. Martinelli, and G. Ferrari-Trecate, "Plug-and-Play Voltage/Current Stabilization DC Microgrid Clusters with Grid-Forming/Feeding Converters," in *Proceedings of the American Control Conference*, vol. 2018-June, pp. 5362–5367, IEEE, jun 2018.

[67] D. Kumar, F. Zare, and A. Ghosh, "DC Microgrid Technology: System Architectures, AC Grid Interfaces, Grounding Schemes, Power Quality, Communication Networks, Applications, and Standardizations Aspects," *IEEE Access*, vol. 5, pp. 12230–12256, 2017.

[68] D. J. Becker and B. J. Sonnenberg, "DC microgrids in buildings and data centers," in *INTELEC, International Telecommunications Energy Conference (Proceedings)*, pp. 1–7, IEEE, oct 2011.

[69] H. Shi, M. Xu, and R. Li, "Deep Learning for Household Load Forecasting-A Novel Pooling Deep RNN," *IEEE Transactions on Smart Grid*, vol. 9, pp. 5271–5280, Sept. 2018.

[70] S. Hochreiter and J. Schmidhuber, "Long Short-Term Memory," *Neural Computation*, vol. 9, pp. 1735–1780, Nov. 1997.

[71] C. Yan, Y. Zhang, J. Xu, F. Dai, J. Zhang, Q. Dai, and F. Wu, "Efficient parallel framework for HEVC motion estimation on many-core processors," *IEEE Transactions on Circuits and Systems for Video Technology*, vol. 24, no. 12, pp. 2077–2089, 2014.

[72] W. Kong, Z. Y. Dong, Y. Jia, D. J. Hill, Y. Xu, and Y. Zhang, "Short-Term Residential Load Forecasting Based on LSTM Recurrent Neural Network," *IEEE Transactions on Smart Grid*, vol. 10, pp. 841–851, Jan. 2019.

[73] X. Cao, S. Dong, Z. Wu, and Y. Jing, "A data-driven hybrid optimization model for shortterm residential load forecasting," in *2015 IEEE International Conference on Computer and Information Technology*, (Liverpool, U.K), pp. 283–287, CIT/IUCC/DASC/PICOM, 2015.

[74] Z. Yun, Z. Quan, S. Caixin, L. Shaolan, L. Yuming, and S. Yang, "RBF neural network and ANFIS-based short-term load forecasting approach in real-time price environment," *IEEE Transactions on Power Systems*, vol. 23, no. 3, pp. 853–858, 2008.

[75] R. Zhang, Y. Xu, Z. Y. Dong, W. Kong, and K. P. Wong, "A composite k-nearest neighbor model for day-ahead load forecasting with limited temperature forecasts," in *IEEE Power and Energy Society General Meeting*, vol. 2016-Novem, (Boston, MA, USA), pp. 1–5, 2016.

[76] Q. Pang and M. Zhang, "Very short-term load forecasting based on neural network and rough set," in *2010 International Conference on Intelligent Computation Technology and Automation, ICICTA 2010*, vol. 3, (Changsha, China), pp. 1132–1135, 2010.

[77] R. Zhang, Z. Y. Dong, Y. Xu, K. Meng, and K. P. Wong, "Short-term load forecasting of Australian national electricity market by an ensemble model of extreme learning machine," *IET Generation, Transmission and Distribution*, vol. 7, no. 4, pp. 391–397, 2013.

[78] M. Ghofrani, M. Ghayekhloo, A. Arabali, and A. Ghayekhloo, "A hybrid short-term load forecasting with a new input selection framework," *Energy*, vol. 81, pp. 777–786, 2015.

[79] J. C. Mayo-Maldonado, R. Salas-Cabrera, J. C. Rosas-Caro, J. De Leon-Morales, and E. N. Salas-Cabrera, "Modelling and control of a DC-DC multilevel boost converter," *IET Power Electronics*, vol. 4, no. 6, pp. 693–700, 2011.

[80] D. Spanos, R. Olfati-Saber, and R. Murray, "Dynamic consensus on mobile networks," in *The 16th IFAC World Congress, . . .* , pp. 1–6, 2005.

[81] V. Nasirian, S. Moayedi, A. Davoudi, and F. L. Lewis, "Distributed cooperative control of dc microgrids," *IEEE Transactions on Power Electronics*, vol. 30, pp. 2288–2303, Apr. 2015.

[82] D. Chen, L. Xu, and L. Yao, "DC network stability and dynamic analysis using virtual impedance method," in *IECON Proceedings (Industrial Electronics Conference)*, pp. 5625–5630, IEEE, oct 2012.

[83] T. Tanaka, K. Hirose, D. Marquet, B. J. Sonnenberg, and M. Szpek, "Analysis of wiring design for 380-VDC power distribution system at telecommunication sites," *INTELEC, International Telecommunications Energy Conference (Proceedings)*, 2012.

[84] M. G. Villalva, J. R. Gazoli, and E. R. Filho, "Comprehensive approach to modeling and simulation of photovoltaic arrays," *IEEE Transactions on Power Electronics*, vol. 24, pp. 1198–1208, may 2009.

[85] S. A. Alavi, A. Rahimian, K. Mehran, and V. Vahidinasab, "Multilayer event-based distributed control system for dc microgrids with non-uniform delays and directional communication," *IET Generation, Transmission & Distribution*, vol. n/a, no. n/a.

[86] R. Han, L. Meng, J. M. Guerrero, and J. C. Vasquez, "Distributed Nonlinear Control with Event-Triggered Communication to Achieve Current-Sharing and Voltage Regulation in DC Microgrids," *IEEE Transactions on Power Electronics*, vol. 33, pp. 6416–6433, jul 2018.

[87] M. Mesbahi and M. Egerstedt, *Graph theoretic methods in multiagent networks*. Princeton University Press, 2010.

[88] U. Münz, A. Papachristodoulou, and F. Allgöwer, "Delay robustness in consensus problems," *Automatica*, vol. 46, no. 8, pp. 1252–1265, 2010.

[89] R. Olfati-Saber and R. M. Murray, "Consensus problems in networks of agents with switching topology and time-delays," *IEEE Transactions on Automatic Control*, vol. 49, no. 9, pp. 1520–1533, 2004.

[90] P. Pepe and Z. P. Jiang, "A Lyapunov-Krasovskii methodology for ISS and iISS of time-delay systems," *Systems and Control Letters*, vol. 55, no. 12, pp. 1006–1014, 2006.

[91] G. S. Seyboth, D. V. Dimarogonas, and K. H. Johansson, "Event-based broadcasting for multi-agent average consensus," *Automatica*, vol. 49, pp. 245–252, jan 2013.

[92] F. Yizheng, "On spectral integral variations of graphs," *Linear and Multilinear Algebra*, vol. 50, no. 2, pp. 133–142, 2002.

[93] A. Sydney, C. Scoglio, and D. Gruenbacher, "Optimizing algebraic connectivity by edge rewiring," *Applied Mathematics and Computation*, vol. 219, pp. 5465–5479, jan 2013.

[94] T. T. Tay, I. M. Y. Mareels, and J. B. Moore, *High Performance Control*. Systems & Control: Foundations & Applications, Boston, MA: Birkhäuser Boston, 1997.

[95] P. N. Paraskevopoulos, *Modern control engineering*. Prentice-Hall, 2017.

[96] R. Zhang and B. Hredzak, "Distributed finite-time multiagent control for DC microgrids with time delays," *IEEE Transactions on Smart Grid*, vol. 10, pp. 2692–2701, may 2019.

[97] M. Baranwal, A. Askarian, S. Salapaka, and M. Salapaka, "A Distributed Architecture for Robust and Optimal Control of DC Microgrids," *IEEE Transactions on Industrial Electronics*, vol. 66, pp. 3082–3092, apr 2019.

[98] P. Mathew, S. Madichetty, and S. Mishra, "A Multilevel Distributed Hybrid Control Scheme for Islanded DC Microgrids," *IEEE Systems Journal*, vol. 13, pp. 4200–4207, dec 2019.

[99] S. Trip, M. Cucuzzella, X. Cheng, and J. Scherpen, "Distributed averaging control for voltage regulation and current sharing in DC microgrids," *IEEE Control Systems Letters*, vol. 3, pp. 174–179, jan 2019.

[100] M. S. Rahman, M. J. Hossain, J. Lu, and H. R. Pota, "A Need-Based Distributed Coordination Strategy for EV Storages in a Commercial Hybrid AC/DC Microgrid With an Improved Interlinking Converter Control Topology," *IEEE Transactions on Energy Conversion*, vol. 33, pp. 1372–1383, sep 2018.

[101] A. Zakhor and A. V. Oppenheim, "Reconstruction of Two-Dimensional Signals from Level Crossings," *Proceedings of the IEEE*, vol. 78, no. 1, pp. 31–55, 1990.

[102] Y. H. Fung and Y. H. Chan, "A POCS-based restoration algorithm for restoring halftoned color-quantized images," *IEEE Transactions on Image Processing*, vol. 15, pp. 1985–1992, July 2006.

[103] S.-j. Yeh and H. Stark, "Iterative and one-step reconstruction from nonuniform samples by convex projections," *Journal of the Optical Society of America A*, vol. 7, p. 491, Mar. 1990.

[104] D. Rzepka, M. Miskowicz, D. Koscielnik, and N. T. Thao, "Reconstruction of signals from level-crossing samples using implicit information," *IEEE Access*, vol. 6, pp. 35001–35011, 2018.

[105] B. Huang, L. Liu, H. Zhang, Y. Li, and Q. Sun, "Distributed Optimal Economic Dispatch for Microgrids Considering Communication Delays," *IEEE Transactions on Systems, Man, and Cybernetics: Systems*, vol. 49, pp. 1634–1642, aug 2019.

[106] J. Su, B. Li, and W. H. Chen, "On existence, optimality and asymptotic stability of the Kalman filter with partially observed inputs," *Automatica*, vol. 53, pp. 149–154, Mar. 2015.

[107] F. Deutsch and H. Hundal, "The rate of convergence for the cyclic projections algorithm III: Regularity of convex sets," *Journal of Approximation Theory*, vol. 155, pp. 155–184, Dec. 2008.

[108] M. Iglesias-Urkia, D. Casado-Mansilla, S. Mayer, J. Bilbao, and A. Urbieta, "Integrating Electrical Substations Within the IoT Using IEC 61850, CoAP, and CBOR," *IEEE Internet of Things Journal*, vol. 6, pp. 7437–7449, Oct. 2019.

[109] P. Ji, D. Xiong, P. Wang, and J. Chen, "A study on exponential smoothing model for load forecasting," in *Asia-Pacific Power and Energy Engineering Conference, APPEEC*, 2012.

[110] M. David, F. Ramahatana, P. Trombe, and P. Lauret, "Probabilistic forecasting of the solar irradiance with recursive ARMA and GARCH models," *Solar Energy*, vol. 133, pp. 55–72, Aug. 2016.

[111] F. Wang, K. Li, L. Zhou, H. Ren, J. Contreras, M. Shafie-khah, and J. P. Catalão, "Daily pattern prediction based classification modeling approach for day-ahead electricity price forecasting," *International Journal of Electrical Power & Energy Systems*, vol. 105, pp. 529–540, Feb. 2019.

[112] R. Haiges, Y. Wang, A. Ghoshray, and A. Roskilly, "Forecasting Electricity Generation Capacity in Malaysia: An Auto Regressive Integrated Moving Average Approach," *Energy Procedia*, vol. 105, pp. 3471–3478, May 2017.

[113] D. Tien Bui, K.-T. T. Bui, Q.-T. Bui, C. V. Doan, and N.-D. Hoang, "Hybrid Intelligent Model Based on Least Squares Support Vector Regression and Artificial Bee Colony Optimization for Time-Series Modeling and Forecasting Horizontal Displacement of Hydropower Dam," in *Handbook of Neural Computation*, pp. 279–293, Elsevier, 2017.

[114] H. Yang, J. Long, P. He, and Y. Zheng, "Short-Term Load Forecasting of Microgrid Based on Grey Correlation Analysis and Neural Network Optimized by Mind Evolutionary Algorithm," in *2019 IEEE PES Innovative Smart Grid Technologies Asia, ISGT 2019*, pp. 2738–2742, Institute of Electrical and Electronics Engineers Inc., May 2019.

[115] U. K. Das, K. S. Tey, M. Seyedmahmoudian, S. Mekhilef, M. Y. I. Idris, W. Van Deventer, B. Horan, and A. Stojcevski, "Forecasting of photovoltaic power generation and model optimization: A review," *Renewable and Sustainable Energy Reviews*, vol. 81, pp. 912–928, Jan. 2018.

[116] R. Ahmed, V. Sreeram, Y. Mishra, and M. Arif, "A review and evaluation of the state-of-the-art in PV solar power forecasting: Techniques and optimization," *Renewable and Sustainable Energy Reviews*, vol. 124, p. 109792, May 2020.

[117] Y. Ren, P. Suganthan, and N. Srikanth, "Ensemble methods for wind and solar power forecasting—A state-of-the-art review," *Renewable and Sustainable Energy Reviews*, vol. 50, pp. 82–91, Oct. 2015.

[118] M. K. Behera, I. Majumder, and N. Nayak, "Solar photovoltaic power forecasting using optimized modified extreme learning machine technique," *Engineering Science and Technology, an International Journal*, vol. 21, pp. 428–438, June 2018.

[119] S. Sobri, S. Koohi-Kamali, and N. A. Rahim, "Solar photovoltaic generation forecasting methods: A review," *Energy Conversion and Management*, vol. 156, pp. 459–497, Jan. 2018.

[120] A. Garulli, S. Paoletti, and A. Vicino, "Models and Techniques for Electric Load Forecasting in the Presence of Demand Response," *IEEE Transactions on Control Systems Technology*, vol. 23, pp. 1087–1097, May 2015.

[121] T. Ergen and S. S. Kozat, "Online Training of LSTM Networks in Distributed Systems for Variable Length Data Sequences," *IEEE Transactions on Neural Networks and Learning Systems*, vol. 29, pp. 5159–5165, Oct. 2018.

[122] UK Power Networks, "Photovoltaic (PV) Solar Panel Energy Generation data," 2014.

[123] H. N. Dai, K. W. Ng, M. Li, and M. Y. Wu, "An overview of using directional antennas in wireless networks," *International Journal of Communication Systems*, vol. 26, pp. 413–448, apr 2013.

[124] S. Jayaprakasam, S. K. A. Rahim, and C. Y. Leow, "Distributed and Collaborative Beamforming in Wireless Sensor Networks: Classifications, Trends, and Research Directions," *IEEE Communications Surveys and Tutorials*, vol. 19, no. 4, pp. 2092–2116, 2017.

[125] K. Sundaresan and R. Sivakumar, "Ad hoc networks with heterogeneous smart antennas: Performance analysis and protocols," *Wireless Communications and Mobile Computing*, vol. 6, pp. 893–916, nov 2006.

[126] J. H. Winters and M. J. Gans, "The range increase of adaptive versus phased arrays in mobile radio systems," *Conference Record - Asilomar Conference on Signals, Systems and Computers*, vol. 1, pp. 109–115, mar 1994.

[127] M. Onyeka Okoye, J. Yang, J. Cui, Z. Lei, J. Yuan, H. Wang, H. Ji, J. Feng, and C. Ezeh, "A Blockchain-Enhanced Transaction Model for Microgrid Energy Trading," *IEEE Access*, vol. 8, pp. 143777–143786, 2020.